A GAIN-SCHEDULED CONTROL SCHEME FOR IMPROVED MANEUVERABILITY AND POWER EFFICIENCY OF UNDERWATER GLIDERS

by
Ashton Johnston

A thesis submitted to The Johns Hopkins University in conformity
with the requirements for the degree of Master of Science

Baltimore, Maryland
December, 2022

Abstract

Underwater gliders are a relatively new type of low-power, long duration underwater vehicle that use changes in buoyancy to propel themselves forward. They are widely used today for oceanographic research, and a number of theoretical control schemes have been derived over the years. However, despite their nonlinear dynamics that evolve as a function of their environment and operating conditions, most fielded gliders use linear control methods, such as static-gain proportional-integral (PI) or proportional-integral-derivative (PID) compensators for motion control, which can significantly limit vehicle performance.

This thesis develops an alternative approach to underwater glider control that employs control system gain-scheduling to improve vehicle performance and efficiency over a wider range of operating conditions as compared to static or fixed-gain approaches. The primary contribution of this thesis is the development of a practical gain-scheduling procedure using linearized models of the decoupled pitch and yaw dynamics of the vehicle. This methodology improves on the current fixed-gain topologies used on fielded gliders today, while being straightforward and cost-effective to implement.

In this thesis, the development of a nonlinear dynamical model of a Slocum glider using computer-aided design (CAD) and computational fluid dynamics (CFD) simulations was also carried out to support the high-fidelity characterization of the controller topologies. A nonlinear numerical simulation of the Slocum glider was developed

in Matlab and was used to assess the performance improvements and the increased robustness of the gain-scheduled PID method to a standard fixed-gain PID approach.

Primary Reader and Advisor: Dr. Neil F. Palumbo

Secondary Reader: Dr. Adam Watkins

Tertiary Reader: Dr. Cleon Davis

Acknowledgments

This thesis is partly a product of my research work done at The Johns Hopkins University Applied Physics Laboratory (JHUAPL), as well as additional research done toward my degree from the Whiting School of Engineering at Johns Hopkins University. I want to express my sincerest thanks to my advisor, Dr. Neil Palumbo, for his advice and instruction during this process. He was a consistent and patient voice of support and technical guidance, and I consider the opportunity to work with him a great privilege. I also thank him for all of the effort he put into advising my research and for his extensive help in editing this document. Without him, this thesis would never have happened.

I thank my thesis readers, Dr. Adam Watkins and Dr. Cleon Davis of Johns Hopkins University's Electrical and Computer Engineering Department, for their time and advice. Their technical and administrative assistance helped to keep this work focused and on schedule, and this thesis is better because of them. I would also like to thank my coworkers at JHUAPL for their support and flexibility as I undertook this thesis while working alongside them. In particular, I would like to thank my supervisors Nate Macias, Mike Labarre, Justin Morrison and Mike Buschman for their interest in this research and guidance during numerous conversations on the results of this work. I would also like to thank Chuck Kerechanin for his help in getting me started with Solidworks and his assistance with setting up and analyzing the Flow Simulation runs.

Contents

List of Tables

List of Figures

List of Symbols

b   Displacement vector of masses in the world frame

F   External Force vector

f   Hydrodynamic forces in the world frame

$\mathbf{f}_{gi}$ Gravitational forces of point mass in the world frame

I   Identity matrix

J   Moment of Inertia matrix

l   Angular inertia in the world frame

m   Mass matrix

p   Linear inertia in the world frame

q   Quaternion Vector

r   Displacement vector of a mass in the body frame

$\mathbf{R}_{\phi}$ Roll Rotation Matrix

$\mathbf{R}_{\psi}$ Yaw Rotation Matrix

$\mathbf{R}_{\theta}$ Pitch Rotation Matrix

T   External Torque vector

t	Hydrodynamic torques in the world frame
CB	Center of Buoyancy
CG	Center of Gravity
δ_R	Rudder Deflection Angle
ω_n	Natural Frequency
ϕ	Body Roll Angle
ψ	Body Yaw Angle
ρ	Water Density
θ	Body Pitch Angle
ξ	Glide Path Angle
ζ	Damping Coefficient
d_θ	Disturbance in the Pitch Axis
dT	Control Update Time Step
K	Nomoto Gain Constant
$K_{D,D0}$	Drag Coefficients
$K_{L,L0}$	Lift Coefficients
$K_{M,M0}$	Pitching Moment Coefficients
$K_{P,I,D}$	Proportional, Integral, Derivative Gains
p, q, r	Body Roll, Pitch, Yaw Rotational Rates
T	Nomoto Time Constant

u, v, w	Body x,y,z Translational Rates
V	Vehicle velocity vector
$V_{H,N,E}$	Vehicle Speeds Horizontal, North, East Directions
α	Angle of attack (AoA)
$\bar{m}, m_{movable}$	Movable (battery) mass
β	Angle of sideslip (AoS)
ω	Angular velocity in the body frame
υ	Translational velocity in the body frame
$\mathbf{C}_{3x3}$	Cross term matrix in dynamic equation
$\mathbf{D}_{3x3}$	Cross term matrix in dynamic equation
$\mathbf{F}_{ext}$	Hydrodynamic forces in the wind frame
$\mathbf{g}$	Gravity vector
$\mathbf{J}_s$	Moment of inertia of stationary mass
$\mathbf{J}_{3x3}$	Overall moment of inertia matrix
$\mathbf{J}_{added}$	Hydrodynamic added inertia matrix
$\mathbf{k}$	Gravity unit vector in "z" direction
$\mathbf{L}$	Angular inertia in the body frame
$\mathbf{M}_{3x3}$	Overall mass inertia matrix
$\mathbf{M}_{added}$	Hydrodynamic added mass matrix
$\mathbf{P}$	Linear inertia in the body frame

$\mathbf{R}_{BE}$	Rotation matrix from body to world frame
$\mathbf{R}_{EB}$	Rotation matrix from world to body frame
$\mathbf{R}_{WB}$	Rotation matrix from wind to body frame
$\mathbf{T}_{ext}$	Hydrodynamic torques in the wind frame
$\mathbb{I}$	Inertia matrix (6x6)
D	Drag force
L	Lift force
m_0	Net buoyancy
$m_b, m_{ballast}$	Variable Ballast mass
m_s	Stationary (distributed hull) mass
M_{DL_i}	Hydrodynamic moments
$r_b, \mathbf{r}_{ballast}$	Displacement vector of ballast mass in the body frame
$r_p, \mathbf{r}_{movable}$	Displacement vector of movable mass in the body frame
SF	Side force

Chapter 1

Introduction

Underwater gliders are a relatively new and innovative class of autonomous underwater vehicle (AUV) that moves through the water column by controlling its attitude and buoyancy using internal actuators. Gliders have a number of useful applications, most notably in oceanographic sensing and data collection, as well as a variety of defense applications. They are attractive sensing platforms due to their relatively low size, weight and cost, autonomy, and long-range, long-duration capabilities. For these reasons, the last 20 years have seen a wide adoption of gliders for oceanographic research purposes, and with that, extensive research into various control strategies for these systems. However, a gap remains between theoretical and realizable control methods that are simultaneously easy to implement and provide robust control in the dynamic ocean environment due to power and processing constraints, as well as sensor size and weight limitations. This thesis attempts to bridge that gap through development of a nonlinear dynamical model of an underwater glider and a gain-scheduled control scheme that is simple to derive and characterize.

There are two key areas of this work:

1. *The modeling of the nonlinear dynamics of an underwater glider through first-principles and CFD methods.* As part of this work, a CAD model of a Slocum glider

was created, and CFD was used to determine the forces and moments acting on the vehicle at different operating points (e.g. angle-of-attack, angle-of-sideslip). These nonlinear force and moment coefficients were applied to the six-degree-of-freedom (6DoF) dynamic equations of vehicle motion in order to more precisely represent the actual vehicle response characteristics (e.g., roll-pitch-yaw coupling). The development of a ground truth dynamical model is necessary for systematic model-based control design for this class of vehicle and allows for the comparison of linear and nonlinear control methods in a simulated environment. This modeling methodology can also be tailored to other gliders for the purpose of predicting performance, developing improved control and navigation algorithms, and design analysis.

2. *The development and analysis of a gain-scheduled controller through the use of decoupled, linearized dynamic equations of motion.* By linearizing the dynamics of an underwater glider at various operating points, it is possible to apply linear control theory methods to design stable and highly performant controllers that better account for the nonlinear variations in the vehicle dynamics as the operating point changes. A straightforward methodology is developed for designing such a system, and the differences in vehicle performance are discussed.

In this introduction, we describe the attributes of underwater gliders (Section 1.1), their applications in oceanographic research (Section 1.2), the motivation behind studying more performant control schemes (Section 1.3), and provide a literature review of previous work on the use and control of underwater gliders (Section 1.4).

1.1 Glider Characteristics and Design

Underwater gliders are widely used to gather oceanographic data due to their power efficiency and long-range capabilities. These gliders are trimmed to be neutrally buoyant in water so that by ingesting water (decreasing their displacement) they become heavier than the surrounding fluid and sink, and by expelling water (increasing their displacement) they become lighter than the surrounding fluid and rise. The glider's fixed wings convert the vertical motion of the vehicle to the horizontal plane by producing a forward force that propels the vehicle without need for a conventional thruster. This creates a sawtooth flight profile in the vertical plane that is unique to underwater gliders (Figure 1-1). Gliders may also make themselves neutrally buoyant and drift with the current, rest on the ocean bottom, or float on the surface like a spar buoy.
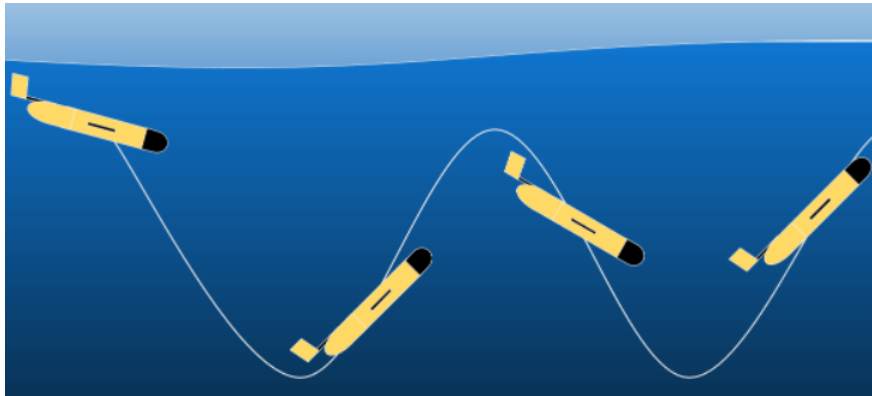
Figure 1-1. Typical underwater glider flight profile in the vertical plane.

The need for gliders to perform both descending and ascending glides places constraints on the wing design of the vehicles. The change in glide direction results in the lift force generated by the wings to change directions from upward on descending glides to downward on ascending glides. Because it is necessary to change the direction of the lift force, the glider's wings must be symmetrically cambered in order to produce relatively equal amounts of lift in both glide directions. Most gliders use simple flat-plate wings

that are placed near the center of the body. The changing lift direction also results in an interesting effect where an ascending glider must bank to port in order to turn starboard, while a descending glider must bank to starboard in order to turn starboard.

The use of buoyancy propulsion systems and low-power designs make gliders capable of long ranges and high-endurance deployments. Their high transport efficiency results from the use of wings rather than a propeller, as well as their low speeds with respect to the surrounding water, both of which minimize the power needed to overcome the drag of the vehicle [40]. Most commercial gliders have a max operating depth of about 1000 m, but there are some experimental models that operate down to 6000 m. Compared to other AUVs, they are relatively slow, typically travelling horizontally between 0.5 to 1 knot (0.25 to 0.5 m/s), but gliders have much longer ranges and mission lifetimes. The typical mission lifetime of a glider is on the order of months, with ranges in the hundreds to thousands of kilometers.

To navigate, gliders are programmed to follow a desired horizontal path through the water, usually defined by a set of waypoints. Gliders communicate by satellite while on the surface through an antenna mounted in either the tail or wings, allowing the transmission of data to the shore and the reception of commands from the operator(s). While on the surface, gliders also get a GPS position update that allows them to correct for any errors in their dead-reckoned position estimates. Without knowledge of their position underwater, currents can cause large position errors between the true position of the vehicle and its estimated position. If properly equipped, gliders can use doppler velocity logs (DVL) to get better estimates of their velocities while underway, but this technique is limited to areas where the glider is within range of the seafloor.

1.2 Applications in Oceanography

Underwater gliders are well-suited for a variety of applications in remote sensing for physical, biological, and chemical oceanography. Commercial applications include use as air-to-water communication gateways, navigation aids, or infrastructure inspection. For military applications, gliders can be used for maritime reconnaissance and tactical oceanography. Gliders can operate individually or in groups and may adjust their missions according to operator instruction or observed sensor information. A particularly promising prospect is the deployment of a fleet of gliders in a region of interest to provide high-resolution, 3-dimensional oceanographic data in near real time.

Gliders have played an important role in collecting data for the development of ocean models, and their importance in understanding the ocean's role in our planet's ecosystem cannot be overstated. The oceans are massive in scale and their dynamics vary both temporally and spatially. Thus, the collection of data at any one point in space and time is typically less useful than over large regions and time scales. Compared to other modern methods for gathering oceanographic data, gliders offer a variety of advantages. Ships are expensive to operate and are limited in number and availability. Fixed moorings gather data at a single point in the ocean, and drifting sensors cannot choose their path through the ocean. Gliders overcome many of these challenges.

Gliders provide an efficient method for accessing certain temporal and spatial scales. Due to their compactness and light weight, they can be deployed from small boats and are especially useful near land where it is more economical to operate. They also provide data that connects coastal and open oceans given their ability to operate in and across both regimes. In short, gliders are a crucial tool for studying the ocean interior that provide complementary information to other available tools.

1.3 Motivation for Study

Despite their widespread use, the nonlinear dynamics of gliders are poorly understood and lack a simple, robust and easy-to-implement control scheme that accounts for modeling uncertainties and environmental disturbances. One barrier is that the analysis of the dynamics of underwater gliders is challenging, because it brings together areas of aerospace and marine engineering in interesting ways. Additionally, the use of internal mass actuators is novel for AUVs and introduces nonlinear control dynamics into the already nonlinear and under-actuated system, making motion control uniquely challenging.

Underwater gliders are usually controlled in the vertical plane (depth) through a combination of open-loop control of their buoyancy and proportional-integral (PI) feedback control of their pitch angle using a moving-mass actuation technique. To steer in the horizontal plane, PI feedback compensation is employed to control the yaw of the vehicle using a rudder and/or the roll of the vehicle using a rotating internal ballast. In typical glider applications, fixed-gain PI compensators are employed; so the compensation feedback gains do not adapt as a function of operating point (e.g., depth, temperature, velocity, angle-of-attack, etc.). It is possible that this fixed-gain approach does not "optimally" compensate for the nonlinear variations of the hydrodynamic forces and moments acting on these vehicles as the operating point evolves.

For general underwater data gathering needs, a fixed-gain control scheme is usually sufficient since the data of interest is in the water column (vertical plane), and there is not much need for complex maneuvers or accurate control of the horizontal path of the vehicle. However, in cases where higher precision control is needed, either to minimize energy consumption or to navigate through complex terrain, a more performant and

robust motion control method is required.

1.4   Literature Review

In 1989, Henry Stommel first presented the concept of underwater gliders [51] in a futuristic narrative story that described a network of mobile oceanic sensors that allowed for unprecedented real-time knowledge about the ocean interior. In pursuit of that dream, researchers have developed various glider designs over the past 30 years, such as the Spray [21], Slocum [27], Seaglider [11], Sea-wing [29], and Petrel [24] gliders. Initial research using gliders involved simple pressure, conductivity, temperature, and density (CTD) sampling, but more recent studies have used gliders to measure chlorophyll fluorescence, acoustic backscatter, internal waves, dissolved oxygen, nitrate, optical backscatter, optical transmission, passive acoustics [15], microstructure temperature and shear [47], oceanic front and eddy formation [23], ocean biogeochemistry [8], and even oil spill plumes [25]. In the past few decades, underwater gliders have proven themselves as useful sensing platforms in oceanographic research.

The operating environment for underwater gliders is time varying and complex. There are many factors in an ocean environment that can adversely affect a glider's performance; therefore, it is important to validate any vehicle's motion control capabilities prior to fielding the system for scientific studies. This control validation is typically done in simulation due to the exorbitant cost of performing regular sea trials. Other benefits of simulation are that one can assess performance reliability across many trials and can change a large number of environmental factors to determine how they would impact performance. In 2001, Leonard and Graver proposed a now-famous dynamic model of an underwater glider based on the momentum and kinetic energy theorems [41]. This model has been widely used in feedback control [34], parameter

identification [6, 13], stability analysis [2], and controller design [12] for underwater gliders.

A wide variety of control strategies have been proposed to control the motion of underwater gliders, such as PID controllers [42, 30], Linear Quadratic Regulators (LQR) [34, 12, 38, 35, 22, 17, 41], sliding mode controllers [52], model predictive controllers [28, 12], feedforward/feedback controllers [16], passivity-based controllers [53], H-infinity controllers [45], fuzzy controllers [26, 20], adaptive controllers based on a backstepping technique [14], neural network based controllers [12, 36], and homeostatic controllers [37, 39]. Although some of these methods rely on dynamically changing the gains of PID controllers, they require significant and potentially costly changes to the overall control structure, rather than using previously derived gain tables which is commonly done in a wide array of industries [50].

Gain-scheduling refers to techniques in which intuitive linear modeling and control synthesis techniques are leveraged for nonlinear control design problems [50]. Although thinly discussed in academic literature prior to 1990, gain scheduling has been used since at least the 1950s on systems ranging from auto-pilots for planes and missiles [44] to automotive engines [48]. Gain-scheduling has been used in conventional underwater vehicle control to account for changes in actuator induced forces and moments with speed [3], mitigating the effects of parametric uncertainties on under-actuated UUVs [10], and transitioning between different medium densities for hybrid UUV/UAVs [9]. It is often employed in thruster-based underwater vehicle control to maintain stability, particularly when considering larger velocity dynamics and disturbances [49]. However, this is not the case for underwater gliders. This thesis will fill this knowledge gap and has the potential to improve glider performance in complex terrains, thus laying the foundation for novel oceanic discoveries.

Chapter 2

Modeling and Simulation of the Glider

This chapter details a model of the dynamics of an underwater glider. The glider has a body with fixed wings, a raised tail with a rudder, a buoyancy engine for ballast control, and an internal moving mass. The model is developed from first principles and can be adapted to any glider provided its mass configuration and geometry are defined. For the purposes of this study, a Slocum glider was used. A CAD model of the glider was developed and CFD was used to determine the hydrodynamic coefficients for the vehicle. The 6-DOF dynamical model was coded in Matlab, and a GUI was created for the easy setup of simulation runs and processing of data. Additionally, ocean current and density stratification models were developed and incorporated into the simulation to assess the systems response to environmental disturbances.

2.1 Coordinate Frames and Transformations

2.1.1 Reference Frames

World Frame

The world frame is described by a non-rotating, earth-fixed, North-East-Down (NED) coordinate frame. The origin of the world frame is the initial deployment position of the vehicle. Let $\mathbf{i}$, $\mathbf{j}$, and $\mathbf{k}$ be the unit vectors in the North, East, and Down directions,

respectively, as shown in Figure 2-1. This choice of world frame is consistent with underwater vehicle literature, such as in [31] and others.
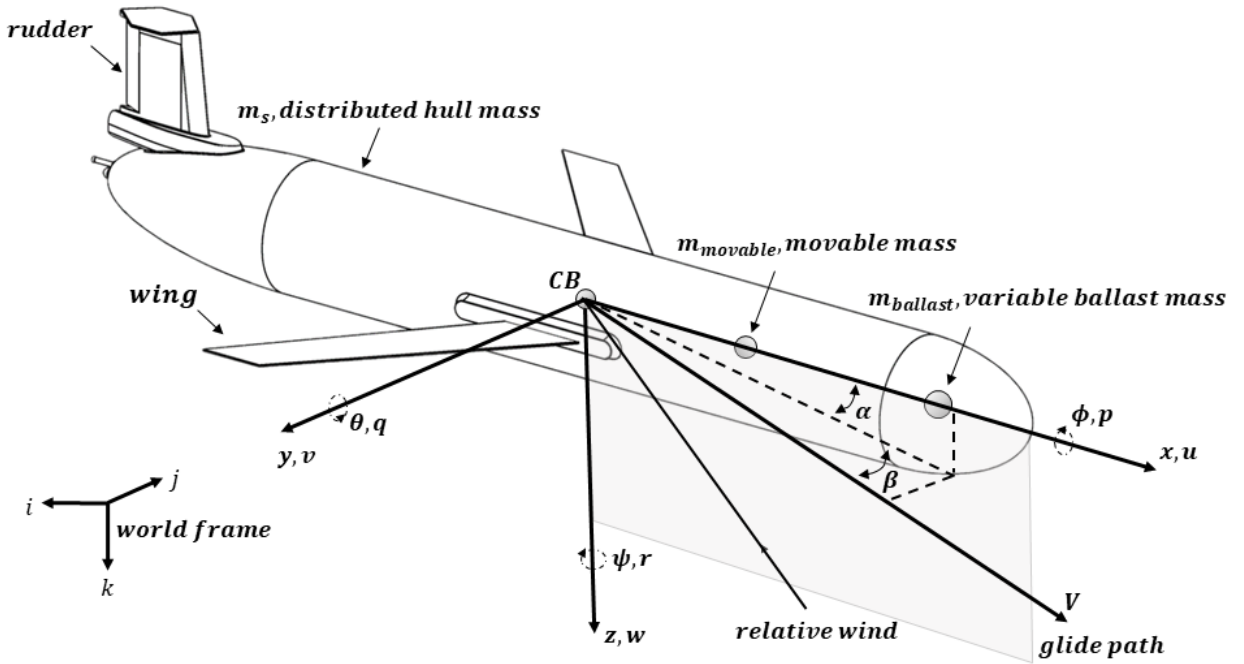
Figure 2-1. Glider world, body and wind frames.

Body Frame

The glider body frame is fixed to the glider vehicle body with its origin at the glider's center-of-buoyancy (CB). The body **x** axis is positive in the direction of the glider's nose, the body **y** axis is positive in the direction of the glider's right wing, and the body **z** axis is orthogonal to both the **x** and **y** axes and is positive out the bottom of the vehicle, as shown in Figure 2-1. The body velocities are defined along the body **x**, **y**, and **z** axes, where surge is u, sway is v, and heave is w, respectively.

Wind Frame

The hydrodynamic forces acting on an underwater vehicle depend on the velocity and orientation of the vehicle relative to the fluid it is moving through. As is standard in aircraft and underwater vehicle literature, the orientation of the wind frame relative

10

to the body frame is described by two aerodynamic angles, the angle-of-attack α, and the angle-of-sideslip β. The wind frame origin is the glider's CB, and α and β are defined such that one axis of the wind frame is aligned with the glider's velocity vector $\mathbf{V}$, as shown in Figure 2-1. The aerodynamic angles are defined as $\alpha = tan^{-1}\left(\frac{w}{u}\right)$ and $\beta = sin^{-1}\left(\frac{v}{V}\right)$.

2.1.2   Transformations

The transformation between the body and world coordinate frames is parameterized by the Euler angles, where ϕ is the roll angle, θ is the pitch angle, and ψ is the yaw angle. Euler angles describe the orientation of the vehicle body frame relative to the world frame through a series of three rigid body rotations about specified coordinate axes. The order of axis rotations is fixed by the choice of an Euler angle convention. The yaw, pitch, roll convention is the standard convention in aircraft and underwater vehicle dynamics, and is used here.

Rotation matrices are used to map vectors expressed in body frame coordinates into world frame coordinates. The three Euler angle rotations are represented by rotation matrices $\mathbf{R}_\psi$, $\mathbf{R}_\theta$, and $\mathbf{R}_\phi$, where:

$$
\mathbf{R}_\psi = \begin{pmatrix} cos\psi & sin\psi & 0 \\ -sin\psi & cos\psi & 0 \\ 0 & 0 & 1 \end{pmatrix}, \mathbf{R}_\theta = \begin{pmatrix} cos\theta & 0 & -sin\theta \\ 0 & 1 & 0 \\ sin\theta & 0 & cos\theta \end{pmatrix},
$$
$$
\mathbf{R}_\phi = \begin{pmatrix} 1 & 0 & 0 \\ 0 & cos\phi & sin\phi \\ 0 & -sin\phi & cos\phi \end{pmatrix}.
$$

$$(2.1)$$

By multiplying the three matrices in the proper order, we obtain the rotation matrix from the world frame to the body frame $\mathbf{R}_{EB} = \mathbf{R}_\phi \mathbf{R}_\theta \mathbf{R}_\psi$:

$$\mathbf{R}_{EB} = \begin{pmatrix} cos\psi cos\theta & sin\psi cos\theta & -sin\theta \\ -sin\psi cos\theta + cos\psi sin\theta sin\phi & cos\psi cos\theta + sin\phi sin\theta sin\psi & cos\theta sin\phi \\ sin\psi sin\phi + cos\psi cos\phi sin\theta & -cos\psi sin\phi + sin\theta sin\psi cos\phi & cos\theta cos\psi \end{pmatrix}$$

$$(2.2)$$

Euler Angle Angular Rates and Gimbal Lock

In order to solve the 6-DOF dynamical equations described in 2.2, we must solve for the Euler angle angular rates. The glider angular velocity with respect to the body frame $\dot{\omega}$ may be written in terms of the Euler angle rates as

$$
\begin{aligned}
\dot{\omega} = \begin{pmatrix} p \\ q \\ r \end{pmatrix} &= \begin{pmatrix} \dot{\phi} \\ 0 \\ 0 \end{pmatrix} + \mathbf{R}_\phi \begin{pmatrix} 0 \\ \dot{\theta} \\ 0 \end{pmatrix} + \mathbf{R}_\phi \mathbf{R}_\theta \begin{pmatrix} 0 \\ 0 \\ \dot{\psi} \end{pmatrix} \\
&= \begin{pmatrix} 1 & sin\phi tan\theta & cos\phi tan\theta \\ 0 & cos\phi & -sin\phi \\ 0 & -sin\phi & cos\theta cos\phi \end{pmatrix} \begin{pmatrix} \dot{\phi} \\ \dot{\theta} \\ \dot{\psi} \end{pmatrix}
\end{aligned}
$$

$$(2.3)$$

Inverting the matrix in Equation 2.3 gives

$$
\begin{pmatrix} \dot{\phi} \\ \dot{\theta} \\ \dot{\psi} \end{pmatrix} = \begin{pmatrix} 1 & sin\phi tan\theta & cos\phi tan\theta \\ 0 & cos\phi & -sin\phi \\ 0 & \frac{sin\phi}{cos\theta} & \frac{cos\phi}{cos\theta} \end{pmatrix} \dot{\omega}
$$

$$(2.4)$$

Note that this transformation is singular for pitch angles where $\theta = \pm 90°$. This phenomenon is known as gimbal lock, and it arises because Euler angles are non-unique. A common method for overcoming gimbal lock is to parameterize a vehicle's orientation using quaternions.

2.1.3 Quaternions

Quaternions parameterize orientation using four parameters and one constraint, which avoids the gimbal lock singularities that can occur with Euler angles. Euler's theory of rotation states that any rigid body rotation may be parameterized by specifying an axis of rotation and a rotation angle about that axis. If we define the unit vector along the axis of rotation to be $\mathbf{c} = (c_1, c_2, c_3)^T$, the rotation angle to be δ, and the quaternion vector as:

$$\mathbf{q} = \begin{pmatrix} q_0 \\ q_1 \\ q_2 \\ q_3 \end{pmatrix} = \begin{pmatrix} cos\frac{\delta}{2} \\ c_1 sin\frac{\delta}{2} \\ c_2 sin\frac{\delta}{2} \\ c_3 sin\frac{\delta}{2} \end{pmatrix} = \begin{pmatrix} cos\frac{\delta}{2} \\ \mathbf{c} sin\frac{\delta}{2} \end{pmatrix} \tag{2.5}$$

where $\mathbf{q}$ is subject to the constraint:

$$\mathbf{q}^T \mathbf{q} = q_0^2 + q_1^2 + q_2^2 + q_3^2 = 1 \tag{2.6}$$

then the corresponding rotation matrix may be written as:

$$\mathbf{R}_{EB} = \begin{pmatrix} q_0^2 + q_1^2 - q_2^2 - q_3^2 & 2(q_1 q_2 + q_0 q_3) & 2(q_1 q_3 + q_0 q_2) \\ 2(q_1 q_2 - q_0 q_3) & q_0^2 - q_1^2 + q_2^2 - q_3^2 & 2(q_2 q_3 + q_0 q_1) \\ 2(q_1 q_3 + q_0 q_2) & 2(q_2 q_3 - q_0 q_1) & q_0^2 - q_1^2 - q_2^2 + q_3^2 \end{pmatrix} \tag{2.7}$$

The quaternion parameters may be written in terms of the Euler angles ϕ, θ, and ψ as:

$$q_0 = cos\frac{\phi}{2}cos\frac{\theta}{2}cos\frac{\psi}{2} + sin\frac{\phi}{2}sin\frac{\theta}{2}sin\frac{\psi}{2} \tag{2.8}$$

$$q_1 = sin\frac{\phi}{2}cos\frac{\theta}{2}cos\frac{\psi}{2} - cos\frac{\phi}{2}sin\frac{\theta}{2}sin\frac{\psi}{2} \tag{2.9}$$

$$q_2 = cos\frac{\phi}{2}sin\frac{\theta}{2}cos\frac{\psi}{2} + sin\frac{\phi}{2}cos\frac{\theta}{2}sin\frac{\psi}{2} \tag{2.10}$$

$$q_3 = cos\frac{\phi}{2}cos\frac{\theta}{2}sin\frac{\psi}{2} - sin\frac{\phi}{2}sin\frac{\theta}{2}cos\frac{\psi}{2} \tag{2.11}$$

The Euler angles may be found directly from the quaternion parameters as follows:

$$tan\phi = \frac{2(q_0q_1 - q_2q_3)}{q_0^2 - q_1^2 - q_2^2 + q_3^2} \tag{2.12}$$

$$sin\theta = 2(q_0q_2 - q_3q_1) \tag{2.13}$$

$$tan\psi = \frac{2(q_1q_2 + q_0q_3)}{q_0^2 + q_1^2 - q_2^2 - q_3^2} \tag{2.14}$$

The quaternion rates may be written in terms of the body angular velocity $\dot{\omega}$ and the quaternion parameters as:

$$\begin{pmatrix} \dot{q_0} \\ \dot{q_1} \\ \dot{q_2} \\ \dot{q_3} \end{pmatrix} = \frac{1}{2} \begin{pmatrix} 0 & -p & -q & -r \\ p & 0 & r & -q \\ q & -r & 0 & p \\ r & q & -p & 0 \end{pmatrix} \begin{pmatrix} q_0 \\ q_1 \\ q_2 \\ q_3 \end{pmatrix} \tag{2.15}$$

Finally, the vehicle angular rates may be written in the body frame as a function of the quaternion rates as:

$$\begin{pmatrix} p \\ q \\ r \end{pmatrix} = 2 \begin{pmatrix} -q_1 & q_0 & q_3 & -q_2 \\ -q_2 & -q_3 & q_0 & q_1 \\ -q_3 & q_2 & -q_1 & q_0 \end{pmatrix} \begin{pmatrix} \dot{q_0} \\ \dot{q_1} \\ \dot{q_2} \\ \dot{q_3} \end{pmatrix} \tag{2.16}$$

2.2 Dynamics Model Derivation

The dynamic equations of motion for underwater gliders can be developed from Newton's second law, which states that the changes of momentum are due to the accumulated external forces and torques. Defining $\mathbf{F}$ as the external forces, $\mathbf{T}$ as the external torques, $\mathbf{m}$ and $\mathbf{J}$ as the mass and moment of inertia vectors respectively, and v and ω as the linear and angular velocity vectors respectively, this can be expressed generally as:

$$\mathbf{m} \cdot \dot{v} = \sum \mathbf{F} \tag{2.17}$$

$$\mathbf{J} \cdot \dot{\omega} = \sum \mathbf{T} \tag{2.18}$$

Recognizing that the time derivative of momentum is the force acting upon it ($\mathbf{F} = \frac{d\mathbf{p}}{dt}$), Equations 2.17 and 2.18 can be rearranged and combined into Equation 2.19 to fully describe the vehicle's dynamics

$$\begin{pmatrix} \dot{v} \\ \dot{\omega} \end{pmatrix} = \mathbb{I}^{-1} \begin{pmatrix} \dot{\mathbf{P}} \\ \dot{\mathbf{L}} \end{pmatrix} \tag{2.19}$$

where $\mathbf{P}$ and $\mathbf{L}$ represent the linear and angular momentum matrices, respectively, and $\mathbb{I}$ is a 6x6 inertia matrix shown in Equation 2.20

$$\mathbb{I} = \begin{pmatrix} \mathbf{M}_{3x3} & \mathbf{C}_{3x3} \\ \mathbf{D}_{3x3} & \mathbf{J}_{3x3} \end{pmatrix} \tag{2.20}$$

In Equation 2.20, $\mathbf{M}_{3x3}$ represents the mass matrix of the vehicle which includes the added mass ($\mathbf{M}_{added}$) of the fluid acting on the body, and $\mathbf{J}_{3x3}$ is the moment of inertia matrix which includes the added moment of inertia ($\mathbf{J}_{added}$). $\mathbf{C}_{3x3}$ and $\mathbf{D}_{3x3}$ are the cross term matrices that only include the cross term effects of the variable and moving masses. The glider is assumed to be operating at low angle of attack; therefore, the

hydrodynamic effects are largely dominated by the lift and drag forces. Due to this, the added mass and moments of inertia can be assumed diagonal and can be neglected in the cross term matrices [41].

Based on rigid body dynamics [54], the linear momentum cross term created by the rotation of the ballast mass can be calculated using Equation 2.21

$$\mathbf{P}_m = m \cdot v = m\omega \times \mathbf{r} = -m\mathbf{r} \times \omega = -m\hat{\mathbf{r}}\omega \tag{2.21}$$

where $\mathbf{r}$ is the displacement vector of the mass m in the body frame. Similarly, the angular momentum cross term of the ballast mass can be calculated using Equation 2.22

$$\mathbf{L}_m = \mathbf{r} \times \mathbf{P} = \mathbf{r} \times (mv) = m\mathbf{r} \times v = m\hat{\mathbf{r}}v \tag{2.22}$$

Thus, the cross matrices in the inertia matrix $\mathbb{I}$ can be calculated as in Equations 2.23 and 2.24.

$$\mathbf{C}_{3x3} = -\sum m_{ballast}\hat{\mathbf{r}}_{ballast} - \sum m_{movable}\hat{\mathbf{r}}_{movable} \tag{2.23}$$

$$\mathbf{D}_{3x3} = \sum m_{ballast}\hat{\mathbf{r}}_{ballast} + \sum m_{movable}\hat{\mathbf{r}}_{movable} \tag{2.24}$$

Furthermore, the ballast and movable masses create additional moments of inertia in the moment of inertia matrix J_{3x3}. For a single ballast mass (m), the moment of inertia can be expressed as

$$\mathbf{L}_m = \mathbf{r} \times \mathbf{P} = \mathbf{r} \times mv = m\mathbf{r} \times v$$
$$= m\mathbf{r} \times (\omega \times \mathbf{r}) \tag{2.25}$$
$$= -m\mathbf{r} \times (\mathbf{r} \times \omega) = -m \cdot \hat{\mathbf{r}} \cdot \hat{\mathbf{r}} \cdot \omega$$

which gives the representation for J_{3x3} shown in Equation 2.26.

$$\mathbf{J}_{3x3} = \mathbf{J}_s + \mathbf{J}_{added} - \sum m_{ballast} \cdot \hat{\mathbf{r}}_{ballast} \cdot \hat{\mathbf{r}}_{ballast} - \sum m_{movable} \cdot \hat{\mathbf{r}}_{movable} \cdot \hat{\mathbf{r}}_{movable} \tag{2.26}$$

where $\mathbf{J}_s$ is the moment of inertia of the fixed masses in the vehicle. The mass matrix for the vehicle is shown in Equation 2.27.

$$\mathbf{M}_{3x3} = (\sum m_s + \sum m_{ballast} + \sum m_{movable})\mathbf{I}_{3x3} + \mathbf{M}_{added} \tag{2.27}$$

With the inertia matrices defined, all that is left to complete the model is the formulation of the linear and angular momentum terms. To start, the transformation between the body and world frame must be considered to account for the effect of gravity on the ballast masses in the system. The transformation is shown in Equations 2.28 and 2.29.

$$\mathbf{p} = \mathbf{R}_{BE}\mathbf{P} \tag{2.28}$$

$$\mathbf{l} = \mathbf{R}_{BE}\mathbf{L} + \mathbf{b} \times \mathbf{p} \tag{2.29}$$

where $\mathbf{p}$ and $\mathbf{l}$ are the world frame linear and angular momenta, respectively, and $\mathbf{b}$ is the displacement of masses in the world frame. Taking the derivative of Equations 2.28 and 2.29 gives Equations 2.30 and 2.31

$$\dot{\mathbf{p}} = \mathbf{R}_{BE}\dot{\mathbf{P}} + \mathbf{R}_{BE}\hat{\omega}\mathbf{P} = \mathbf{f}_{ext} + \sum \mathbf{f}_{gi} \tag{2.30}$$

$$\dot{\mathbf{l}} = \mathbf{R}_{BE}\dot{\mathbf{L}} + \mathbf{R}_{BE}\upsilon \times \mathbf{P} + \mathbf{b} \times \mathbf{P} = \mathbf{t}_{ext} + \sum_{i=1}^{n}(\mathbf{b}_i \times \mathbf{f}_{gi}) \tag{2.31}$$

where $\mathbf{f}_{ext}$ and $\mathbf{t}_{ext}$ are the hydrodynamic forces and torques in the world frame, and $\mathbf{f}_{gi}$ is the gravitational force of a mass m_i in the world frame. Rearranging the terms in Equations 2.30 and 2.31, we can obtain expressions for the rate of change of the linear and angular momenta in the body frame.

$$\dot{\mathbf{P}} = \mathbf{P} \times \omega + \mathbf{R})EB\dot{\mathbf{p}} = \mathbf{P} \times \omega + m_0 g\mathbf{R}_{EB}\mathbf{k} + \mathbf{R}_{WB}\mathbf{F}_{ext} \tag{2.32}$$

$$\dot{\mathbf{L}} = \mathbf{L} \times \omega - \hat{\upsilon}\mathbf{P} + \mathbf{R}_{EB}(\sum_{i=1}^{n}(\mathbf{b}_i - \mathbf{b}) \times \mathbf{f}_{gi} + \mathbf{t}_{ext}) \tag{2.33}$$

In Equation 2.33, $\mathbf{b}_i$ is the displacement of m_i in the world frame, while $\mathbf{b}$ is the displacement of the origin of the body frame in the world frame. Therefore, $\mathbf{b}_i - \mathbf{b}$

represents the displacement of m_i in the body frame, and $(\mathbf{b}_i - \mathbf{b}) \times \mathbf{f}_{gi}$ represents the torque created by the gravitational forces acting on the various masses in the system. Consequently, Equation 2.33 can be rewritten as

$$\dot{\mathbf{L}} = \mathbf{L} \times \omega - \hat{\upsilon}\mathbf{P} + \left(\sum m_{ballast}\mathbf{r}_{ballast} + \sum m_{movable}\mathbf{r}_{movable}\right) \times g\mathbf{R}_{EB}\mathbf{k} + \mathbf{R}_{WB}\mathbf{T}_{ext} \quad (2.34)$$

where $\mathbf{F}_{ext}$ and $\mathbf{T}_{ext}$ are the hydrodynamic forces and torques in the body frame.

Finally, using Equations 2.21 and 2.22, it can be shown that the linear and angular momenta in the body frame can be represented by Equations 2.35 and 2.36.

$$\mathbf{P} = \mathbf{M}_{added} \cdot \upsilon + \sum m_s \upsilon + \sum m_{ballast}(\upsilon + \hat{\omega}\mathbf{r}_{ballast}) + \sum m_{movable}(\upsilon + \hat{\omega}\mathbf{r}_{movable}) \quad (2.35)$$

$$\mathbf{L} = \mathbf{J}_{added}\omega + \sum m_s\omega + \sum m_{ballast}\hat{\mathbf{r}}_{ballast}(\upsilon + \hat{\omega}\mathbf{r}_{ballast})$$
$$+ \sum m_{movable}\hat{\mathbf{r}}_{movable}(\upsilon + \hat{\omega}\mathbf{r}_{m}ovable) \quad (2.36)$$

Thus, $\dot{\mathbf{P}}$ and $\dot{\mathbf{L}}$ can be solved by substituting Equations 2.35 and 2.36 into Equations 2.32 and 2.33.

The viscous forces and moments are included in $\mathbf{F}_{ext}$ and $\mathbf{T}_{ext}$,

$$\mathbf{F}_{ext} = \begin{pmatrix} -D \\ SF \\ -L \end{pmatrix} \quad and \quad \mathbf{T}_{ext} = \begin{pmatrix} M_{DL_1} \\ M_{DL_2} \\ M_{DL_3} \end{pmatrix}, \quad (2.37)$$

where D, L, and SF represent the hydrodynamic drag, lift, and side forces, respectively, and M_{DL_i} are the hydrodynamic moments. This use of a simplified coefficient-based model helps to include important aspects of the vehicle dynamics, while using a small set of parameters so that the model is amenable to control theory tools. The values for these forces and moments will be derived using CFD simulations, which is further described in Section 2.3.

2.2.1 Equation Summary

Given the states $[u, v, w, p, q, r]^T$, where $\upsilon = [u, v, w]^T$ represents the body-frame axial velocities, and $\omega = [p, q, r]^T$ represents the body-frame rotational rates, a dynamic model for an underwater glider can be expressed as in Equations 2.38 - 2.46.

$$\dot{\upsilon} = \begin{pmatrix} \dot{u} \\ \dot{v} \\ \dot{w} \end{pmatrix} \tag{2.38}$$

$$\dot{\omega} = \begin{pmatrix} \dot{p} \\ \dot{q} \\ \dot{r} \end{pmatrix} \tag{2.39}$$

$$\mathbb{I} = \begin{pmatrix} \mathbf{M}_{3x3} & \mathbf{C}_{3x3} \\ \mathbf{D}_{3x3} & \mathbf{J}_{3x3} \end{pmatrix} \tag{2.40}$$

$$\mathbf{M}_{3x3} = \left(\sum m_s + \sum m_{ballast} + \sum m_{movable}\right)\mathbf{I}_{3x3} + \mathbf{M}_{added} \tag{2.41}$$

$$\mathbf{C}_{3x3} = -\sum m_{ballast}\hat{\mathbf{r}}_{ballast} - \sum m_{movable}\hat{\mathbf{r}}_{movable} \tag{2.42}$$

$$\mathbf{D}_{3x3} = \sum m_{ballast}\hat{\mathbf{r}}_{ballast} + \sum m_{movable}\hat{\mathbf{r}}_{movable} \tag{2.43}$$

$$\mathbf{J}_{3x3} = \mathbf{J}_s + \mathbf{J}_{added} - \sum m_{ballast} \cdot \hat{\mathbf{r}}_{ballast} \cdot \hat{\mathbf{r}}_{ballast} - \sum m_{movable} \cdot \hat{\mathbf{r}}_{movable} \cdot \hat{\mathbf{r}}_{movable} \tag{2.44}$$

$$\dot{\mathbf{P}} = \left[\mathbf{M}_{added} \cdot \upsilon + \sum m_s \upsilon + \sum m_{ballast}(\upsilon + \hat{\omega}\mathbf{r}_{ballast}) + \sum m_{movable}(\upsilon + \hat{\omega}\mathbf{r}_{movable})\right] \times \omega$$
$$+ m_0 g \mathbf{R}_{EB} k + \mathbf{R}_{WB}\mathbf{F}_{ext} \tag{2.45}$$

$$\dot{\mathbf{L}} = [\mathbf{J}_{added}\omega + \sum m_s\omega + \sum m_{ballast}\hat{\mathbf{r}}_{ballast}(\upsilon + \hat{\omega}\mathbf{r}_{ballast})] \times \omega$$

$$-\hat{\upsilon}[\mathbf{M}_{added} \cdot \upsilon + \sum m_s\upsilon \sum m_{ballast}(\upsilon + \hat{\omega}\mathbf{r}_{ballast}) + \sum m_{movable}(\upsilon + \hat{\omega}\mathbf{r}_{movable})]$$

$$+(\sum m_{ballast}\mathbf{r}_{ballast} + \sum m_{movable}\mathbf{r}_{movable}) \times g\mathbf{R}_{EB}\mathbf{k} + \mathbf{R}_{WB}\mathbf{T}_{ext}$$

$$(2.46)$$

These equations will be used to develop the nonlinear simulation of the glider dynamics as well as to derive the linearized equations of motion used for control system synthesis.

2.3   Deriving Nonlinear Hydrodynamic Coefficients

The forces and moments represented by Equations 2.38 - 2.46 illustrate the coupled, nonlinear response characteristics of a general underwater glider. In order to represent a specific vehicle, the mass distribution and geometry of the vehicle must be defined, as well as the hydrodynamic coefficients described in Equation 2.37. This model can then be used as a "truth" simulation for analysis purposes, as well as controller design and synthesis. The geometry of the Slocum glider was estimated from published work [4] and the Slocum G2 Operators Manual [46]. Detailed measurements of the tail and rudder were taken in-person by the author.

There are several methods for determining the hydrodynamic coefficients of a vehicle based on a given geometry. In the case of underwater gliders, analytical [2], experimental [34, 13] and computational [32] approaches have been used. All prior work has assumed that the coefficients are linear with respect to the angle-of-attack and angle-of-sideslip, and linear estimation methods were used based on a few data points. However, the assumption that the hydrodynamic coefficients are linear is only relevant when the vehicle is in a steady glide. During inflection points, when the vehicle changes glide direction by ingesting or expelling water from the buoyancy engine,

the vehicle sees much higher angles-of-attack due to the direction of flow around the vehicle changing rapidly. Additionally, it is possible that a vehicle may encounter high angles-of-sideslip as it maneuvers through high-current regions of the ocean. During these high angle maneuvers, nonlinear relationships develop between the coefficients and angles of attack and sideslip.

In order to fully capture the nonlinear relationships between the hydrodynamic coefficients shown in 2.37 and the angles of attack and sideslip, a CAD model of the Slocum vehicle was developed in Solidworks, and computational flight tests were performed using Solidworks Flow Simulation to determine the forces and moments acting on the vehicle. This section describes the CAD model of the Slocum glider (Section 2.3.1), the methodology used for performing computational flight tests of the vehicle (Section 2.3.2), and analyzes the resulting nonlinear hydrodynamic coefficients (Section 2.3.3).

2.3.1 CAD Model of the Slocum Glider

The Slocum glider has a cylindrical hull comprised of multiple sections that lock together to form a pressure vessel. The nose end cap is free-flooded and has an ellipsoidal shape to minimize drag and protect the buoyancy engine bladder. The rear tail cap is also free flooded and has a tapered truncated conical shape to minimize drag and houses various components outside of the main hull, such as the sacrificial anode and a jettison weight for emergency recovery. The raised tail fin sits above the tapered section of the vehicle and contains three antennas for communications and tracking. The tail fin has a hydrofoiled profile to minimize drag, with fixed horizontal stabilizers and a rudder for steering control. The wings of the glider are attached near the center of the vehicle with a slotted quick-release system that clicks into place.

21

The Slocum G2 glider is shown in Figure 2-2a with an optional propeller that was not considered in the dynamical or CAD model for this study. An exploded view of the glider internals is shown in Figure 2-2b.

(a) Slocum G2 Glider Exterior
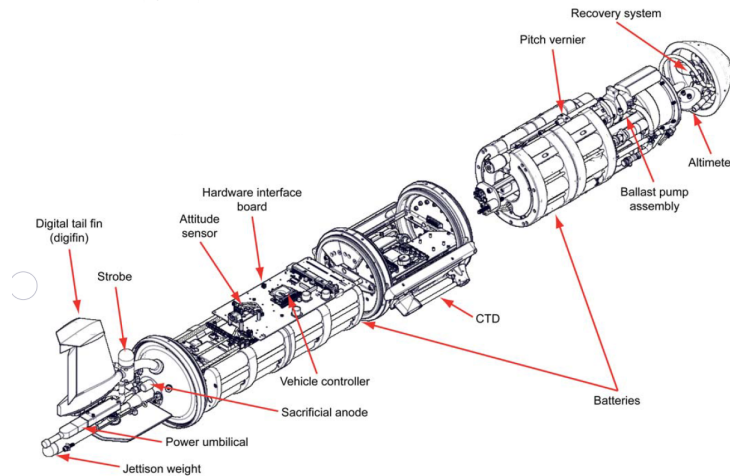
(b) Slocum G2 Internals [46]

Figure 2-2. Slocum G2 Glider

Some dimensions of the CAD model are shown in Figure 2-3. Additional dimensional drawings can be found in Appendix A. The cylindrical portion of the hull is 47.61 in. in length with an external diameter of 8.37 in. The nose section is 8.27 in. long, and the tail section is 14.24 in., giving the vehicle a total length of 70.14 in. The tail

22

section tapers from the external diameter of the hull to 1.73 in. at the rear of the vehicle. The raised fin section is 10.21 in. long and 6.83 in. tall. The wings are swept back at a 45° angle and protrude from the hull by 14.69 in. on both sides, giving the vehicle a total width of 37.75 in.
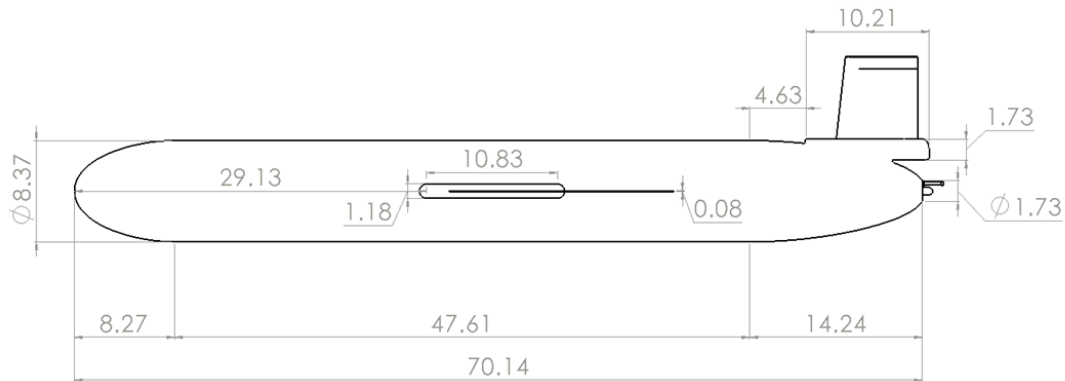
(a) Slocum Hull Dimensions [in.]
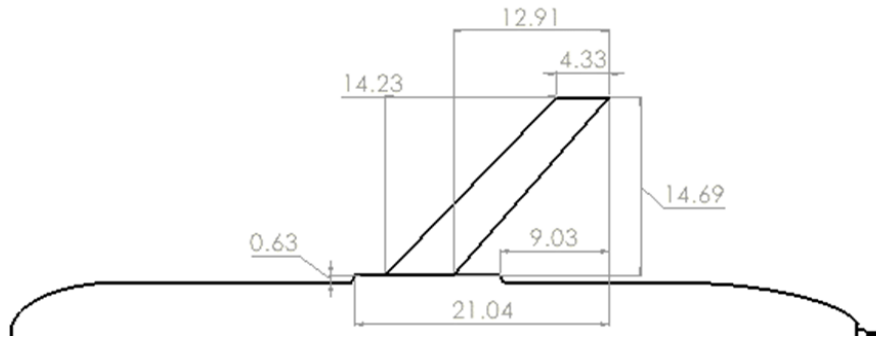
(b) Slocum Wing Dimensions [in.]

Figure 2-3. Slocum CAD Model Dimensions

The CAD model contains some simplifications from the real vehicle, namely in the quick-release wing attachment point on the side of the hull, and in the tail section. On the real system, the quick-release mechanism is slotted and can house small weights for ballasting the glider. As shown in Figure 2-4, the wing attaches directly to the side of the glider through a raised attachment point. The dimensions of the attachment point are similar to that of the quick-release mechanism, but the slot in which the wing is typically fitted into was filled in. In Figure 2-5, the modeled fin section can be

23

seen to attach directly to the tail cover. In reality, there is a small tube that attaches the fin to the main hull and houses the antenna feed cables. There are also small slots that run alongside the fin that allow water to free-flood the rear section of the vehicle. These details were removed from the model to simplify the CFD mesh and speed up the solve time.
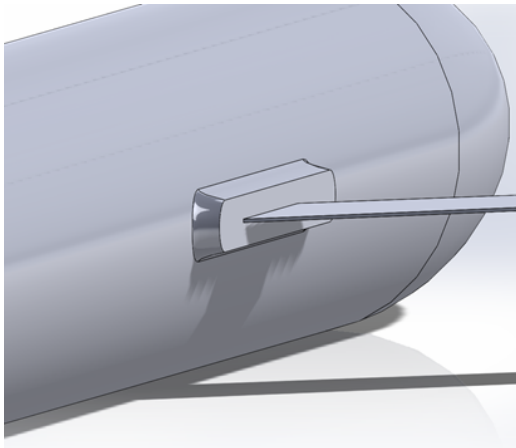
Figure 2-4. Slocum CAD Wing Detail
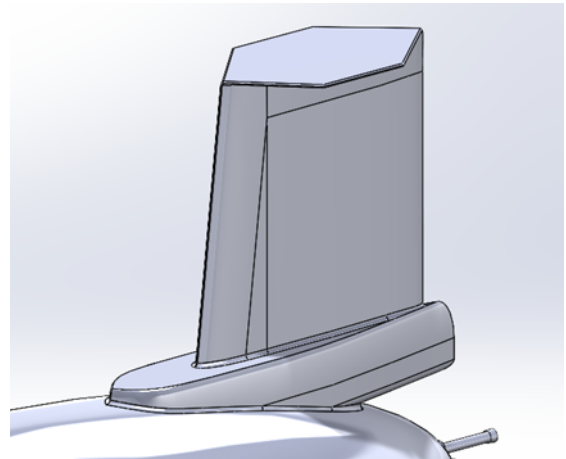
Figure 2-5. Slocum CAD Tail Detail

It's expected that these minor differences between the model and the real glider would have a minimal effect on the calculated drag coefficient, but would not cause major differences in the other coefficients. As the main purpose of the computational flight tests was the determination of the nonlinear relationships between hydrodynamic coefficients and the vehicle's operating point over a wide range of angles of attack and sideslip, these small differences were deemed to be acceptable due to the large number of runs needed to characterize the hydrodynamics of the vehicle and the increase in time needed to resolve the effects of these small details in the CFD software. One additional note about the CAD model are the small protrusions off the back of the tail section. These were added to visually show the jettison weight and a tail connector, but were explicitly excluded from the CFD mesh for the same reason as discussed above.

2.3.2 Computational Flight Tests

In order to identify the nonlinear hydrodynamic coefficients of the vehicle, Solidworks Flow Simulation was used to perform computational flight tests on the CAD model described above. A local mesh was applied to all surfaces of the model (excluding the minor elements on the rear face of the tail), and a 3-dimensional computation domain was defined about the vehicle, as shown in Figure 2-6. A laminar flow of water was defined at atmospheric pressure and average sea surface temperature of 20°C and set to flow in the negative Z direction at 0.5 m/s at varying angles of attack and sideslip. The outputs of the simulations were the forces and torques acting on and about the X, Y, and Z axes with respect to the CB of the vehicle. A full listing of the Flow Simulation settings can be found in Appendix B.
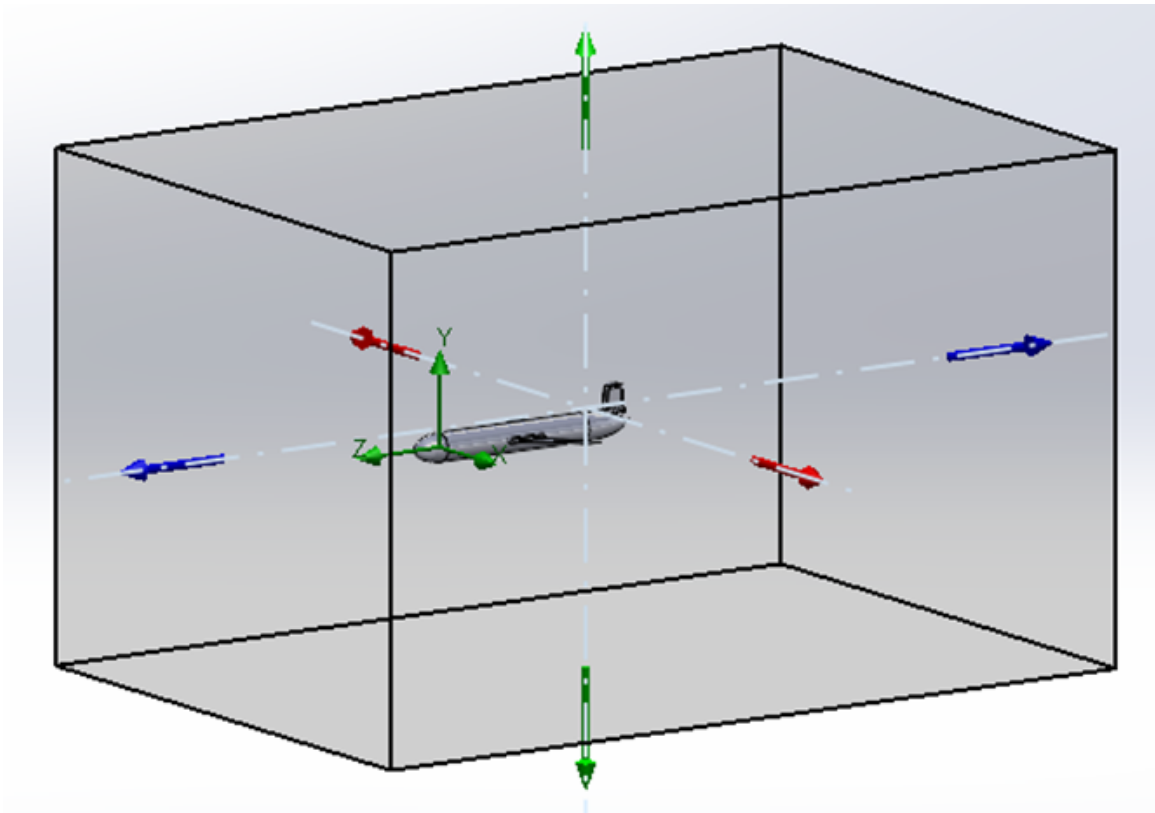
Figure 2-6. CFD Computation Domain

Solidworks Flow Simulation can automatically refine the global and local meshes on selected surfaces. After some trial and error, it was found that minimal differences in the force and moment values occurred after two refinements had occurred, giving an approximate cell count of 2,000,000. Additionally, it was found that the values reached a steady-state around 500 iterations. Due to the large number of runs needed to fully characterize the hydrodynamic coefficients, the simulations were set up to stop after 500 iterations in order to save time. The average run time for a single run was 1.5 hours.
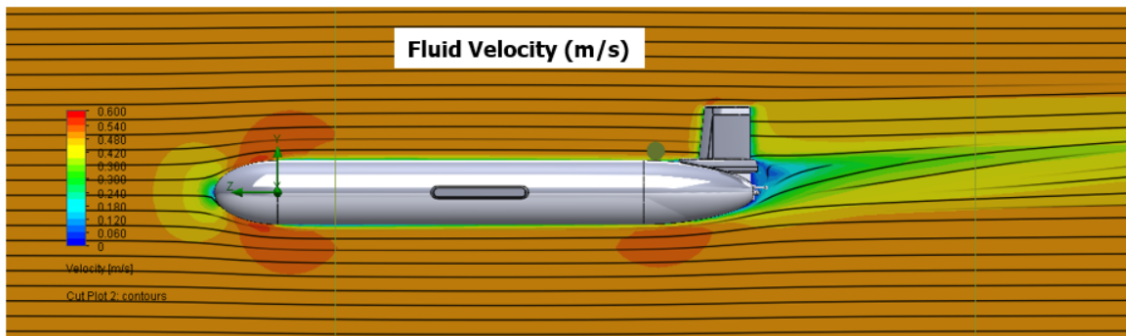
Figure 2-7. Computational Flight Test Example [Side View]

An example of the flow about the vehicle with 0° angle-of-attack is shown in Figure 2-7. Low pressure regions can be seen at the nose and trailing the vehicle as it moves through the fluid. Runs were repeated with the rudder set to 20° in order to characterize the changes in the hydrodynamic coefficients due to rudder actuation. An example of the effect of the rudder on the flow can be seen in Figure 2-8. This example is a top-down view of a 2-dimensional cut that passes through the raised tail fin and had 0° angle-of-attack and 30° angle-of-sideslip. A strong low pressure region can be seen on the starboard side of the fin with trailing vortices shedding behind the vehicle. The effects of the glider body and wings on the flow can also be seen in the red colored section on the left of the image.
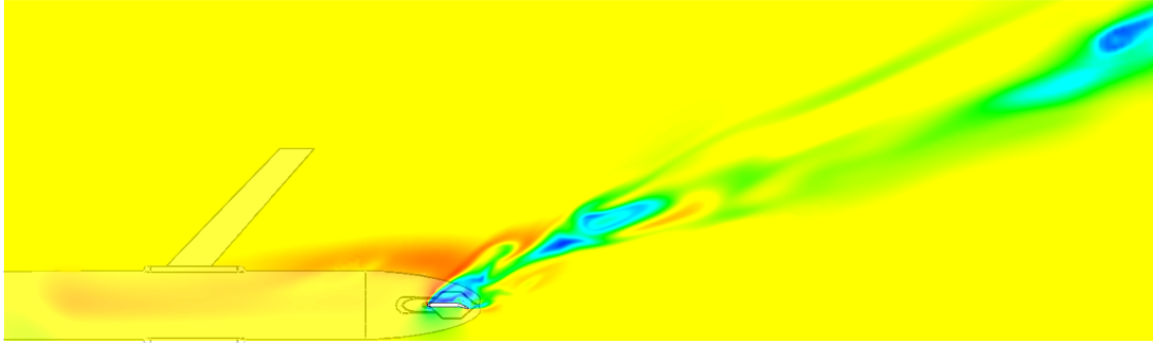
Figure 2-8. Rudder Flow Example [Top-Down View]

2.3.3 Hydrodynamic Coefficients

In order to determine the nonlinear relationships between the hydrodynamic coefficients and the vehicle's angles of attack and sideslip, a number of simulations were run with varying combinations of values for the aerodynamic angles ranging from -30° to +30°. An example table of aerodynamic angles is shown in Table 2-I, and the complete tables for all hydrodynamic coefficients can be found in Appendix C. These runs were repeated with the rudder rotated to 20° to asses how the rudder would effect the forces and moments acting on the vehicle.

Table 2-I. Aerodynamic Angle Permutations

The forces and moments output from Solidworks Flow Simulation were in Newtons

and Newton-seconds, respectively, and were in the simulation coordinate system seen in Figure 2-6. The output values were exported to Excel and rotated to the body frame coordinate system described in Section 2.1.1. The values were then normalized with respect to the fluid velocity and angles of attack and sideslip. The rotated and normalized values are what is shown in Appendix C. The values contained in these tables were then interpolated using the Akima method [1] to 0.1° precision and a lookup table was generated for use in the 6-DOF simulation. Surface plots showing the interpolated coefficients can be found in Appendix C.
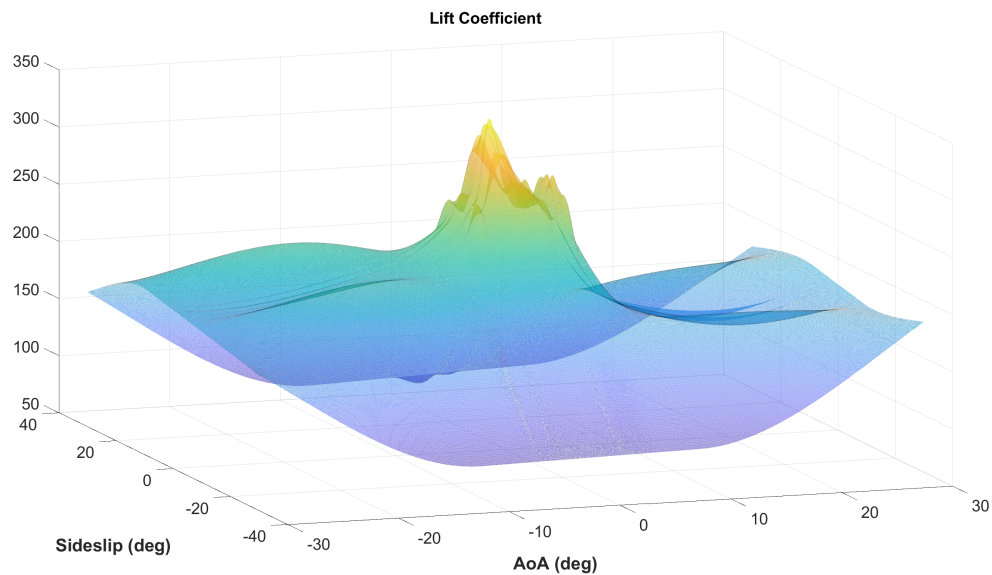
Figure 2-9. Lift Coefficient wrt AoA and AoS

Viewing the coefficients graphically can give a more intuitive understanding of the usefulness of this technique. Figure 2-9 shows a surface plot of the interpolated lift coefficient with respect to the aerodynamic angles. It can be seen that in small regions the lift coefficient is mostly linear, but over the entire space it is highly nonlinear. The most lift is generated between $\pm 10°$ AoA and AoS, with modest lift generated outside of that operating region. The lift also appears to be asymmetric, with more lift being generated with negative AoAs than positive. This is likely due to the raised tail fin

effecting the lift generation when the fluid is impacting the top of the vehicle versus the bottom of the vehicle.
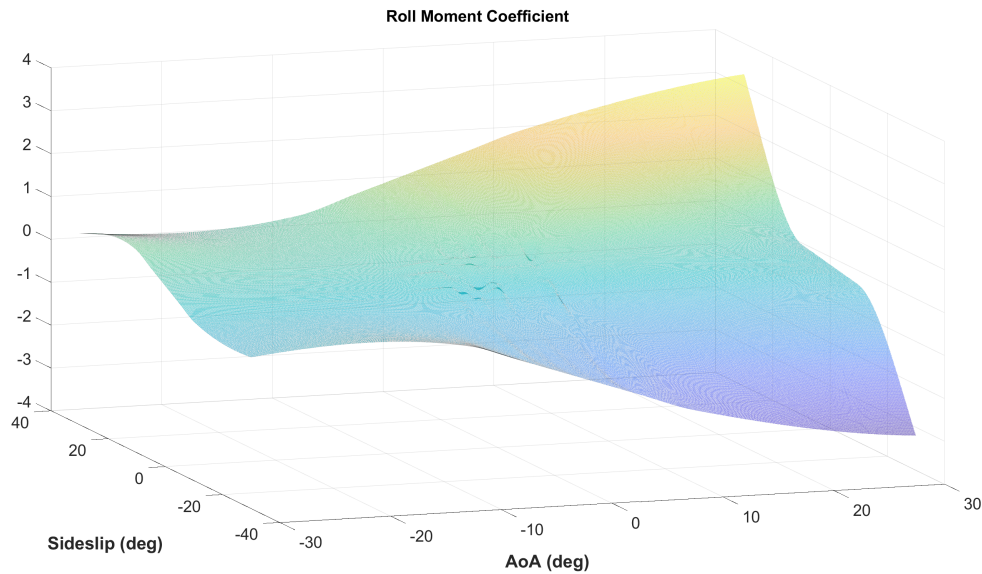
Figure 2-10. Roll Moment Coefficient wrt AoA and AoS

As expected, the addition of a rudder results in significant changes to the side force and yaw moment coefficients (found in Appendix C); however, there are additional effects on the roll and pitch moment coefficients that demonstrate the yaw-roll-pitch coupling present in the vehicle. Figures 2-10 and 2-11 show the roll moment coefficient without and with the rudder, respectively. It can be seen that the rudder imparts small, but not insignificant, roll torques on the vehicle when it is actuated. This is not surprising given the high tail fin design that is above the axial center of the vehicle. This effect has also been described by others in [34] and [54].

The effects of the rudder on the vehicle are also nonlinear, adding another layer of complexity to the model that linearized hydrodynamic coefficients overlook. In order to characterize this effect, simulations were run with straight flow (i.e. no angle-of-attack or angle-of-sideslip) and the rudder angle was increased to 30° in
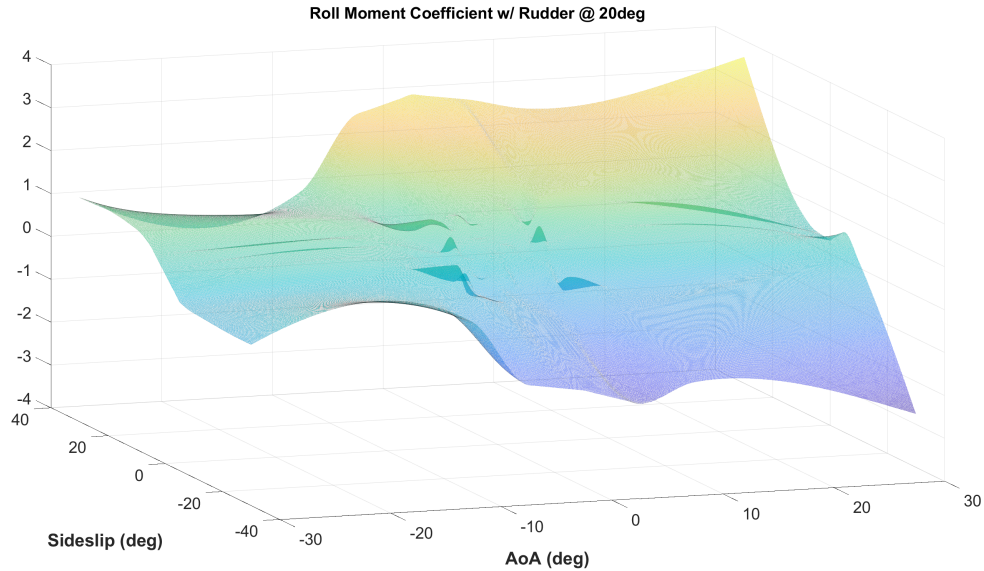
Figure 2-11. Roll Moment Coefficient With Rudder wrt AoA and AoS

5° increments. The resulting yaw moment coefficient was then used to estimate a representative polynomial function that was used to scale the rudder effects in the 6-DOF simulation. This process is described in more detail in Section 2.4.1. The results from the rudder characterization simulations are shown in Figure 2-12. The black line shows the raw data, the dotted blue line shows the polynomial fit calculated by Excel, and the dashed red line shows the relationship used in the 6-DOF simulation, which is the same polynomial fit equation, but shifted downward to cross through 0 at the y-axis.

2.4 Matlab Simulation

The glider was simulated in Matlab to due to its diverse array of ordinary differential equation (ODE) solvers, wide variety of tools for data analysis and visualization, and to allow for quick and easy development of different control topologies. A high-level block diagram of the simulation architecture is shown in Figure 2-13. A graphical user interface (GUI) was developed to allow for easy setup and management of the
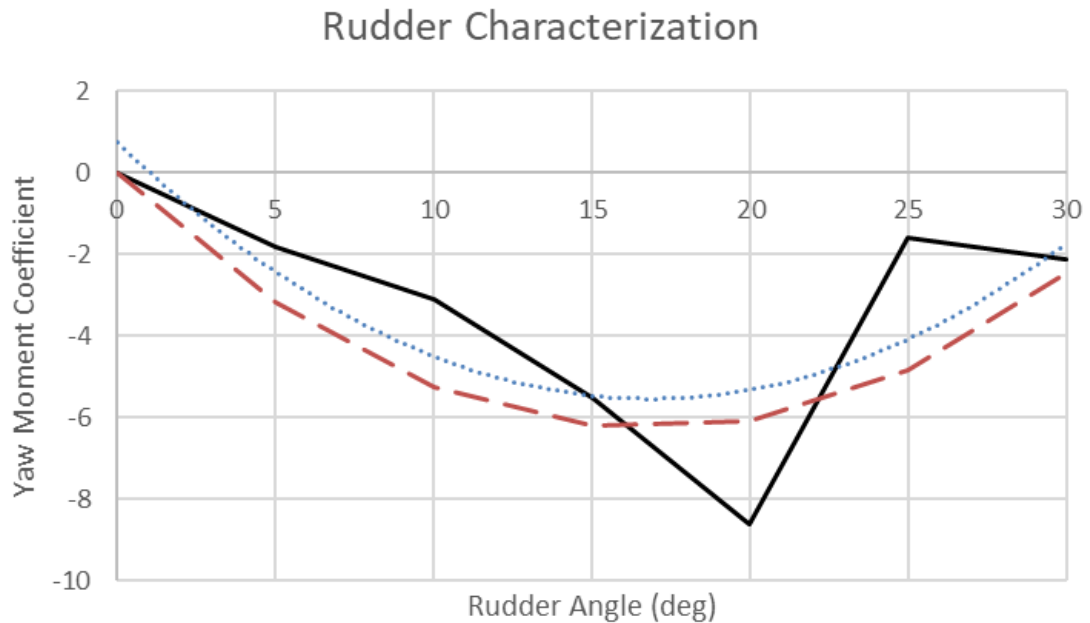
Figure 2-12. Yaw Moment Coefficient wrt Rudder Angle

simulations. Using the GUI, simulations could be set up by the user and queued to allow for multiple simulations to run and be compared after completion. Each simulation could be configured with different dynamics, control topologies, environmental disturbances, and other relevant control logic. The simulated glider was controlled by a guidance, navigation and control (GNC) object that handled transitioning through the glider's state machine, estimating the glider's position and velocities, and managing the simulated actuators.

Each simulation is setup to run for some pre-allotted amount of time or until a waypoint goal is reached. A flow chart of the simulation process is shown in Figure 2-14. The actuators and state of the vehicle are initialized, then the equations of motion shown in Section 2.2.1 are solved using the ode45 function in Matlab. The ODE solver automatically determines how many time steps are needed to meet a user defined tolerance, but on average the equations are solved at approximately 30Hz.

Figure 2-13. Simulation Architecture Block Diagram

The final state values the solver outputs are clocked to 1Hz, and those values are used to simulate the sensors on the vehicle. From there, the GNC is updated, data is logged for plotting, and the AoA and AoS are used to select the hydrodynamic coefficients for the next iteration. The process repeats until the end condition is met.

The GNC update is shown on the right in Figure 2-14. Each iteration, the GNC object ingests the simulated glider state and uses those values to update the simulated sensors. The velocity and position of the vehicle are estimated based on the sensor values. This architecture allows for the development and testing of multiple navigation filters; however, for the purposes of this study straightforward estimates for velocity and position are used based on basic trigonometry. This is described in more detail in Section 2.4.2. Based on the estimated state of the vehicle, the simulated glider transitions through a sequence of modes: **Glide Up**, **Inflect Down**, **Glide Down**, **Inflect Up**. These modes instruct the Control object to move the actuators in an open or closed loop fashion to the correct locations. Finally, the range and bearing to the waypoint, and the simulated actuator positions are calculated and output to the simulation object to pass into the ODE solver.

32
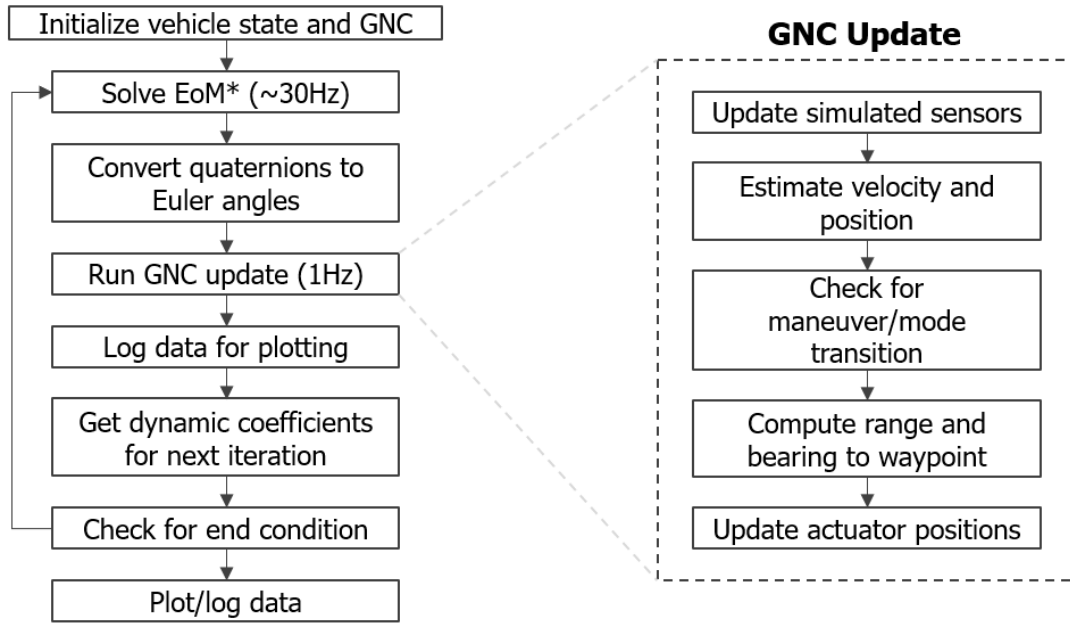
Figure 2-14. Simulation Update Flow Chart

The glider state machine is shown in Figure 2-15. The glider initially starts in **Glide Down**, which sets the buoyancy engine (BE) to the negative most position. Slocum gliders have a 0.5 liter BE, giving them ± 250 mL of throw. For the purposes of this study, the BE was always set to -250 mL during **Glide Down** and +250 mL for **Glide Up**. Once a user-defined maximum depth is reached, the glider enters **Inflect Up** and the BE is moved to the **Glide Up** position. Upon reaching the user-defined minimum depth, the glider enters **Inflect Down**, and the BE is moved to the **Glide Down** position. This repeats until the glider reaches the waypoint or the simulation times out. Modes for GPS and communication updates are not included in the state machine as they are not relevant to the study.
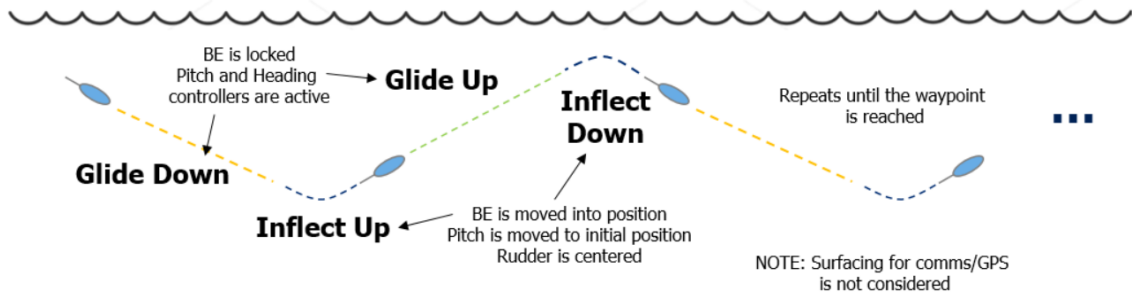
Figure 2-15. Glider State Machine

2.4.1   Coefficient Selection

The hydrodynamic coefficients are selected each iteration based on the AoA and AoS that is calculated from the current glider state. Both angles are rounded to 0.1° precision and a lookup table is used to select the coefficient that corresponds to those angles. The effect of the rudder on the vehicle was added to the simulation by calculating the difference between the coefficient surfaces shown in Appendix C. As the hydrodynamic coefficients were calculated with the rudder set to 20°, the delta between the coefficients was divided by 20 and used along with the simulated rudder angle, AoA, and AoS to derive an additive value for each coefficient. This process is shown graphically in Figures 2-16 and 2-17. The scaling equation shown in Figure 2-17 is based on the rudder characterization curve shown in Figure 2-12 and is:

$$Coefficient\ Scaling\ Value = 0.0221 \times \delta_R^2 - 0.7456 \times \delta_R \qquad (2.47)$$

where δ_R is the rudder angle in degrees.

2.4.2   Navigation Filter

Buoyancy gliders can be outfitted with a variety of sensors in order to estimate their position underwater. At a minimum, gliders use a pressure sensor to derive their depth and depth rate, a tilt sensor to derive their pitch angle, and a magnetometer to derive their heading. Some gliders also use an altimeter for measuring their distance
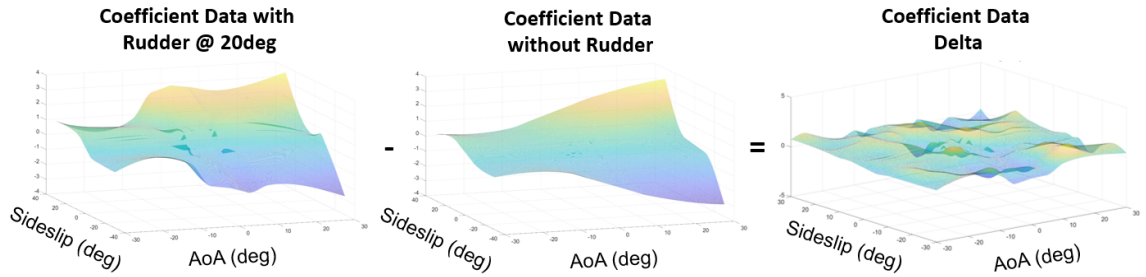
Figure 2-16. Hydrodynamic Coefficient Delta Calculation
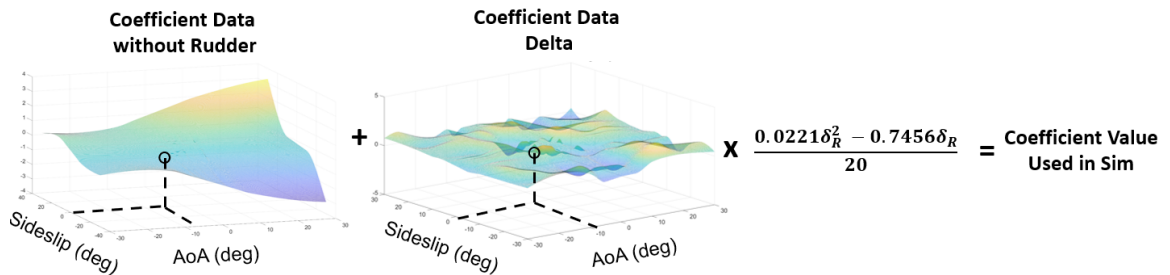
Figure 2-17. Hydrodynamic Coefficient Selection Example

above the sea floor, but this is typically only possible within a few dozen meters of the bottom; however, it can allow the vehicle to better estimate its depth rate and speed over ground. Gliders can also use full 6-DOF inertial measurement units (IMUs) that use an accelerometer, gyroscope and magnetometer in order to estimate the Euler angles and rotational rates of the vehicle. Finally, some recent experiments have outfitted gliders with doppler velocity logs (DVLs) and imaging sonars to aid in velocity estimation [5]. For the purposes of this study, the simulated glider is assumed to have only a depth sensor and IMU.

In order to emulate the dead-reckoning process that real gliders use to estimate their position underwater between GPS updates, the simulated glider uses its simulated sensors to derive its horizontal velocities. Those velocities are then integrated over time to estimate the glider's position. In a real-world system, this can lead to position error growing over time due to the accumulation of small errors in velocity. This

is known as integration drift. As the goal of this study was the development of an improved control system rather than an improved position estimation algorithm, the simulated glider is fed it's "true" position to mitigate any effects on control that the dead-reckoning integration drift may lead to. However, all other estimated states are calculated from the simulated sensors as they would be on a real glider.

The dead-reckoning algorithm starts with the simulated glider's depth rate, which is simply the time derivative of the glider's sensed depth:

$$V_{Depth}[n] = \frac{Depth[n] - Depth[n-1]}{dT} \tag{2.48}$$

where dT is the control update time step. Real-world systems would likely employ a velocity observer or low-pass filter to mitigate the amplification of sensor noise, but for the purposes of this study the simple calculation shown above allows for characterization of the system response without the need for more advanced methods. The depth rate can be used to estimate the magnitude of the total velocity of the glider, V, shown in Figure 2-1:

$$V = \left| \frac{V_{Depth}}{sin(\xi)} \right| \tag{2.49}$$

where ξ is the glide path angle defined by:

$$\xi = \theta - \alpha \tag{2.50}$$

and θ is the sensed pitch of the glider, and α is the AoA of the glider. The AoA is calculated using a lookup table which is derived from the linearized glider dynamics

shown in Section 3.2.1. With the total velocity V of the glider calculated, it is a simple matter to calculate the horizontal velocity of the glider in the world frame:

$$V_H = \sqrt{V^2 - V_{Depth}^2} \tag{2.51}$$

The horizontal velocity can then be separated into its North and East components in order to estimate the glider's position in the world frame:

$$V_N = V_H cos(\psi)$$
$$V_E = V_H sin(\psi) \tag{2.52}$$

where ψ is the measured heading of the vehicle. The glider's position can then be estimated by integrating the velocities with respect to time, like so:

$$N[n] = N[n-1] + V_N dT$$
$$E[n] = E[n-1] + V_E dT \tag{2.53}$$

2.4.3 Simulation Examples

An example simulation using the glider dynamic model is shown in Figure 2-18. The simulation was ran for 2500 seconds and all 12 states are plotted. This particular example uses static hydrodynamic coefficients that are set using the lookup tables described in Section 2.4.1 with an AoA and AoS of 0°. The only exception is the yaw moment coefficient which is set based on the rudder angle, as shown in Figure 2-16. The simulation shows three steady glides segments and three stable inflections. The waypoint goal was 1km North by 1km East, hence the yaw angle of approximately 45°.

Figure 2-19 shows the simulated actuator positions. At each inflection, the buoyancy
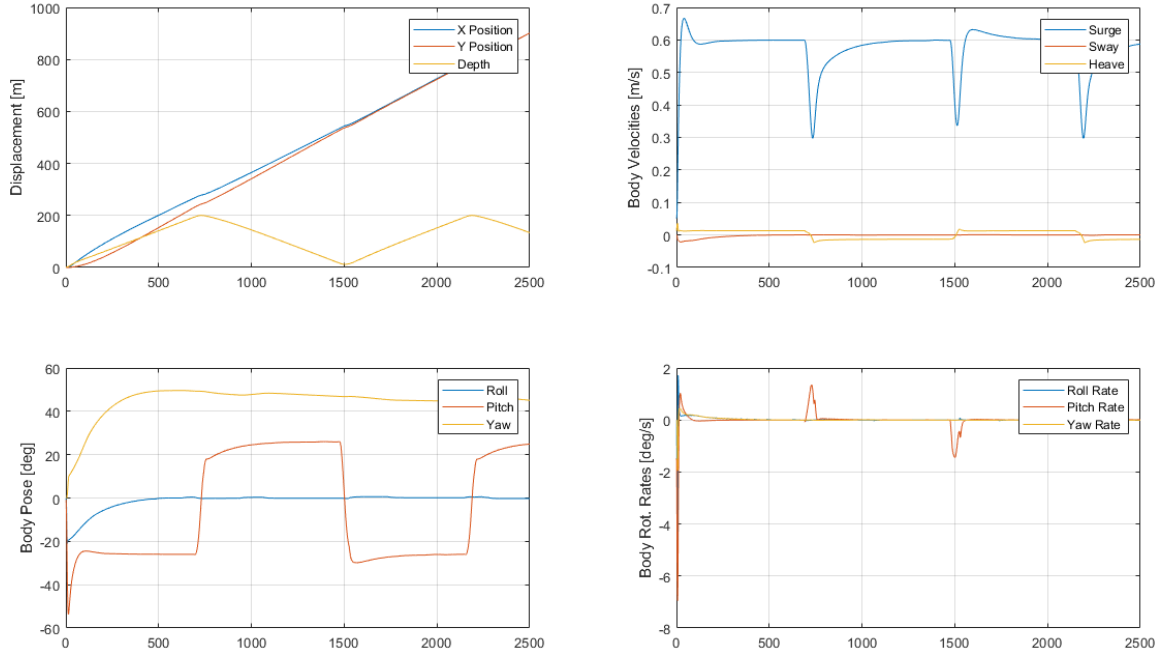
Figure 2-18. Glider Simulation Example

engine is expelled or ingested to inflect up or down, respectively. The internal moving battery mass (referred to as a "pitch vernier" in Slocum documentation) is also shifted to an initial position before the control system takes over during the steady glide phases. The pitch and heading control systems in this example are static gain PI compensators used for demonstrative purposes only. The battery and rudder positions have simulated deadbands of 0.2mm and 1°, respectively. The deadbands are applied to emulate control precision limitations in the real system.

2.5 Environmental Simulation

Simplified ocean current and density models were added to the simulation in order to characterize how the simulated vehicle would respond to environmental disturbances. Currents and density stratification in the ocean can vary widely depending on location and time of year, and the accurate modeling of these phenomena is widely studied in oceanography. For the purposes of this study, representative models were developed
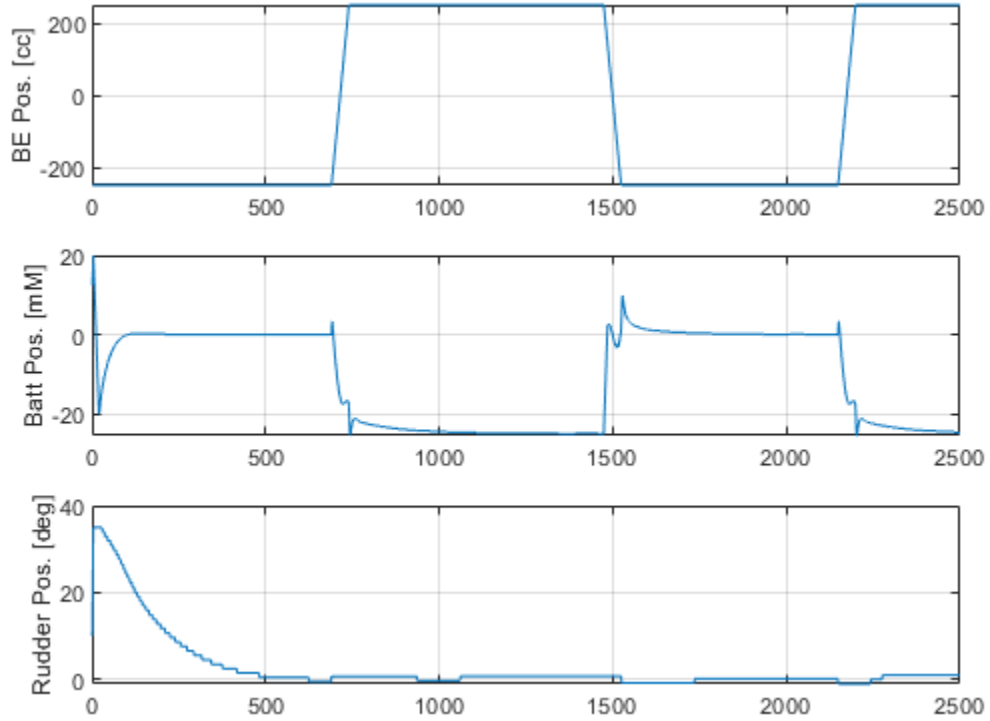
Figure 2-19. Glider Simulation Actuators Example

to stress the control system. Due to the low speed and buoyancy driven nature of the vehicle, it is sensitive to currents and changes in density, and those effects can't be ignored when designing a vehicle controller.

Current Model

Ocean currents are very complex to model. They change in magnitude and direction with depth and vary both temporally and spatially. Upper ocean currents are largely wind driven, while deeper currents are effected more by salinity and temperature differences in the surrounding water [19]. In general though, current magnitudes tend to be strongest at the surface and decrease in intensity as the depth increases.

$$C_{mag}(z) = \frac{C_{max} \times z^{-0.1} + C_{line}(z)}{2} \tag{2.54}$$

Equation 2.54 was used to simulate the notional current magnitude curve shown in

39

Figure 2-20, where z is the depth of the vehicle, and $C_{line}(z)$ is a linearly decreasing value from C_{max} to 0 over the first 200m of depth. C_{max} is taken to be the surface current magnitude. This creates a relatively quick decrease in magnitude in the first 20m of water depth, followed by a linear decrease down to 200m. The direction of the current can also be changed, but for the purposes of this study, only the magnitude was varied with depth.
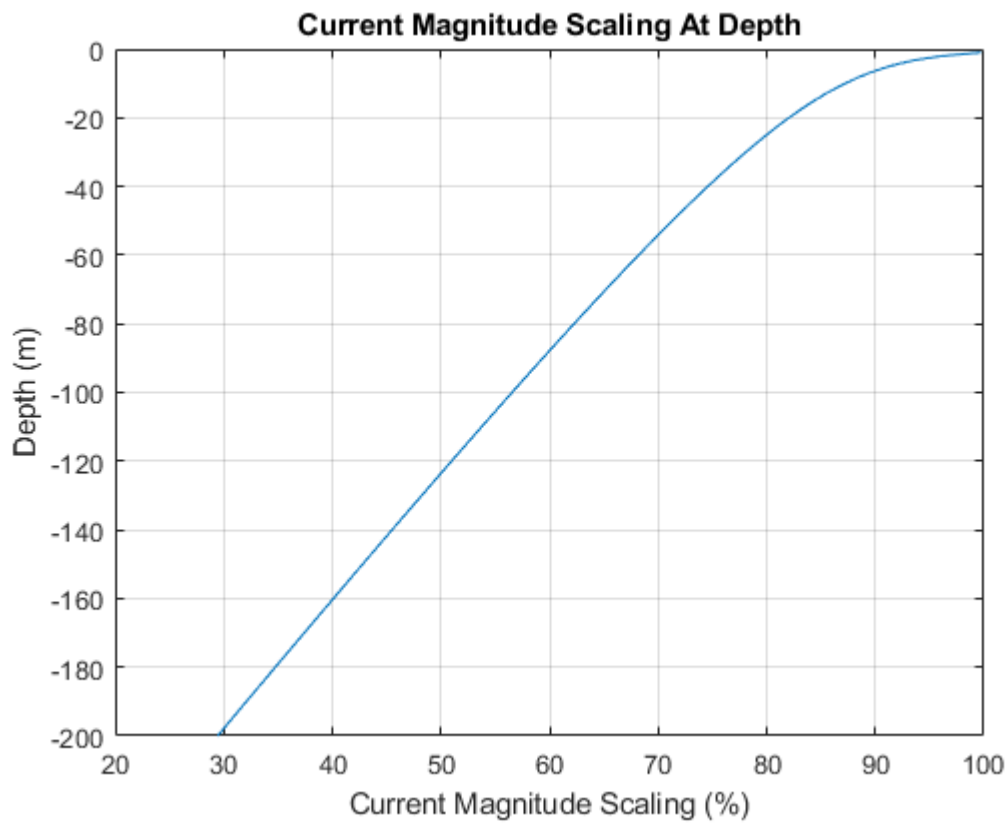
Figure 2-20. Current Magnitude Scaling

Density Model

Much like ocean currents, the density of the ocean is variable both temporally and spatially. Ocean water varies in density due to salinity, temperature and pressure, typically within the range of 1020-1050 kg/m^3, with most of this range being due

to pressure at very deep depths. The density of seawater at the surface is typically within the range of 1020-1029 kg/m^3. The largest vertical density variations happen within the pynocline due to decreasing water temperature and salinity variations in the upper ocean layer [33]. A number of density models exist for different parts of the world's oceans, but most consider much deeper depths than the Slocum glider is capable of reaching.

$$\rho(z) = \frac{\Delta\rho}{1 + e^{0.03819(z-100)}} \tag{2.55}$$

Equation 2.55 describes a sigmoid function that was used to simulate the change in water density in the first 300m of water depth. $\Delta\rho$ is the difference between the surface density at the surface and the maximum density chosen by the user. The so-called "crossover depth" occurs at 100m. This density curve causes the density to increase with depth, which effects the pitch angle and depth rate of the vehicle as it glides downward in the water column.
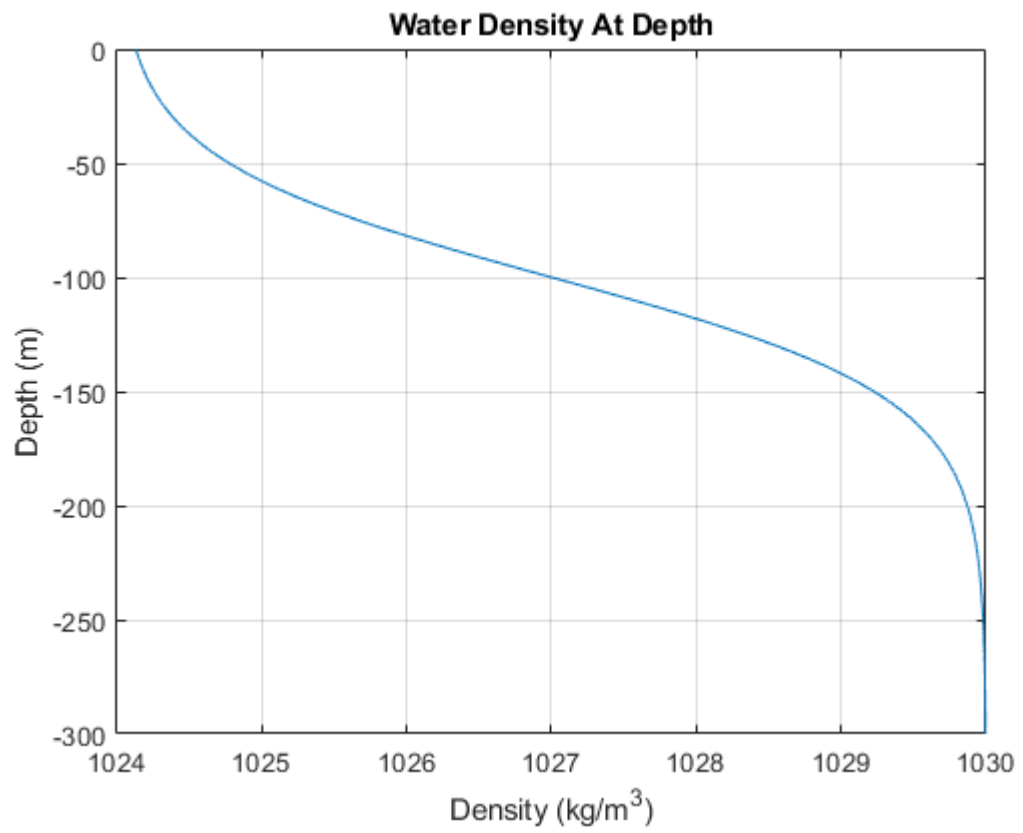
Figure 2-21. Water Density With Depth

Chapter 3

Controller Synthesis

To take advantage of the full capabilities of underwater gliders in ocean sampling and other applications, an accurate and reliable control system is required. Accurate navigation is needed to travel to areas of interest and to correlate sampled data to spatial locations. Robust control is needed for efficient gliding so that gliders can maximize their range or speed. As described in Section 1.3, gliders are usually controlled using fixed-gain PI or PID compensators due to their robustness and ease of implementation. However, due to the nonlinear dynamics of underwater gliders, for higher precision use cases these methods are likely non-optimal, particularly as the glider's performance changes over time. This work aims to develop a systematic design methodology for model-based gain-scheduled feedback control of underwater gliders.

This chapter describes the development of a gain-scheduled PID controller for the simulated underwater glider detailed in Chapter 2. The underlying control architecture that is commonly used in practice for underwater gliders is described first (Section 3.1). One goal of this work is to leverage this "standard" architecture due to its simplicity and utility in real-world applications. To apply linear control methods to the nonlinear dynamics of the system, the glider model was linearized at a wide variety of operating points (Section 3.2), then decoupled transfer functions were derived to describe the

pitch and yaw dynamics of the vehicle (Section 3.3). The transfer functions were then used to determine gain selection equations that could be applied at the linear operating points in order to choose gains that would give the desired response (Section 3.4). The gains were then calculated at a variety of operating points and tabulated for use with the control architecture (Section 3.5). This method allows for gain-scheduled, nonlinear control of underwater gliders, with minimal code changes to fielded systems, while providing significant improvements in control responsiveness.

3.1   Control Architecture

Although a number of control methodologies have been theoretically described for underwater gliders, most are either too computationally expensive (e.g. neural networks, model predictive controllers, adaptive backstepping techniques) or difficult to implement in practice due to limited vehicle state feedback (e.g. LQR, H-infinity) and/or controller specific phenomena such as chattering (e.g. sliding mode control). For these reasons, underwater gliders commonly use PI or PID feedback control to adjust the attitude of the vehicle during the glide phases. During the inflections, open-loop control is often used to adjust the buoyancy of the vehicle, and to move the pitch actuator to an initial position prior to activating feedback control. It is also common to center the rudder during inflections to minimize any undesired yawing that may occur during the transition between glide phases.

There are two main attitude control goals for underwater gliders: the pitch and heading angles. For the shallow water version of the Slocum gliders modeled here, the roll angle is passively stabilized by ballasting the vehicle such that the CG is 4 to 6 cm below the CB [46]. There are other underwater gliders that use a rolling ballast mechanism to control the roll of the vehicle for steering control, but that is not considered in this study. The pitch of the glider is controlled using a moving battery

that translates longitudinally inside the vehicle to shift the CG. The heading of the glider is controlled using the rudder. The pitch and heading control loops are shown in Figures 3-1 and 3-2, respectively.
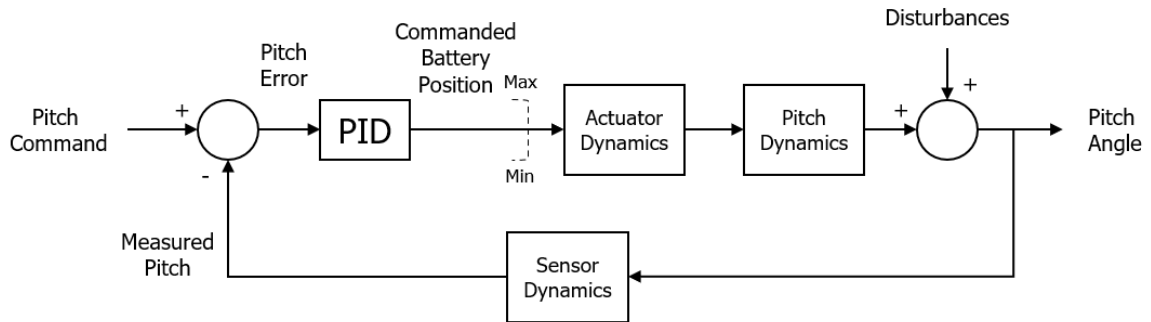
Figure 3-1. Pitch Feedback Control Loop
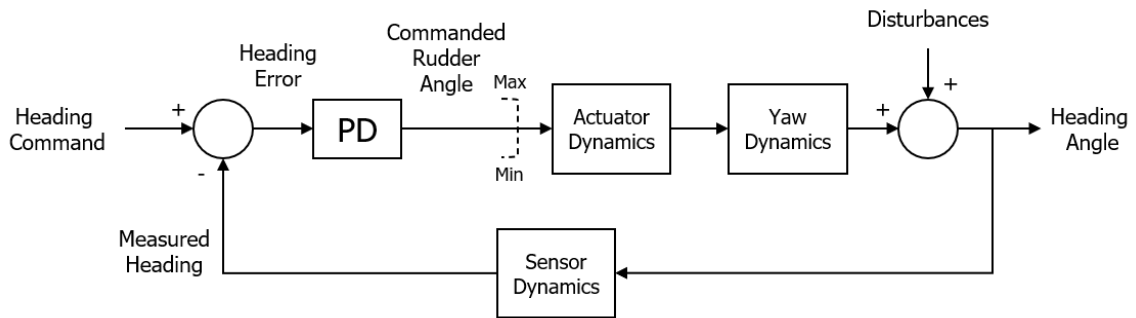
Figure 3-2. Heading Feedback Control Loop

The control loops are nearly identical, with the only differences being the use of a PD controller for the heading control loop, as well as the control signal and actuators being used. As described in Section 2.4.2, the feedback sensor is a 6-DOF IMU that measures the pitch and heading angles of the vehicle using an accelerometer, gyroscope and magnetometer. For the purposes of the simulation, the vehicle state is fed directly into the GNC, and white noise can be added to the state variables to emulate raw sensor measurements. The general PID block is shown in more detail in Figure 3-3. Anti-windup is used in the pitch controller to limit the saturation of the integral term

in the PID [18], but is ignored for controller gain tuning.
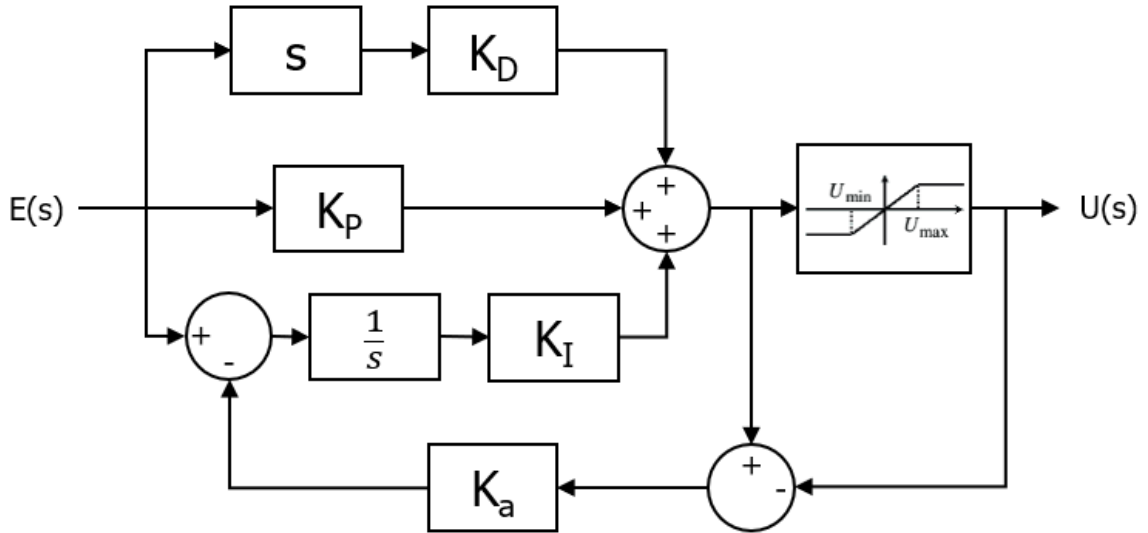
Figure 3-3. PID with Anti-Windup Block Diagram

3.2   Dynamics Model Linearization

In order to apply linear control theory and compensation methods to the nonlinear dynamics of the underwater glider, the nonlinear equations of motion must be linearized about some operating point. For the pitching dynamics, longitudinal models of the glider's dynamics in the vertical plane are provided by [13] and [26]. These models and the glide equilibria calculations described in [34] were used to derive a linearized representation of the longitudinal dynamics of the underwater glider. The turning dynamics of the glider are significantly more challenging. Because the glider must dive and/or rise to propel itself forward, it is impossible to completely decouple the longitudinal and lateral dynamics as is commonly done in aircraft control problems. Due to this inherent complexity, the Nomoto approximation [43] was used along with a simulation approach to build out 2nd order representations of the turning dynamics of the vehicle.

3.2.1 Linearized Pitching Dynamics

As described in [26], the equations of motion in the longitudinal plane for an underwater glider can be summarized as:

$$\dot{x} = u \cos\theta + w \sin\theta \tag{3.1}$$

$$\dot{z} = w \cos\theta - u \sin\theta \tag{3.2}$$

$$\dot{\theta} = q \tag{3.3}$$

$$\dot{q} = \frac{1}{J_2}[(m_3 - m_1 + K_M)uw - m_b r_{b_1} g \cos\theta - \bar{m}g \cos\theta r_{p_1} - \bar{m}g r_{p_3} \sin\theta \\ + K_{M0}u^2 + K_M w^2 q] \tag{3.4}$$

$$\dot{u} = \frac{1}{m_1}[-K_{D0}u^2 + K_{L0}uw - m_b g \sin\theta] \tag{3.5}$$

$$\dot{w} = \frac{1}{m_3}[-K_{L0}u^2 - (K_L + K_{D0})uw + m_b g \cos\theta] \tag{3.6}$$

where x and z are the body-frame positions; θ and q are the pitch angle and pitch rate, respectively; u and w are the body-frame velocities; J_2 is the moment of inertia in the pitch axis; m_1 and m_3 are the added mass parameters in the x and z axes; K_M and K_{M0} are the pitching coefficients; K_D and K_{D0} are the drag coefficients; K_L and K_{L0} are the lift coefficients; m_b is the magnitude of the ballast mass; r_{b_1} is the axial position of the ballast mass in the x axis; $\bar{m}$ is the magnitude of the moving mass; and r_{p_1} and r_{p_3} are the positions of the moving mass in the x and z axes, respectively.

In steady state glides, when the forces acting on the glider are at an equilibrium, many of the variables in the above equations become constant, and it is possible to determine a linear representation for the pitching dynamics of the vehicle. Equation 3.4 is shown below with the linearized parameters denoted with a subscript d:

$$\dot{q} = \frac{1}{J_2}[(m_3 - m_1 + K_M)u_d w_d - m_{b_d} r_{b_1} g \cos \theta_d - \bar{m}g \cos \theta_d r_{p_1} - \bar{m}g r_{p_3} \sin \theta_d$$
$$+ K_{M0} u_d^2 + K_M w_d^2 q]. \tag{3.7}$$

In order to determine the linearized parameters shown in Equation 3.7, we use the glide equilibria calculations described in [34]. We start by prescribing a desired straight line glide path that is specified by a desired glide path angle ξ_d and a desired vehicle speed V_d. Given ξ_d, it is possible to solve for α_d using:

$$\alpha_d = \frac{K_L}{2K_D} \tan \xi_d \left(-1 + \sqrt{1 - 4\frac{K_D}{K_L^2} \cot \xi_d (K_{D0} \cot \xi_d + K_{L0})} \right). \tag{3.8}$$

Subsequently, θ_d can be solved for using:

$$\theta_d = \xi_d + \alpha_d \tag{3.9}$$

and the body velocities along the desired glide path can be solved for using:

$$u_d = V_d \cos \alpha_d \tag{3.10}$$

$$w_d = V_d \sin \alpha_d \tag{3.11}$$

Finally, the ballast mass can be solved for using:

$$m_{b_d} = (m - m_h - \bar{m}) + \frac{V_d^2}{g} \left[-\sin \xi_d (K_{D0} + K_D \alpha_d^2) + \cos \xi_d (K_{L0} + K_L \alpha_d) \right]. \tag{3.12}$$

The remaining terms in Equation 3.7 are either hydrodynamic coefficient constants (K_M and K_{M0}), mass and moment of inertia constants (m_3, m_1, and J_2), or mass position constants (r_{b_1} and r_{p_3}). r_{p_1} is a free variable that is used for controlling the pitch rate.

3.2.2 Linearized Turning Dynamics

As described in [31], the heading control problem for UUVs is usually solved using a Nomoto approximation. Although it was originally derived for the heading control

of ships, it is commonly applied to UUV control due to its simplicity, accuracy, and invariance to vehicle dimensions. Nomoto showed that the steering motions of ships are largely first-order phenomena and can be described using a first-order equation of motion:

$$T\frac{d\dot{\psi}}{dt} + \dot{\psi} = K\delta_r \tag{3.13}$$

where δ_r is the rudder deflection angle, and T and K are known as the Nomoto time constant and gain constant, respectively.

3.3 Transfer Function Derivation

With linearized dynamics in the longitudinal and lateral planes, it is possible to derive transfer functions for the systems that can be used with traditional linear control methods.

3.3.1 Pitch Transfer Function

In order to derive a transfer function for the pitching dynamics of the vehicle, Equations 3.3 and 3.7 are used. We first rearrange and combine terms:

$$\dot{q} = \frac{1}{J_2}[\underbrace{(m_3 - m_1 + K_M)u_d w_d}_{a_1} - \underbrace{m_{b_d}r_{b_1}g\cos\theta_d}_{a_2} - \underbrace{\bar{m}g\cos\theta_d\, r_{p_1}}_{b_1} - \underbrace{\bar{m}gr_{p_3}\sin\theta_d}_{a_3} + \underbrace{K_{M0}u_d^2}_{a_4} + \underbrace{K_M w_d^2}_{a_5}q] \tag{3.14}$$

$$\dot{q} = a_1 - a_2 - a_3 + a_4 + a_5 q - b_1 r_{p_1} \tag{3.15}$$

We then take the Laplace transform:

$$s^2\theta(s) = a_1 - a_2 - a_3 + a_4 + a_5 s\theta(s) - b_1 r_{p_1}(s) \tag{3.16}$$

If we assume that the effects of a_1 through a_4 are small compared to the effects of a_5

and b_1, then we can consider these terms to be a disturbance on the system:

$$s^2\theta(s) = \underbrace{a_1 - a_2 - a_3 + a_4}_{d_\theta(s)} + a_5 s\theta(s) - b_1 r_{p_1}(s) \tag{3.17}$$

$$s^2\theta(s) = d_\theta(s) + a_5 s\theta(s) - b_1 r_{p_1}(s) \tag{3.18}$$

Rearranging, we get:

$$\theta(s) = \frac{-b_1}{s(s - a_5)}\left(r_{p_1}(s) + \frac{1}{b_1}d_\theta(s)\right) \tag{3.19}$$

What arises is a second-order transfer function that relates the axial moving mass position to the pitch angle of the vehicle at the linearized operating point. The disturbance term is entirely comprised of constants and therefore presents a constant offset in the step response that can be compensated for with the integrator term in a PID compensator. This transfer function drastically simplifies the gain tuning procedure for pitch control of an underwater glider.

3.3.2   Pitch Step Response Comparison

To check the validity of the transfer function shown in Equation 3.19, the open-loop step response of the pitching motion of the nonlinear simulation was compared to that of the transfer function. To generate the open-loop step response of the simulated glider, it was controlled to a steady glide and all oscillations were given time to settle out. The moving mass was then shifted forward by 1 mm and the pitch response of the simulated vehicle was logged. The coefficients in the transfer function, b_1 and a_5, were then calculated at a linearized operating point that was similar to that of the simulated glider, and the open-loop step response of the transfer function was calculated in Matlab. The parameters used for the calculations are shown in Table 3-I, and the response comparison is shown in Figure 3-4.

The two responses are similar in nature with a percent difference of 10.5% in the steady-state value that can be explained by the neglected disturbance terms in the
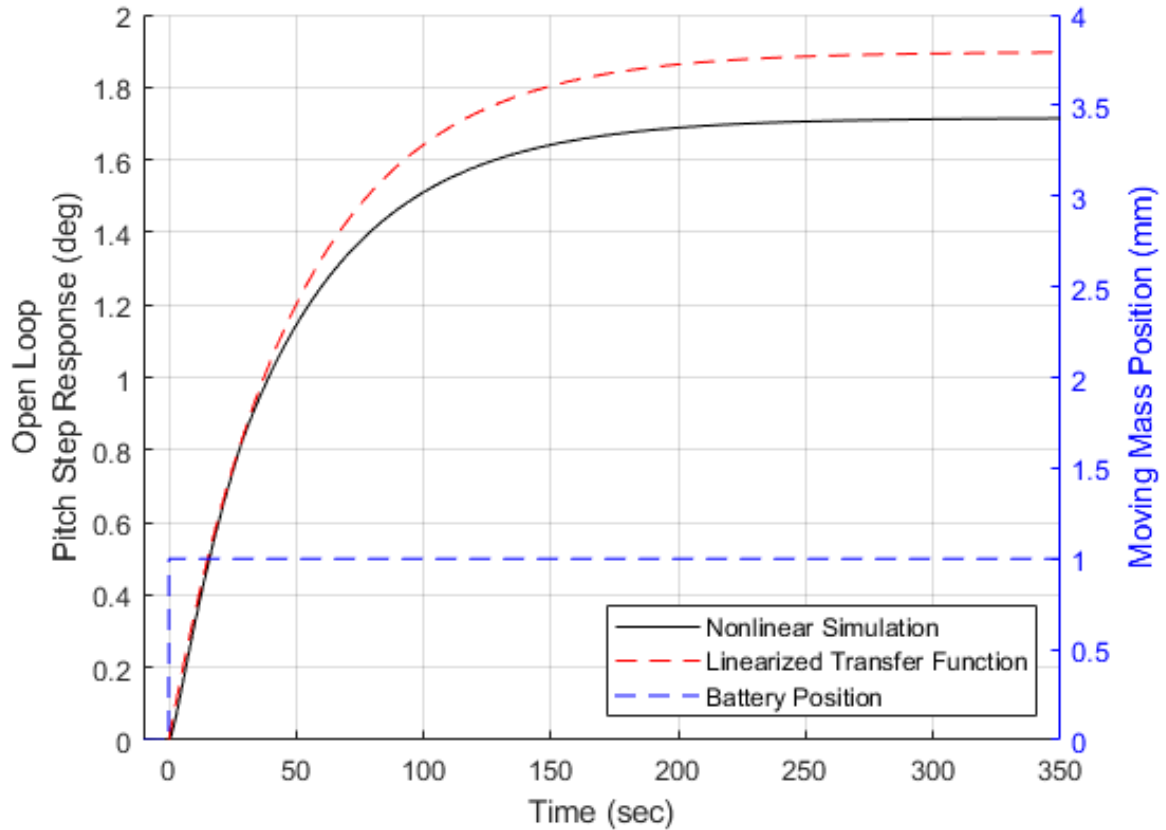
Figure 3-4. Open-Loop Pitch Response Comparison

transfer function. Although this is a fairly substantial deviation, the addition of the integrator term in the controller accounts for it with little trouble. The parameters shown in Table 3-I are the same as those in the numerical simulation; however, the hydrodynamic coefficients are the average of those shown in the tables in Appendix C and have been converted to the appropriate units for the transfer function calculations. One final point to note is the non-zero value for K_{L0}. As Graver describes in [34], "For a vehicle which is symmetric about the body [x-y] plane, $K_{L0} = 0$." As the Slocum glider that is being modeled here is not symmetric about the x-y plane, a notional lift coefficient was chosen to indicate the lift differential across the body with no angle-of-attack.

Despite the deviation in the steady-state value, the nonlinear numerical simulation and linear transfer function show good fidelity in their time response characteristics,

Table 3-I. Simulation Parameters

Parameter	Value
V_d (m/s)	0.3
ξ_d (deg)	30
$\bar{m}$ (kg)	9.1
J_2 $(kg \cdot m^2)$	130
K_M $(N \cdot m(\frac{s}{m})^2)$	-428.21
K_{D0} $(N(\frac{s}{m})^2)$	0
K_D $(N(\frac{s}{m})^2)$	37.47
K_{L0} $(N(\frac{s}{m})^2)$	10
K_L $(N(\frac{s}{m})^2)$	55.09

indicating that the transfer function can be used to tune gains for the pitch control of the simulated glider.

3.3.3 Heading Transfer Function

The heading transfer function can be derived directly from Equation 3.13 by taking the Laplace transform and rearranging:

$$Ts^2\psi(s) + s\psi(s) = K\delta_r(s) \tag{3.20}$$

$$\psi(s) = \frac{K}{s(Ts+1)}\delta_r(s) \tag{3.21}$$

What arises is a second-order transfer function that relates the rudder deflection angle to the heading angle of the vehicle.

3.4 Gain Selection Methodology

With transfer functions that describe the pitching and steering dynamics of the vehicle, it is possible to derive gain selection equations that allow us to calculate gains that give a desired response. This section outlines the derivation of the gain selection equations for the pitch and heading controllers, as well as the methodology used to

generate the gain tables used for the gain-scheduled controller.

3.4.1 Pitch Gain Selection Equations

Using Equation 3.19 and the control architecture shown in Figure 3-1, a closed-loop transfer function can be calculated. For the purposes of deriving gain selection equations, the disturbance term in Equation 3.19 is neglected. The actuator and sensor dynamics in Figure 3-1 are neglected as well, as are the nonlinear control elements such as rate and position limits. Additionally, a PD compensator is used rather than a PID compensator. The integral term is added later to account for the disturbances. Figure 3-5 shows the simplified pitch control topology used for gain selection calculations.
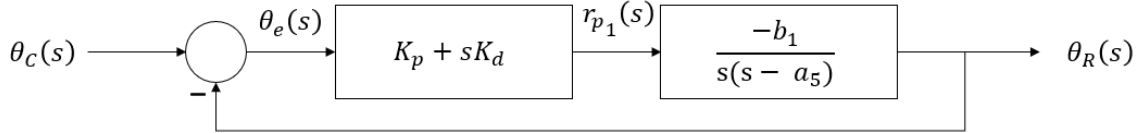
Figure 3-5. Pitch Control Block Diagram

The closed-loop transfer function is then:

$$\frac{\theta_R(s)}{\theta_C(s)} = \frac{-b_1 K_d s - b_1 K_p}{s^2 - (a_5 + b_1 K_d)s - b_1 K_p} \tag{3.22}$$

We see that the closed-loop transfer function takes the form of a second-order system with a zero, which has the canonical form:

$$H(s) = \frac{\frac{\omega_n^2}{z_1}(s + z_1)}{s^2 + 2\zeta\omega_n s + \omega_n^2} \tag{3.23}$$

where ζ is the damping coefficient, ω_n is the natural frequency of the system, and z_1 is the location of the zero. Setting Equations 3.22 and 3.23 equal to each other gives

53

relationships between the gains K_p and K_d and the design parameters ζ and ω_n:

$$\omega_n^2 = -b_1 K_p \tag{3.24}$$

$$\omega_n = \sqrt{-b_1 K_p} \tag{3.25}$$

$$\zeta = -\frac{a_5 + b_1 K_d}{2\sqrt{-b_1 K_p}} \tag{3.26}$$

By selecting values for ζ and ω_n, it becomes possible to solve for the values of K_p and K_d that give the desired response.

3.4.2   Heading Gain Selection Equations

Following a similar process as the one described in Section 3.4.1, we use Equation 3.21 and the control architecture shown in Figure 3-2 to derive a closed-loop transfer function. In a similar manner, the actuator and sensor dynamics are neglected, as are the nonlinear control elements. A PD compensator is used; however, there is no need for an integral term to be added in this case. Figure 3-6 shows the simplified heading control topology used for gain selection calculations.
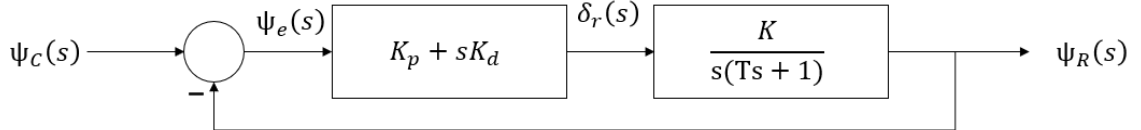
Figure 3-6. Heading Control Block Diagram

The closed-loop transfer function is then:

$$\frac{\psi_R(s)}{\psi_C(s)} = \frac{K K_d \left(s + \frac{K_p}{K_d}\right)}{s^2 + \left(\frac{K K_d + 1}{T}\right) s + \frac{K K_p}{T}} \tag{3.27}$$

We again see that the closed-loop transfer function takes the form of a second-order

system with a zero. Setting Equations 3.27 and 3.23 equal to each other gives:

$$\omega_n^2 = \frac{KK_p}{T} \tag{3.28}$$

$$\omega_n = \sqrt{\frac{KK_p}{T}} \tag{3.29}$$

$$\zeta = \frac{KK_d + 1}{2T\sqrt{\frac{KK_p}{T}}} \tag{3.30}$$

3.5 Deriving the Gain Tables

With transfer functions and gain selection equations in hand, all that is left is the determination of the transfer function coefficients at the desired operating points, and the calculation of the gains at those operating points.

3.5.1 Pitch Gains

To generate gains for the pitch controller, a variety of steady state glides were defined by specifying the desired glide path angle ξ_d and the desired vehicle speed V_d, as described in Section 3.2.1. The chosen parameters were:

- Glide Speed (m/s): 0.1, 0.2, 0.3, 0.4, 0.5

- Glide Path Angle (deg): -45,-40,-35,-30,-25,-20,-15,-10,10,15,20,25,30,35,40,45

A Matlab script was developed that steps through each permutation of the chosen glide speed and glide path angles and calculates the b_1 and a_5 coefficients in Equations 3.25 and 3.26. Values for ζ and ω_n were selected, and K_p and K_d were solved for using Matlab's system of equations solver. A sensitivity study was performed to assess which values of ζ, ω_n and K_i would provide the best results. The results of the sensitivity study are shown in Section 4.1.1. The final values used were: $\zeta = 1.5$ and $\omega_n = 0.75$. K_i was chosen to be $K_p/20$ at each operating point.

To generate gain lookup tables, the calculated gains were interpolated using the Akima method in a process similar to the one used for the hydrodynamic coefficients. The glide speed and glide angle axes were interpolated to 0.01 m/s and 0.1°, respectively. The gain curves are shown in Appendix D.

3.5.2   Heading Gains

In order to determine the Nomoto time and gain constants described in Equation 3.13, the "truth" simulation of the glider was used. The time constant was found by commanding the simulated glider to a steady dive (defined by a depth rate and pitch angle) then deflecting the rudder to some angle and measuring the response time of the vehicle's yaw rate. This was done at several combinations of depth rates, pitch angles and rudder deflection angles, and the value was found to be very similar in all cases. The time constant of a first order system is where the magnitude of the response is at 63% of the steady state value. For the simulated glider, this value came out to be approximately 58 seconds.

All that was left was to determine the Nomoto gain constants for a variety of steady state glides. To do this, the simulated glider was controlled to a set of commanded depth rates and pitch angles using static gain controllers. The glider was given time to stabilize in the glide and reach a true steady state, then the rudder was deflected to some angle. The simulated glider would start to spiral and the yaw rate of the vehicle would reach a steady state value. This yaw rate value was averaged over a 500 second period and tabulated with respect to the depth rate, pitch angle, and rudder deflection that caused it. The chosen values were:

- Depth Rate (m/s): -0.35, -0.25, -0.15, 0.15, 0.25, 0.35
- Pitch Angle (deg): -35,-30,-25,-20,-15,-10,10,15,20,25,30,35
- Rudder Deflection (deg): -45,-30,-15,-10,-5,5,10,15,30,45

Observing the form of Equation 3.21, we note that the Nomoto gain constant is multiplied by the rudder deflection angle. So, to find the Nomoto gain constant from the averaged yaw rates, the yaw rates were divided by the rudder deflection angles that caused them. They were then averaged across all rudder angles to create a table of Nomoto gain constants defined only by the depth rate and pitch angle. This process is shown graphically in Figure 3-7 below. Note that during downward glides, the depth rate is positive and the pitch angles are negative; and inversely, during upward glides, the depth rate is negative and the pitch angles are positive. Pitch angle and depth rate combinations that would have caused unstable glide conditions were neglected.
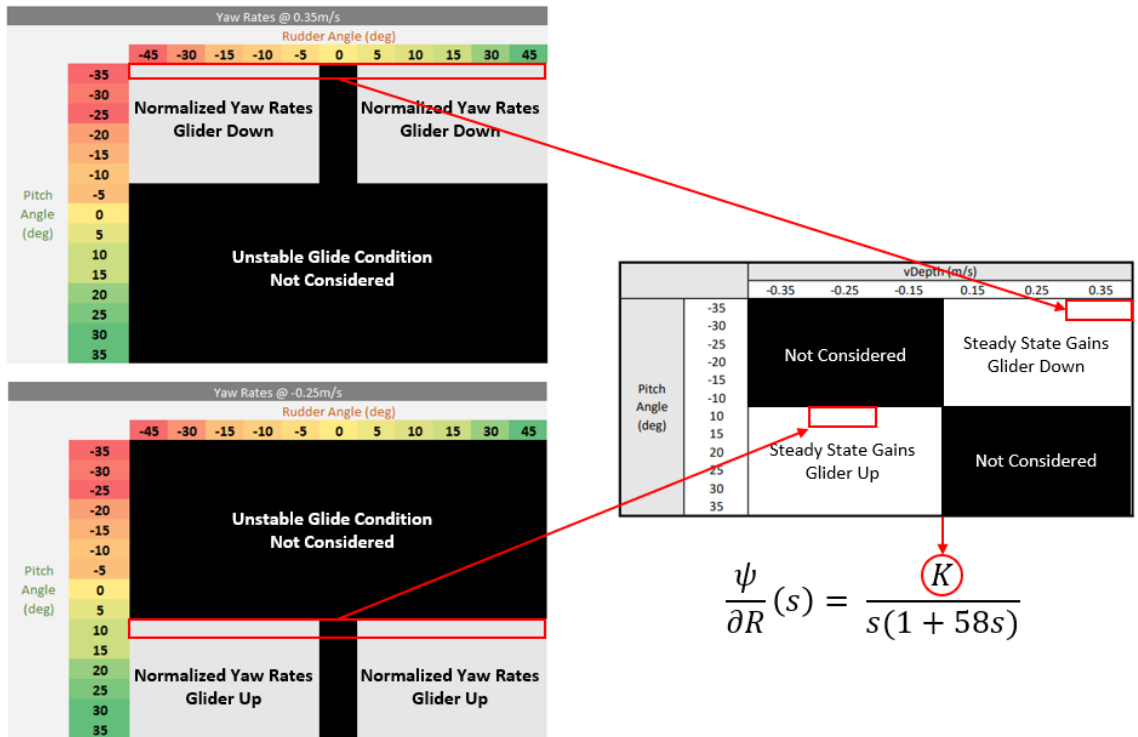
Figure 3-7. Nomoto Gain Tabulation Process

With the Nomoto time and gain constants defined at the operating points, a similar process as the one described in Section 3.4.1 was followed to determine the heading controller gains. A Matlab script was developed that stepped through the tabulated Nomoto gain constants and, using selected ζ and ω_n values, K_p and K_d were solved

for using Equations 3.29 - 3.30 and Matlab's system of equations solver. Another sensitivity study was performed to assess which values of ζ and ω_n should be used. The results of the sensitivity study are shown in Section 4.1.2. The final values used were: $\zeta = 0.5$ and $\omega_n = 0.015$. No K_i gain was needed for the heading controller as the transfer function fully described the turning dynamics of the vehicle.

Finally, the gain lookup tables were generated using the Akima method. The depth rate and pitch angle axes were interpolated to 0.01 m/s and 0.1°, respectively. The gain curves are shown in Appendix D. Note that the gains change sign depending on whether the vehicle is gliding up or down. This is due to the negative roll-yaw coupling acting on the glider during upward glides, which requires the rudder to rotate in the opposite direction between downward and upward glides in order to turn in the same direction.

Chapter 4

Results and Analysis

This chapter contains simulation results and comparative analysis between a static gain controller and the gain-scheduled controller described in the previous sections. We start by performing a sensitivity study to determine ζ and ω_n values for the gain selection equations described in Section 3.4, as well as the integrator gain values needed for the pitch controller (Section 4.1). We then compare various metrics that speak to the performance improvements that the gain-scheduling controller gives over a static gain controller (Section 4.2). We also assess the robustness of the gain-scheduled controller to various plant and environmental disturbances (Section 4.3). And finally, we characterize the power efficiency improvements gained through the use of gain-scheduling (Section 4.4).

4.1 Sensitivity Study

To determine the ζ and ω_n values for tuning the pitch and heading controller gains, Matlab scripts were developed that would sweep through a variety of combinations of ζ and ω_n values, solve for the K_p and K_d gains, and then plot the step responses of the closed loop systems.

4.1.1 Pitch Controller

A selection of closed loop pitch step responses are shown in Figure 4-1. All of the step responses shown have a K_i value that is equal to $K_p/20$. This is described in more detail in the following section. Due to the zero in the closed loop transfer function (Equation 3.22), the system responds differently than a canonical 2nd order system. Traditionally, a 2nd order system with a ζ of 1 should give a critically damped response, but for the 2nd order system with a zero, it gives roughly 15% of overshoot. Increasing ζ lessens the overshoot, but causes the settling time to increase. Increasing ω_n causes the rise time to decrease without increasing the overshoot.
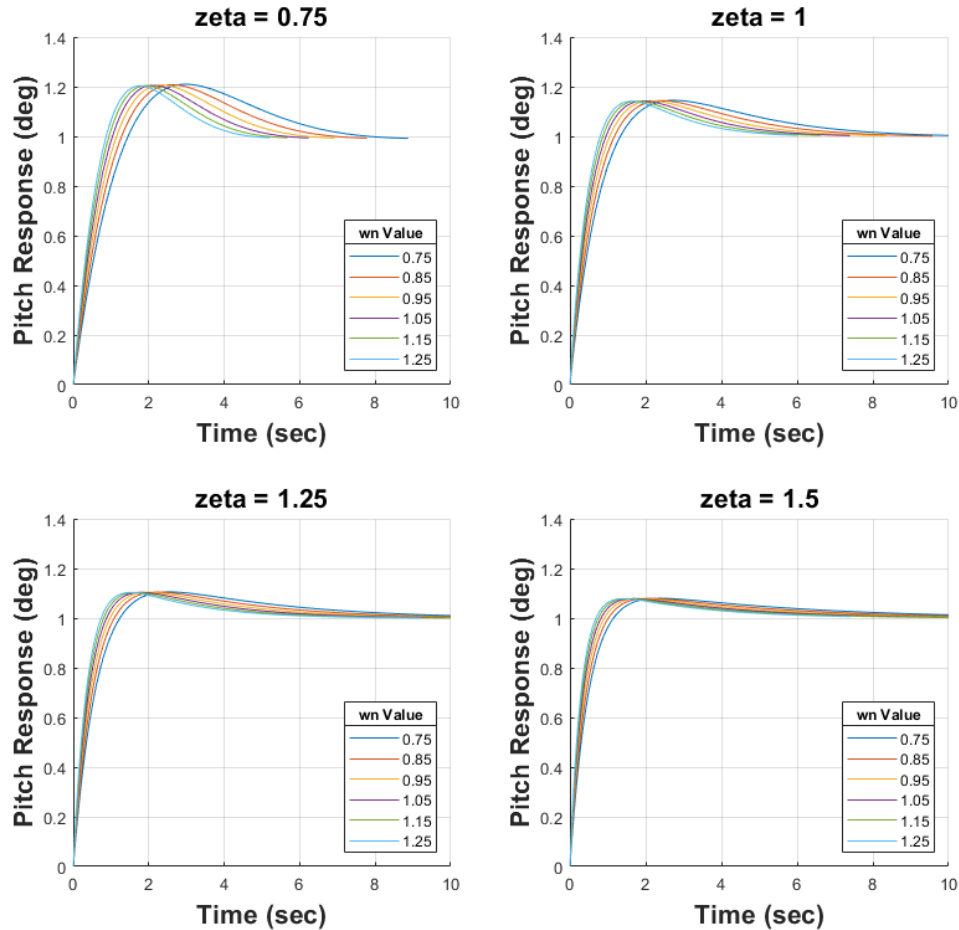
Figure 4-1. Pitch Controller Sensitivity Study

A number of considerations were made before selecting the final ζ and ω_n values.

Beyond simply improving the responsiveness of the pitch controller, one of the primary concerns was power efficiency. Through simulated trials, it was found that a ζ of 1.5, and an ω_n of 0.75, gave improved pitch control while minimizing actuator motion, and therefore power expenditure. This is discussed in more detail in Section 4.4. Another concern was sensitivity to sensor noise. Although higher ζ values led to higher K_d values, thereby increasing the controller's noise sensitivity, the increase was minimal and was shown to be mitigable through the addition of a low-pass filter. This is discussed in more detail in Section 4.3.2.

Selecting K_i
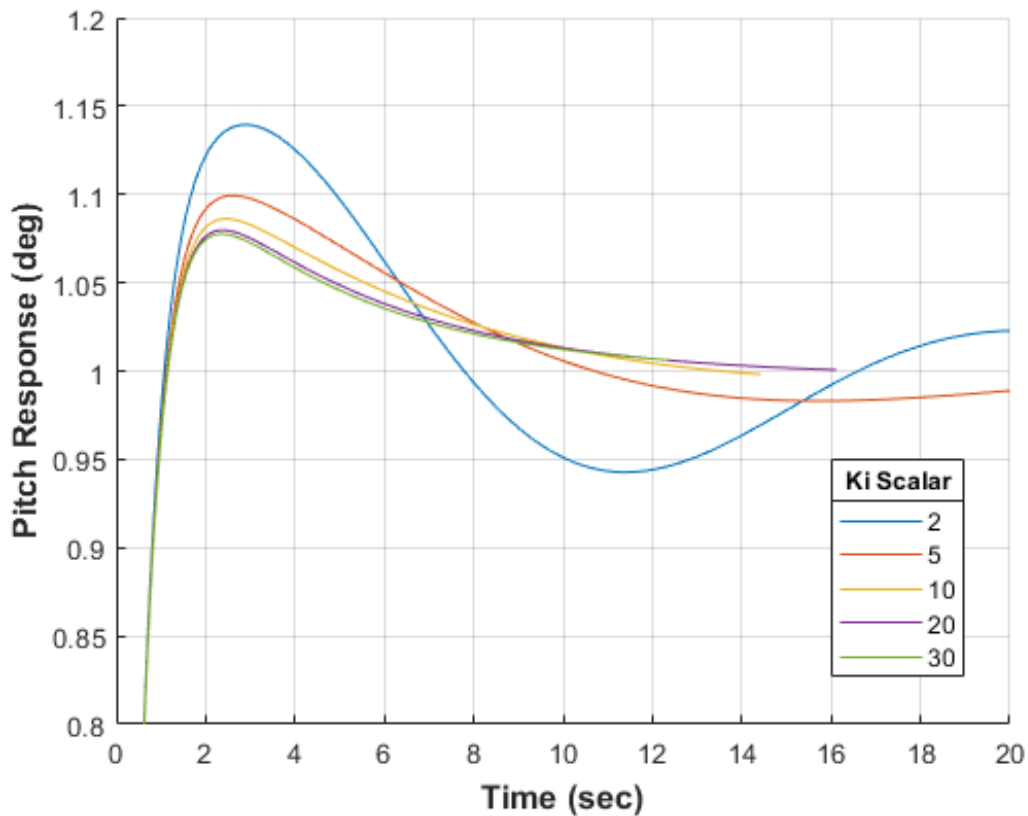
Figure 4-2. Pitch Controller K_i Value Selection

Another consideration for the pitch controller was the selection of the integrator gains. As described in Section 3.3.2, when comparing the derived transfer function

61

and nonlinear simulation (Figure 3-4), there is a difference in the steady-state value that is a result of the neglected disturbance terms. If a PD compensator is used for pitch control, rather than a PID compensator, the pitch controller does not achieve a steady-state error of 0. This is shown in Figure 4-3, where the solid orange line is the response given a PD compensator. To assess what values of Ki should be used, both the closed loop transfer function and nonlinear simulation were used.
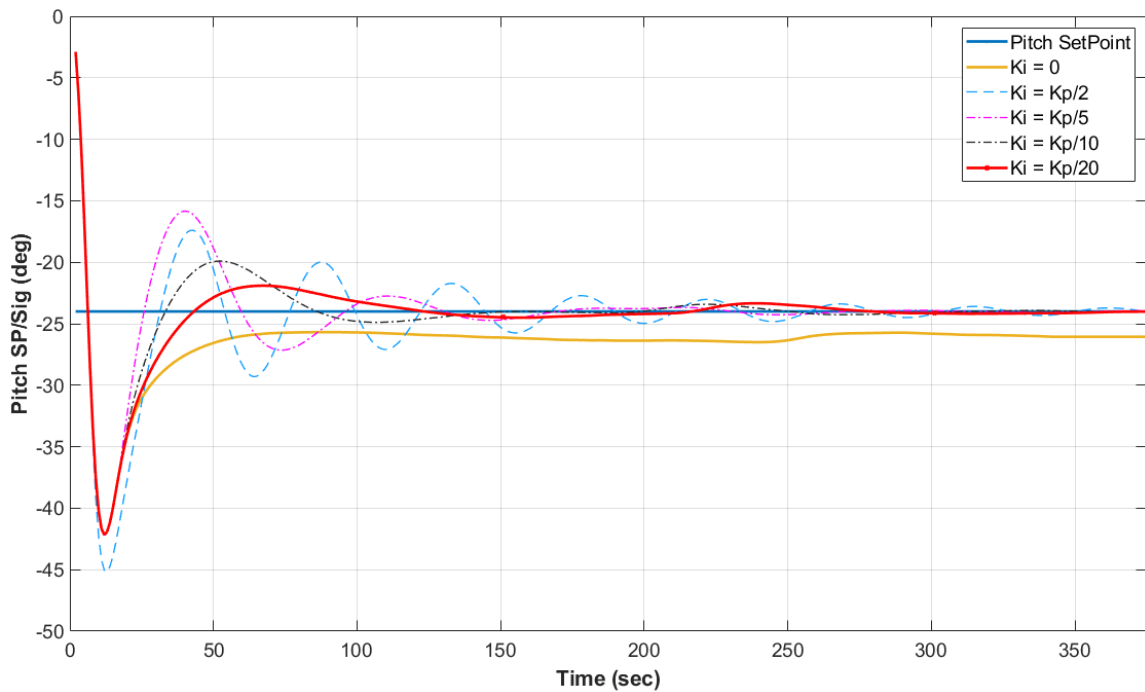
Figure 4-3. Pitch Controller K_i Sim Response Comparison

The step responses of the closed loop pitch transfer function are shown in Figure 4-2 with varying K_i values. The K_i values were defined as the calculated K_p gains divided by some scalar value (shown in the legend). As the K_i values decreased, the ringing in the response and the settling time both decreased as well, with minimal changes in the response beyond a scalar value of 20. Applying this to the nonlinear simulation, we get the responses shown in Figure 4-3. This simulation shows the vehicle being commanded to glide downward at a pitch angle of -24°. Due to the starting condition of the glider, all of the simulated responses initially overshoot the set point; however,

there is significant ringing for the scalar values 2 and 5. For $K_i = K_p/10$, there is reduced ringing, but significant overshoot of about 4° (or 16% of the set point). For $K_i = K_p/20$, there is reduced overshoot and a smooth transition into a steady glide. For this reason, K_i was chosen to be $K_p/20$.

4.1.2   Heading Controller

A selection of closed loop heading step responses are shown in Figure 4-4. Similar to the pitch transfer function, the zero in Equation 3.27 results in the system responding differently than a canonical 2nd order system. An increasing ζ causes more damping, but even with a ζ of 1, the system is not critically damped. Increasing ω_n decreases the rise time and slightly increases the overshoot.
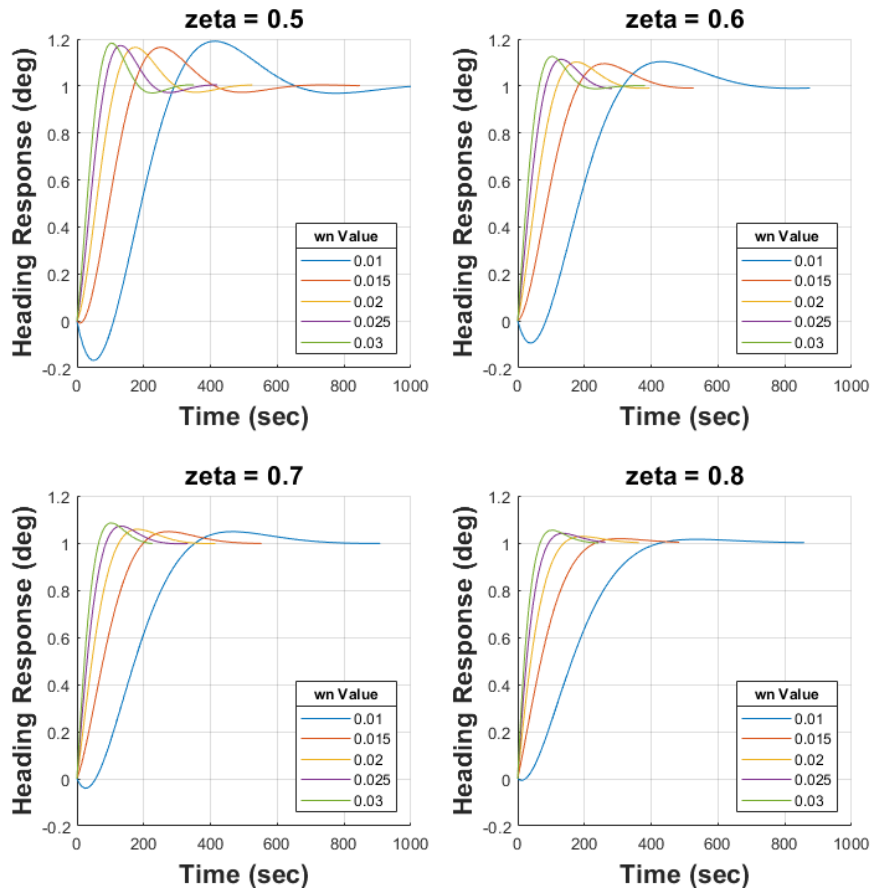
Figure 4-4. Heading Controller Sensitivity Study

Again, a number of considerations were made before selecting the final ζ and ω_n values. Similar to the pitch controller, minimizing actuator motion and reducing sensitivity to sensor noise were the main factors beyond improving responsiveness. Through simulated trials it was found that a ζ of 0.5 and an ω_n of 0.015 gave improved heading control without drastically increasing rudder motion and noise sensitivity. These considerations are discussed further in Sections 4.4 and 4.3.2.

4.2   Controller Performance Comparison

There are a number of metrics that can be used to compare the performance of a traditional static-gain controller versus the gain-scheduled controller. From a performance perspective, the main concerns are the time response characteristics of the controllers, as well as any control improvements that can be realized. This section compares two sets of gains used with the static-gain pitch and heading controllers to the gain-scheduled control scheme described in the previous sections. The first set of gains was hand-tuned by the author to give a robust response within reasonable time margins. The second set of gains was calculated using the Ziegler-Nichols method [7]. The static gain values are shown in Tables 4-I and 4-II. The scheduled gains were calculated using the ζ and ω_n values discussed in Section 4.1.

Table 4-I. Static Gain Values for the Pitch Controller

Gain	Hand-Tuned	Ziegler-Nichols
K_p	-1	-0.033
K_i	-0.01	-0.0027
K_d	-0.5	-0.2658

Table 4-II. Static Gain Values for the Heading Controller

Gain	Hand-Tuned	Ziegler-Nichols
K_p	1	1.2454
K_i	0.001	0.0095
K_d	3	110.7546

4.2.1 General Comparisons

Figure 4-5 shows the pitch response of the vehicle as it transitioned through multiple inflections, while Figure 4-6 shows the heading response. The solid orange lines are the results using the hand-tuned gains. The dashed black lines are the results using the Ziegler-Nichols (Z-N) gains. And the dash-dot red lines are the results using the scheduled gains. The pitch set points were set to $\pm 26°$ and are shown as different color "○", "*", and "◇" markers. Multiple sets of pitch set points are plotted because the simulated glider transitioned between glide directions at different times due to the differing pitch angles, and the set point lines show when those transitions took place.
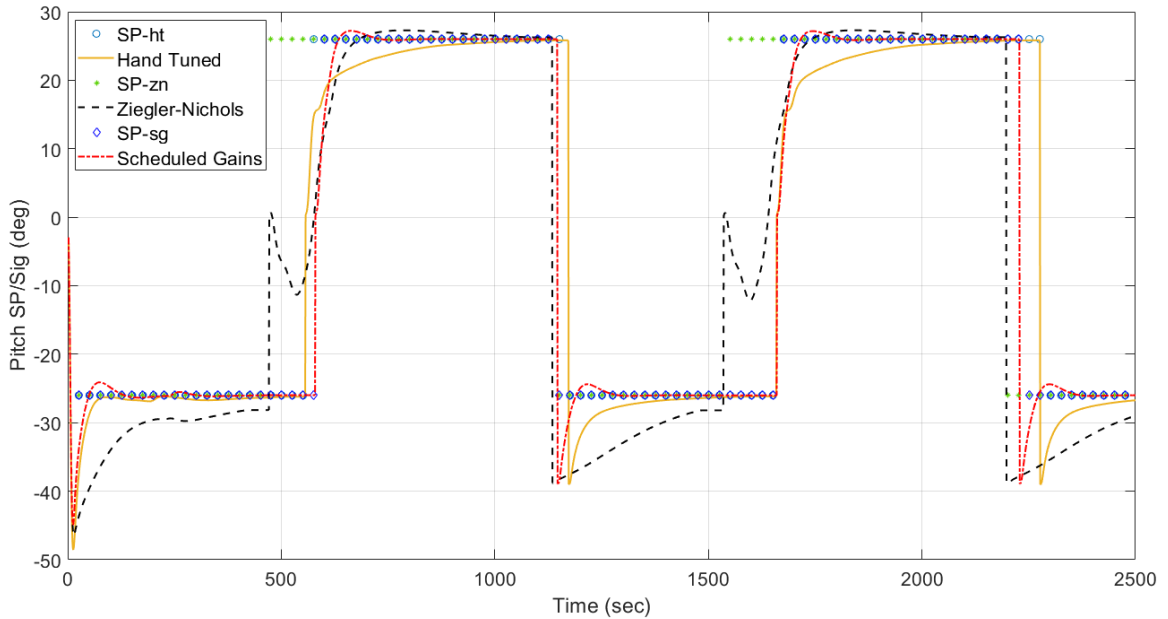
Figure 4-5. Pitch Controller Comparison - Multiple Inflections

For these simulations, the moving battery mass was moved to +10mm and -10mm for

the downward and upward inflections, respectively. This battery motion takes place while the buoyancy engine is ingesting or expelling, which can cause some interesting behavior. Note how the pitch angle initially goes negative when using the Z-N gains. This is due to the initial battery position (-10mm) being too far forward when entering the upward glide. The Z-N gains are less aggressive than the hand-tuned gains and cannot compensate fast enough, which causes the vehicle's nose to dip before the battery shifts back. By comparison, the hand-tuned and gain-scheduled gains handle the transition more gracefully.
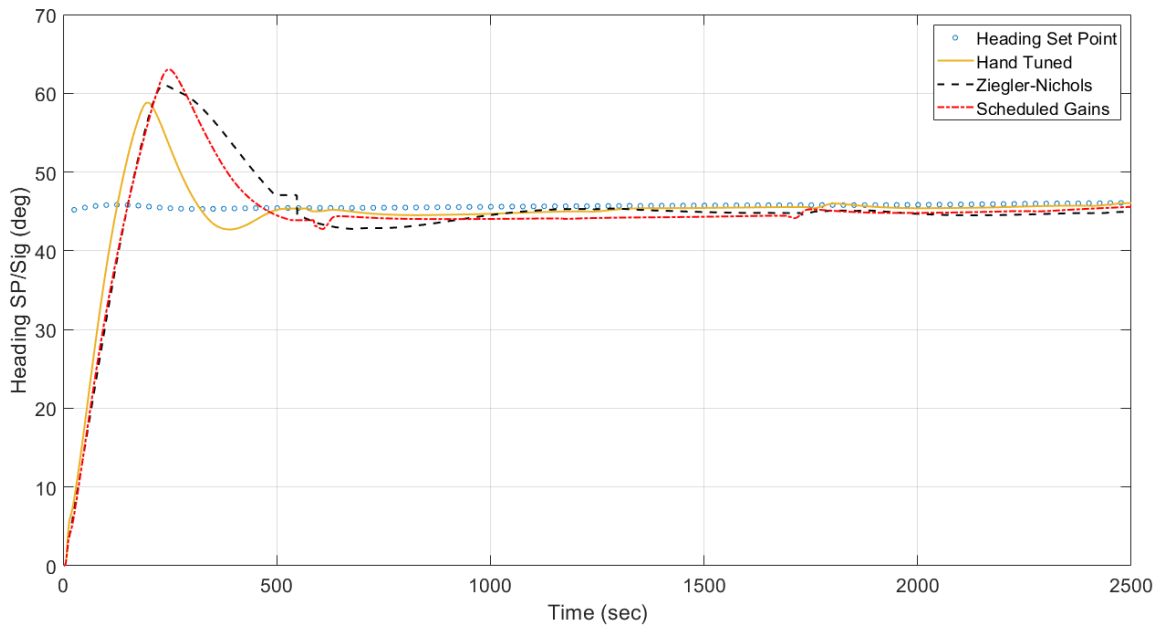
Figure 4-6. Heading Controller Comparison - Multiple Inflections

The response of the heading controller is very similar for these three sets of gains. Although the static gain examples exhibit some ringing about the set point, the overshoot and response times for the three controllers are very similar.

We can further improve the control of the vehicle by selecting different ζ and ω_n values when deriving the scheduled gain tables. Figures 4-7 and 4-8 compare the pitch

and heading responses of the hand-tuned static gains in Tables 4-I and 4-II to the gain-scheduled controller when using the ζ and ω_n values shown in Table 4-III. Note the reduction in overshoot and response time when using these values. The drawback of this improved control is a significant increase in actuator usage, which implies a higher power draw for control of the vehicle.

Table 4-III. ζ and ω_n Values for Improved Control

Parameter	Pitch Controller	Heading Controller
ζ	2	0.4
ω_n	1.25	0.015
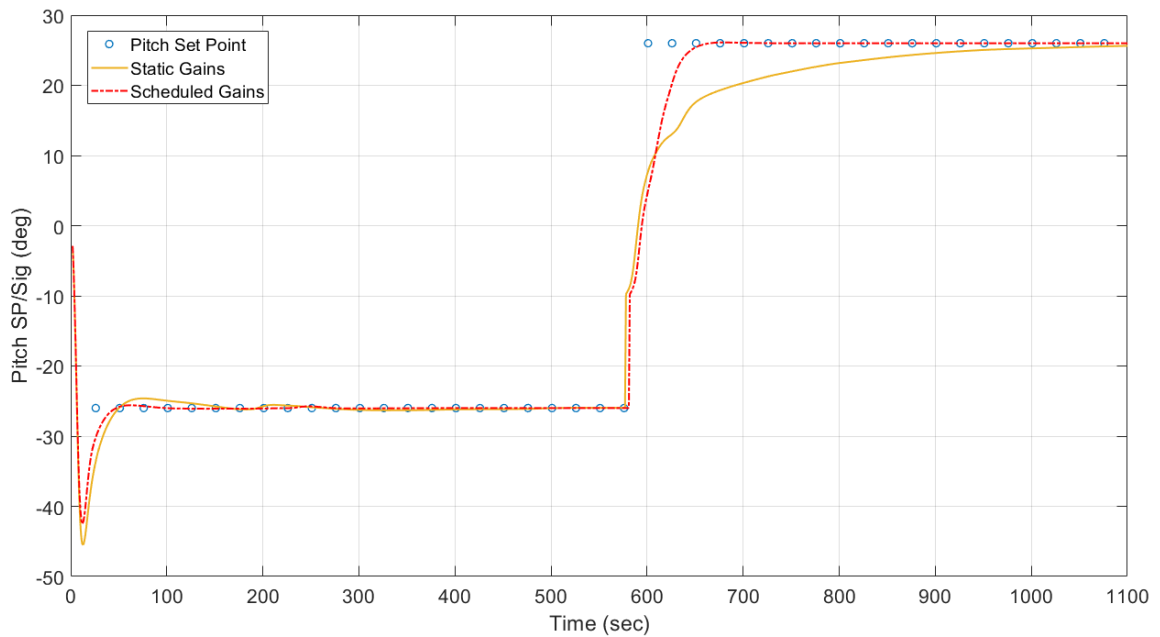
Figure 4-7. Pitch Controller Comparison - Improved

4.2.2 Speed Over Ground

Another important metric to consider is the vehicle's speed over ground. Underwater glider's move at a relatively low speed and are therefore more susceptible to ocean currents than typical UUVs. Figure 4-9 shows the horizontal and vertical velocities
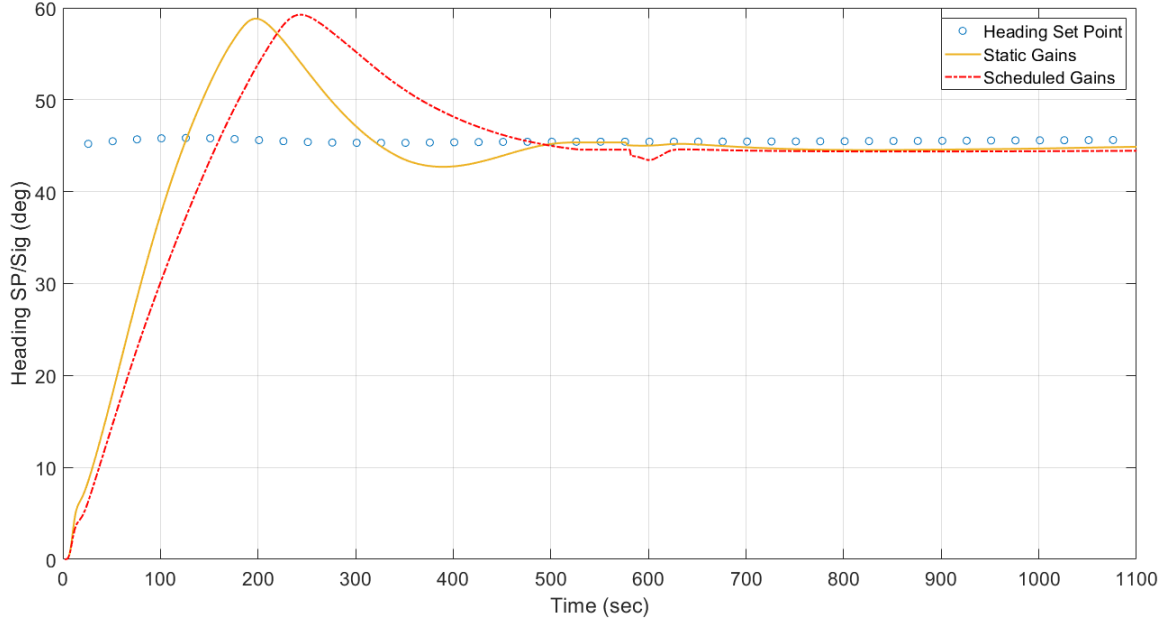
Figure 4-8. Heading Controller Comparison - Improved

of the simulated vehicle for the runs shown in Figures 4-5 and 4-6. Because of the increased responsiveness of the vehicle when using the gain-scheduled controller, the horizontal velocity is more stable during the glide phases. The increased pitch over/under shoot caused by the static gain controller sometimes causes the vehicle to move through the water at a higher velocity, but this can have adverse effects on the power consumption of the vehicle due to the increased pumping that would be needed as the glider reaches its maximum depth more quickly.

4.2.3 Control Through Inflections

Generally, the pitch and heading angles of gliders are only actively controlled during glide phases. This is due to the sensitivity of the glider to variations in buoyancy and CG location during inflections. Without careful consideration for the rate of buoyancy change and ballast weight movement, static gain controllers can struggle to control the vehicle through inflections. Improvements to the pitch control through inflections was investigated in simulation using the gains shown in Tables 4-I and 4-II and the gain-scheduled controller derived from the ζ and ω_n values described in Section 4.1.
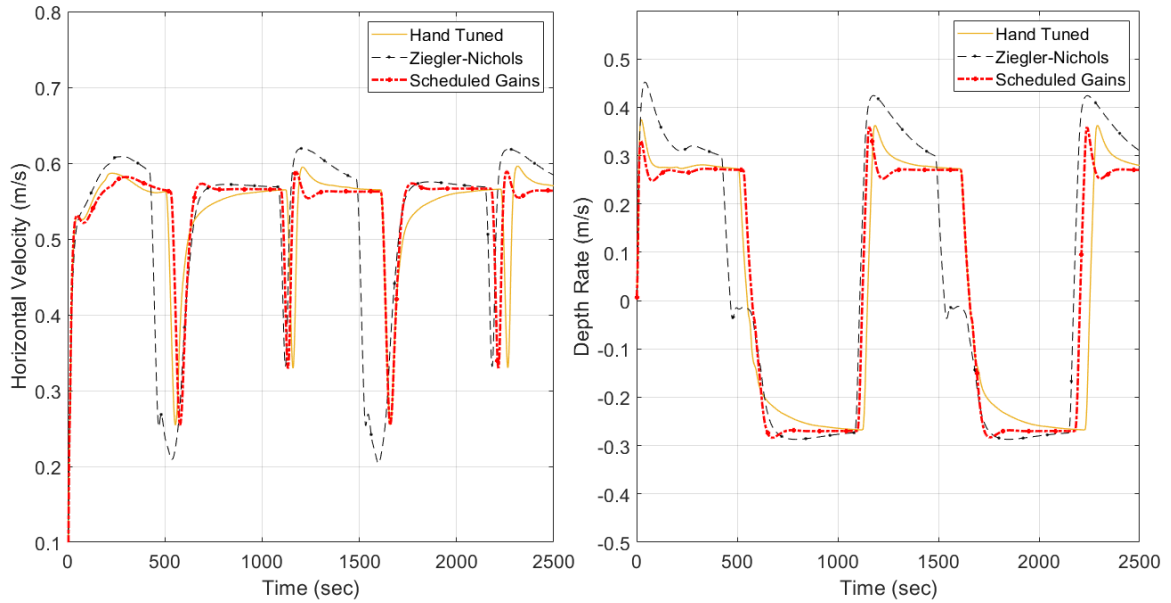
Figure 4-9. Vehicle Velocity Comparison

The results are shown in Figure 4-10.

For these runs, rather than pre-positioning the ballast mass at ±10mm during the inflections, the pitch set point was linearly changed between the positive and negative set points. Note that with the same Z-N gains, the response is significantly worse through the inflections than when manually inflected (as seen in Figure 4-5). This implies a sensitivity to gain choice and actuator rates that is usually handled by manually inflecting between the glide phases. The hand-tuned gains respond well in this simulated scenario, but may not perform as well in real scenarios where the pumping rate of the buoyancy engine varies with depth. This is investigated in more detail in Section 4.3.1. Finally, the gain-scheduled controller performs very well when actively controlling through the inflections.
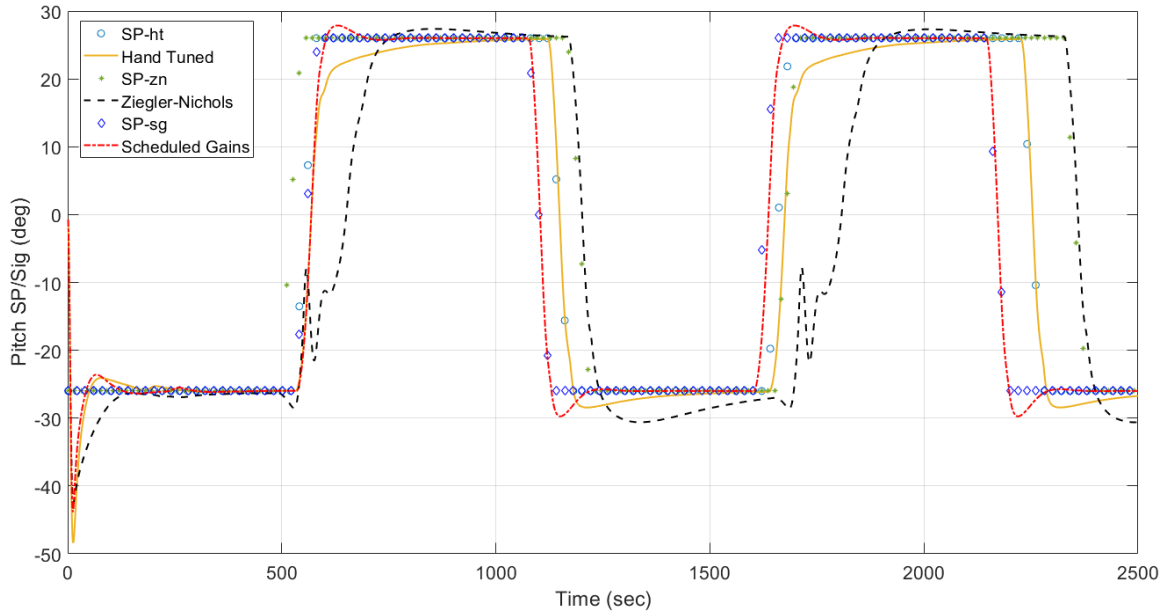
Figure 4-10. Pitch Control Through Inflections

4.3 Controller Robustness

There are a number of factors that can effect the performance of the glider controllers, including: varying actuator rates, sensor noise, and environmental disturbances. This section investigates the effects these plant and environmental disturbances might have on the static and gain-scheduled controllers. The gains used for the static gain controller are the same as the hand-tuned gains shown in Tables 4-I and 4-II, and the gain-scheduled controller is derived from the ζ and ω_n values described in Section 4.1.

4.3.1 Actuator Rates

With increasing depth there is increased pressure exerted on the buoyancy engine as it expels sea water from the vehicle and increases its buoyancy. This causes the buoyancy engine to pump out more slowly at deeper depths, which can have adverse effects on the control of the vehicle. Additionally, the ballast mass throw rate can degrade with time as motors and/or gearing wear down over long duration missions. To assess the impact of these effects on the pitch control of the vehicle, the static

and scheduled gain controllers were simulated with the original BE and battery throw rates, then again with the throw rates halved to emulate the effects described above. These values are shown in Table 4-IV and the simulation results can be seen in Figure 4-11. Heading control was not considered as the rudder deflection rate would not change dramatically enough to cause degradation in the steering control of the vehicle.

Table 4-IV. BE and Battery Throw Rates

Actuator	Original	Slow
BE (mL/s)	10	5
Battery (mm/s)	2.5	1.25
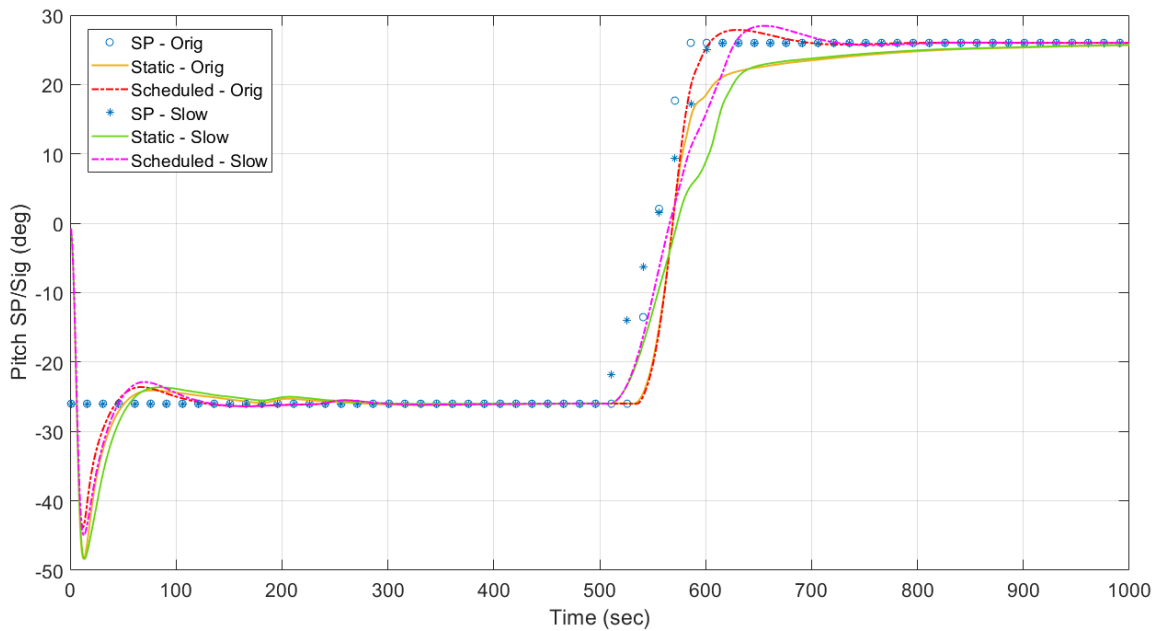
Figure 4-11. Effect of Actuator Degradation on Pitch Control

The effect of the slower actuators on the pitch angle of the vehicle can be seen when using both the static gain and gain-scheduled controller. In general, regardless of the controller that is used, the system is less responsive and takes longer to reach the desired set point. However, due to the increased responsiveness of the gain-scheduled controller, the increased lag caused by the slower actuators still results in improved control over the static gain controller. This implies that the gain-scheduled controller

has an increased robustness to actuator changes and modeling inaccuracies over the traditional static gain controller.

4.3.2 Sensor Noise

To assess and compare the effect of sensor noise on the static gain and gain-scheduled controllers, Gaussian noise was added to signals that are used by the simulated GNC to derive the glider state and update the control systems. To counteract the added noise, simple low-pass filters were added to the control loop to smooth the sensor noise on the feedback signal before calculating the error. Additionally, deadbands were introduced on the actuators to minimize spurious responses to the added noise. The standard deviations of the Gaussian noise are shown in Table 4-V. The filter coefficients for the pitch and heading signal were 0.5 and 0.1, respectively; and the deadbands for the moving battery mass and rudder were 0.2 mm and 1°, respectively. Simulated results are shown in Figures 4-12 and 4-13.

Table 4-V. Gaussian Noise Standard Deviations

Signal	St. Dev.
Depth (m)	0.005
Euler Angles (°)	0.5
Euler Rates (°/s)	0.1

The added noise was made more aggressive than would be expected from modern sensor equipment to illustrate the robustness of both static gain and gain-scheduled controllers to sensor noise. The main effect of the noise on both controllers was an increase in actuator motion due to sensed perturbations on the pitch and heading angles. In both the pitch and heading cases, the static gain controllers took slightly longer to reach the set points than without noise, which is to be expected. By comparison, the gain-scheduled controller reached the set points in roughly the same amount

72
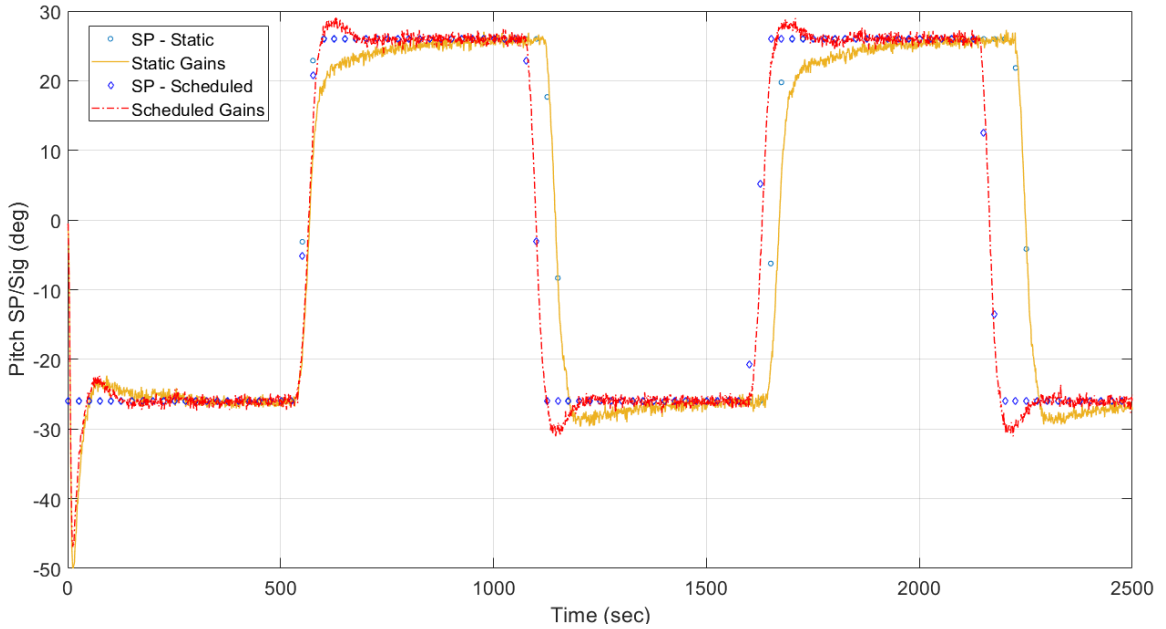
Figure 4-12. Effect of Sensor Noise on Pitch Control

of time as without noise, but fluctuated about the set point once there. This is also to be expected given the noisy sensor measurements.

Figure 4-14 shows the pitch gains that were calculated during the simulated runs. The static gains are the solid orange line, while the scheduled-gains are the dash-dot red line. Note the increased magnitude of the scheduled K_d gain, which implies increased sensitivity to noise. Additionally, the gain-scheduling relies on estimates of the glider's speed through the water, which is derived from both the depth and pitch measurements. All of this makes the gain-scheduled controller more sensitive to noise than the static gain controller. Despite this sensitivity, the gain-scheduled controller still outperforms the static-gain controller as far as time response characteristics are concerned.
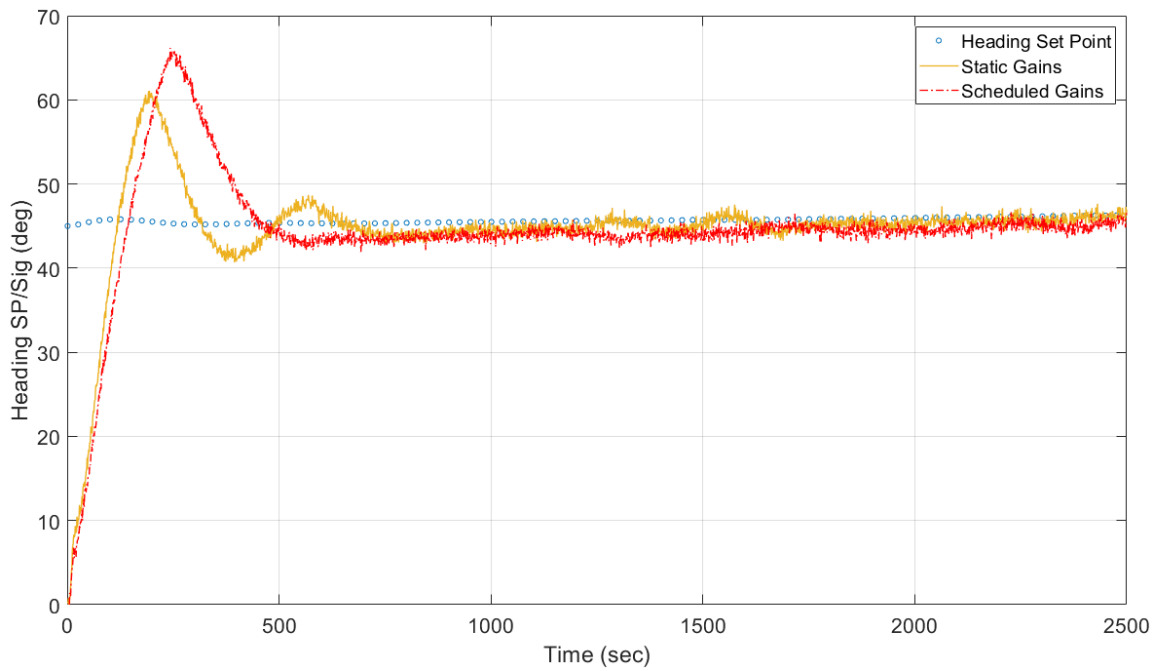
Figure 4-13. Effect of Sensor Noise on Heading Control
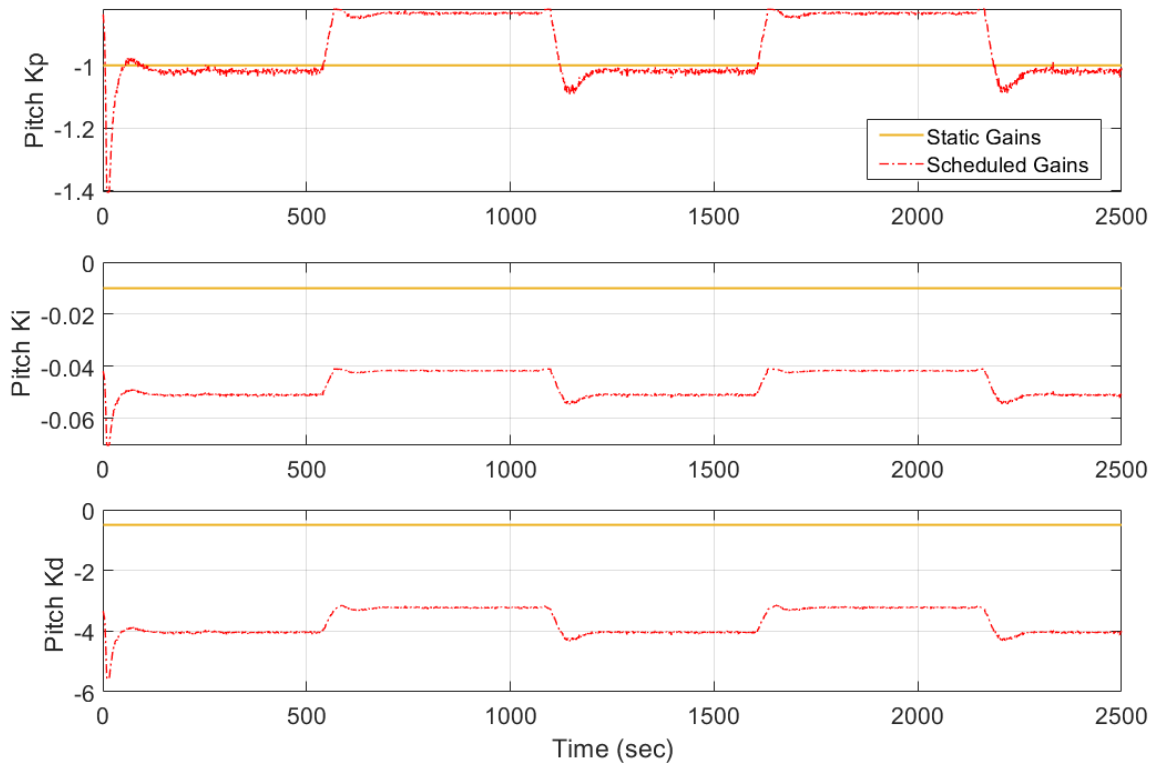
Figure 4-14. Pitch Controller Gains with Added Noise

74

4.3.3 Environmental Disturbances

To assess and compare the impact of environmental disturbances on the static gain and gain-scheduled controllers, density changes and water currents were added to the simulation. The density and current models are described in more detail in Section 2.5.
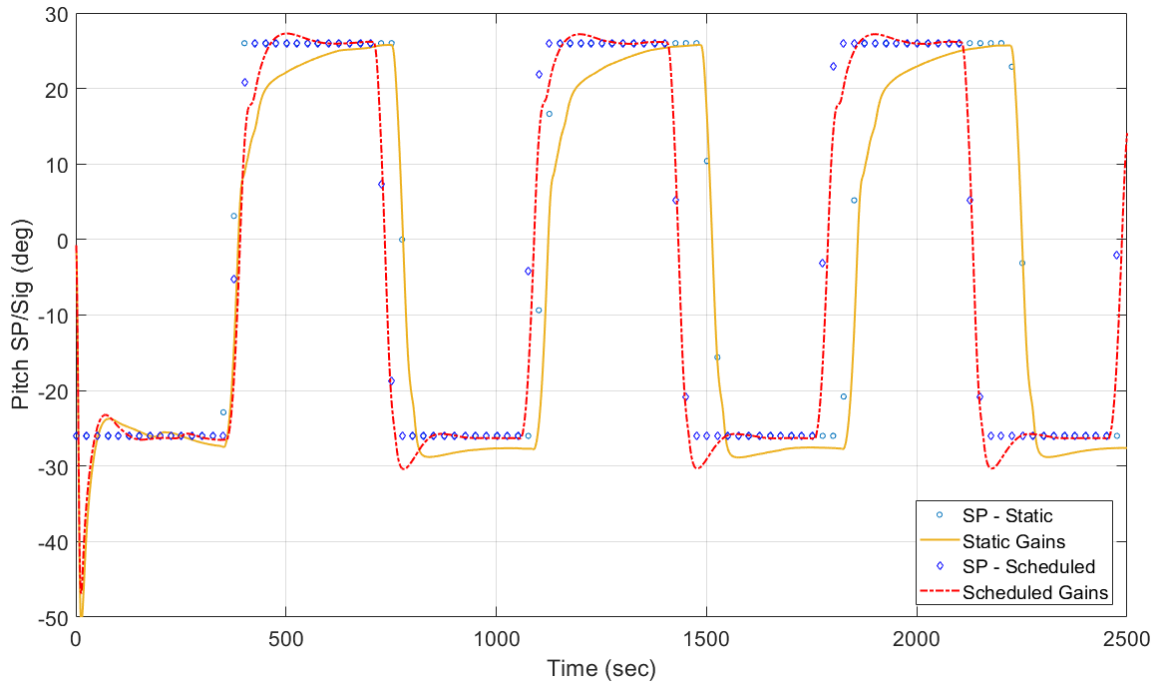
Figure 4-15. Effect of Density Changes on Pitch Controller

Figure 4-15 shows the effect of density changes on the pitch control of the vehicle. For this simulation the density delta was set to 2 kg/m^3, which caused roughly 1 kg/m^3 of density change in the first 100 m of water depth. This can be seen in Figure 4-16 where the solid orange line is the density seen by the glider with static gains, and the dash-dot red line is the density seen by the glider with scheduled gains.

With density changes added to the simulation as the glider dives through the water column, the density of the water around it increases slightly, effectively causing the vehicle to become lighter in the water as its buoyancy increases. This causes the

75
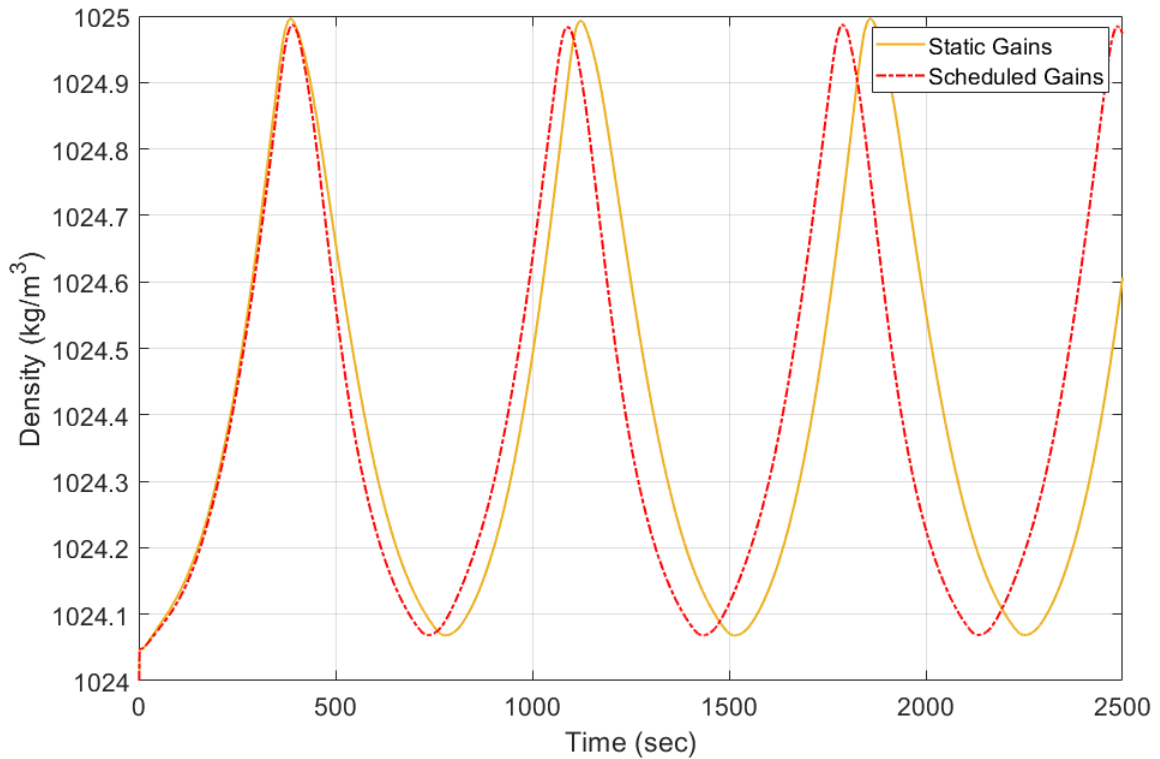
Figure 4-16. Density Change with Depth

weight distribution of the vehicle to change slightly, which effects the pitching moment on the vehicle. In past simulations when the density of the water was uniform, the static gain controller was able to reach the pitch set points during both upward and downward glides. With the changing water density, the static gain controller struggles to reach either set point, and never quite reaches the downward set point before the inflection. In the case of the gain-scheduled controller, there is minimal effect on the pitch performance of the vehicle despite the density stratification. For both controllers, there was minimal effect on the steering performance of the glider.

Figure 4-17 shows the effect of currents on the heading control of the vehicle. For this simulation the maximum current magnitude was set to 0.15 m/s ($\sim$0.3 knots) and the direction was set to be North-to-South, such that the vehicle was gliding into and across the current. The current magnitude with depth is shown in Figure 4-18 where

the solid orange line is the current magnitude seen by the glider with static gains, and the dash-dot red line is the current magnitude seen by the glider with scheduled gains.
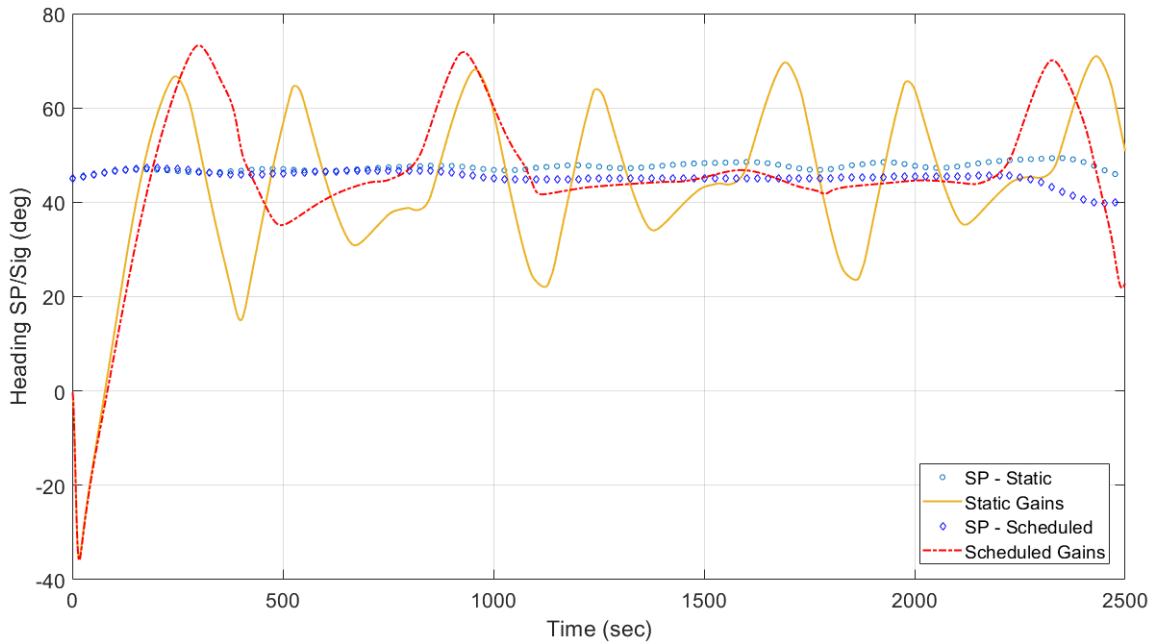
Figure 4-17. Effect of Currents on Heading Controller

With currents added to the simulation, both simulated gliders are pushed off course during the glides and inflections. The static gain controller struggles to compensate for these additional forces and moments, causing the vehicle to oscillate widely about the heading set point. The gain-scheduled controller does a better job at handling these disturbances and keeps it's heading fairly straight throughout the simulation. Both simulated gliders appear to be especially susceptible to mis-steer during inflections, which is likely due to additional roll and yaw moments caused by the currents amplifying the rudder-roll coupling inherent in the vehicle, which in turn induces adverse yaw moments on the vehicle.

4.4   Controller Efficiency

Power efficiency is one of the main benefits of an underwater glider compared to traditional UUVs; therefore, the efficiency of the controller is of utmost importance.
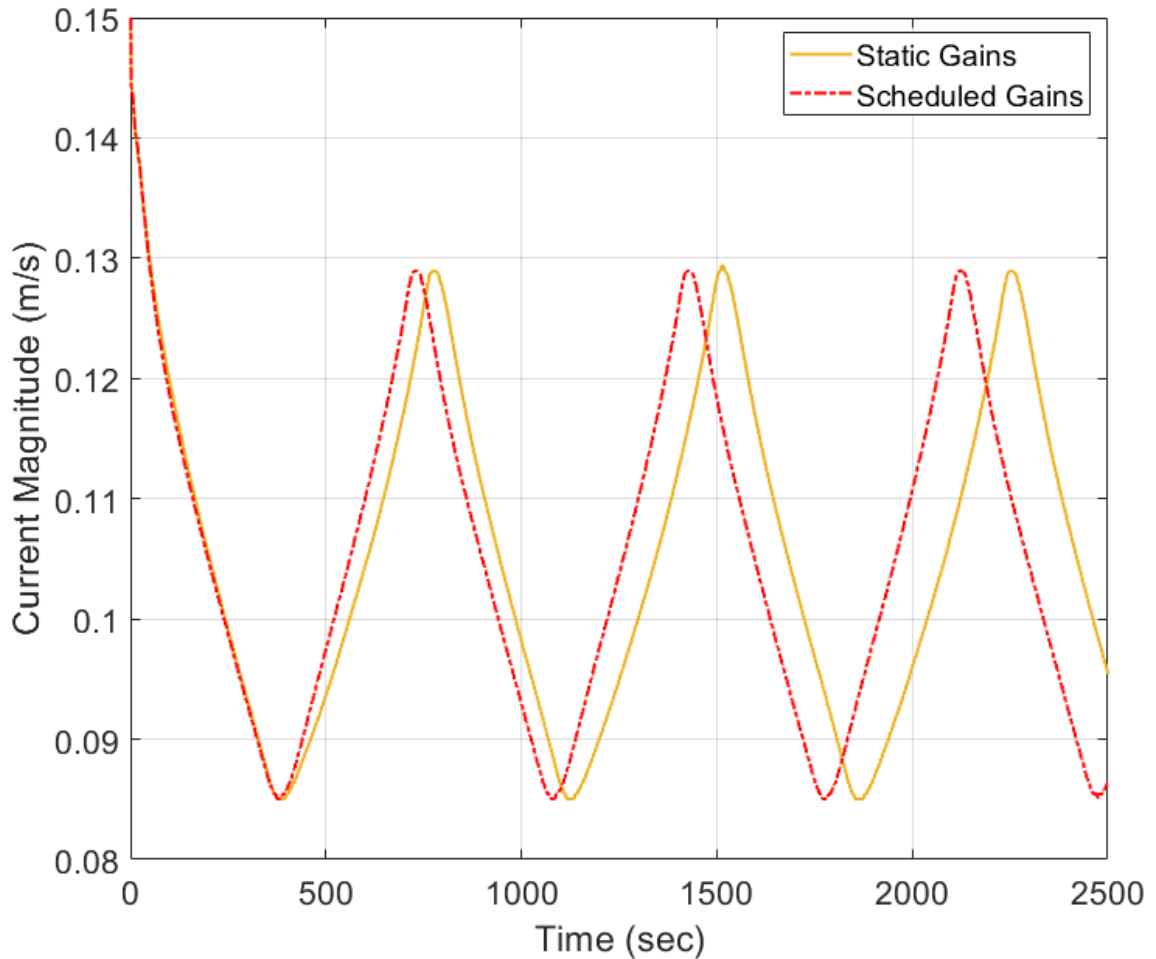
Figure 4-18. Current Magnitude with Depth

Beyond simply choosing more power efficient actuators, there are a number of parameters that can be adjusted to effect the efficiency of a glider's motion controller, such as the controller update rate, actuator deadbands, as well as the pitch angle, depth rate, and max depth the glider is commanded to fly to. For the purposes of this analysis, a one-to-one comparison was done between the static gain controller and the gain-scheduled controller, and the total actuator travel was used as a substitute measure for power efficiency.

Figure 4-19 shows the accumulated actuator travel for the three actuators of the simulated glider. The solid orange lines are the results with the static gain controller,
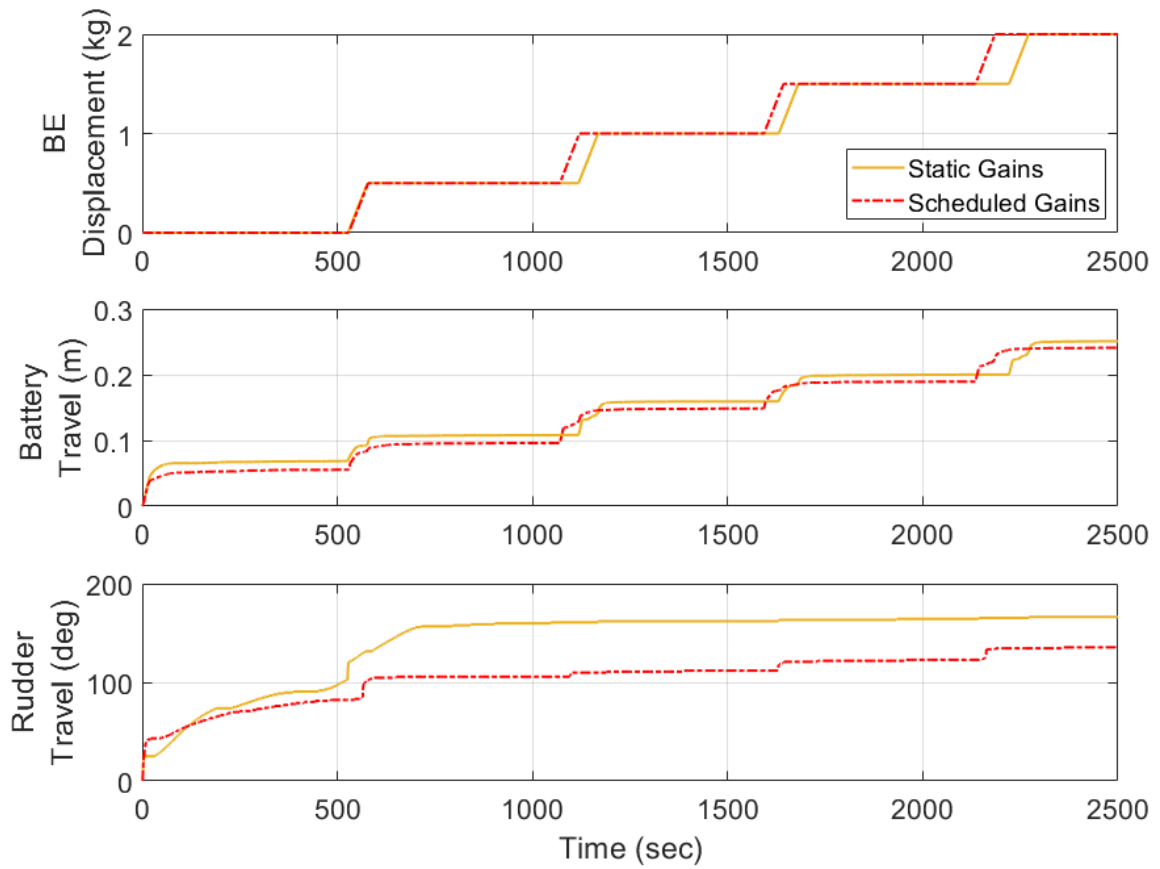
Figure 4-19. Actuator Travel Comparison

while the dash-dot red lines are the results with the gain-scheduled controller. Similar to the previous simulation runs, the glider was commanded to dive to a max depth of 150 m, and the battery and rudder actuators had deadbands of 0.2 mm and 1°, respectively. The ζ and ω_n values used to select the gains for the gain-scheduled controller are those described in Section 4.1; therefore, the pitch and heading responses are effectively the same as those in Figures 4-5 and 4-6. These results show that, given the exact same vehicle, with the exact same parameters, the gain-scheduled controller provides better pitch control performance, and comparable heading control performance, while using less power to drive the actuators and being more robust to changes in the plant dynamics and environment.

Chapter 5

Conclusions and Future Work

The principle goal of this thesis was the development and application of a straightforward methodology for the design of a gain-scheduled control scheme for an underwater glider. Underwater gliders have demonstrated their utility in oceanographic research as data collection platforms, and their potential can be enhanced by the application of the methods presented here. The methodology developed in this work provides insight into the nonlinear physical processes governing the dynamics of gliders and presents a realizable control scheme that increases the performance and robustness of glider motion control. Motivated by a desire to increase the performance of underwater gliders, this work attempted to answer the question of how best to improve the motion control of this novel vehicle, while minimizing the changes needed on the platform itself.

In Chapter 2, a simplified and generalizable dynamical model of an underwater glider was derived based on first principles. The presented model is not vehicle specific and therefore has applications in glider design and optimization, control algorithm development, and state estimation. Using this model, a nonlinear simulation specific to a Slocum glider was developed through the use of CAD and CFD software packages. This simulation was developed using the Matlab environment. The CFD-derived nonlinear hydrodynamic coefficients were used in the numerical simulation to create a "truth" simulation of the vehicle that could be used for characterization of the motion

control system. Additionally, environmental models were included in the simulation to assess the controller's robustness to environmental disturbances.

Chapter 3 describes the development of a gain-scheduled controller for an underwater glider using the dynamical model derived in Chapter 2. The general control architecture of underwater gliders is outlined, then the longitudinal dynamics of the system are linearized and used to derive a transfer function for the pitching dynamics of the vehicle. The Nomoto approximation is used to approximate the steering dynamics of the glider, and the numerical simulation is used to acquire the steady-state gains and time constants for the turning dynamics of the system at various operating points. The transfer functions are used to derive gain selection equations for the pitch and steering controllers, and these equations are used to generate gain lookup tables that can be incorporated into the simulation with minimal changes to the standard controller topology.

A comparative analysis between the traditional static gain controller and the gain-scheduled controller is performed in Chapter 4. A sensitivity study was performed to determine the tuning parameters for the scheduled gains and then the pitch and heading controllers were compared using static gains and gains that were derived using the methods outlined in Chapter 3. Performance improvements were realized in the pitch and heading responses of the vehicle, its speed over ground, and its stability when controlling through inflections. Improvements in the robustness of the gain-scheduled controller to changes in actuator rates, sensor noise, and environmental disturbances were also investigated. And finally, the power efficiency of the gain-scheduled controller was shown to be comparable, if not better than, that of the static gain controller.

The gain-scheduled controller demonstrated here showed marked improvements in

a number of metrics, but required a significant amount of simulation to derive. In particular, the CFD runs used to derive the nonlinear hydrodynamic coefficients numbered in the hundreds. Additionally, the Nomoto approximation used to derive the steering transfer function required dozens of simulations runs in order to characterize the steady-state gain values at each combination of pitch angle and depth rate. A purely analytical approach would require less simulation time, but would likely only be an approximation to the true turning dynamics of the vehicle.

Another difficulty with the methodology described here is the selection of the proper tuning parameters for the gain selection equations. It was shown that improved performance could be achieved by using more aggressive gains, but power efficiency would suffer due to increased actuator usage. Increased derivative gains also have the drawback of increasing the systems sensitivity to sensor noise. All of this requires consideration when choosing the proper ζ and ω_n values for gain tuning. That said, a sophisticated simulation of an underwater glider has been developed here and can be leveraged for gain tuning and controller validation.

Future Work

Recommendations for future work in this area include validation of the nonlinear hydrodynamic coefficients and the gain-scheduled control scheme through at-sea experiments of a Slocum glider, as well as further application of the dynamical model to analysis of glider dynamics, control and design. Due to the use of the underlying PID controllers, implementation of the gain-scheduled controller on a Slocum vehicle is not expected to be difficult; however, true comparisons between the static gain and gain-scheduled controllers would require testing in a "clean" environment that does not vary much with time, which may be challenging to find. Another option might be the implementation of this control scheme on a laboratory scale glider that can be

tested in a tank or pool to allow for controlled testing and analysis.

The analysis presented here suggests that a gain-scheduled controller may lead to significant performance gains and an increase in robustness over traditional static gain controllers. Additional performance gains may be realized through adjustments in the total glider volume, resizing of the internal ballast systems, and/or the reshaping of external geometries, such as the wings, nose and tail. The design of any vehicle is subject to a number of tradeoffs, and this work is a step toward the goal of developing an optimal approach for the design of glider control systems that are realizable with modern sensors and hardware.

Appendix A

Slocum CAD Dimensional Drawings

All dimensions are in inches.
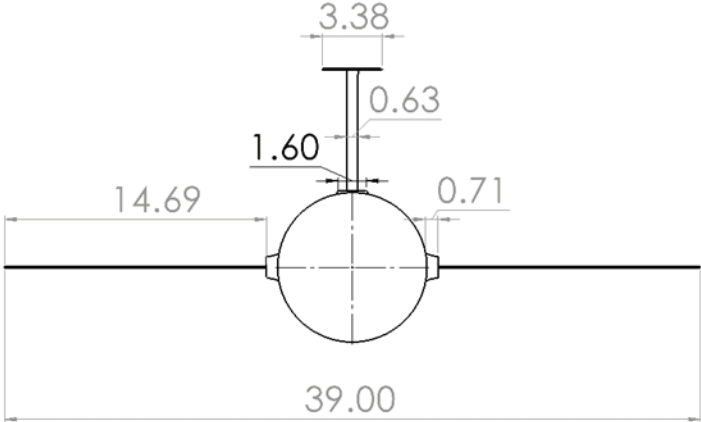
Figure A-1. Slocum Dimensions - Front View
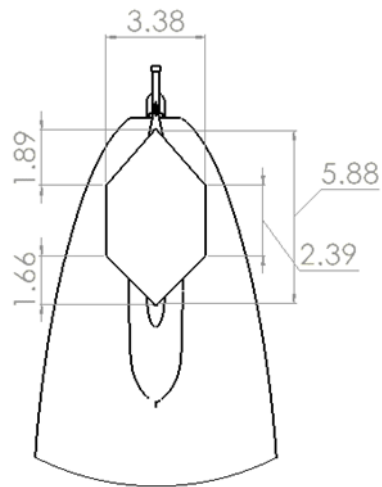
Figure A-2. Slocum Dimensions - Top View Tail
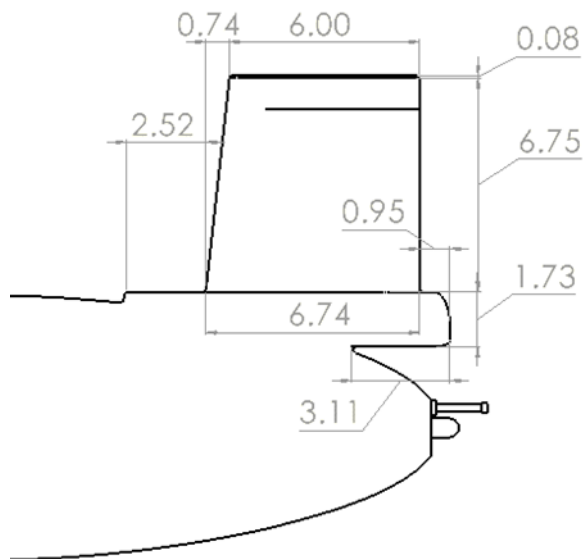
Figure A-3. Slocum Dimensions - Side View Tail
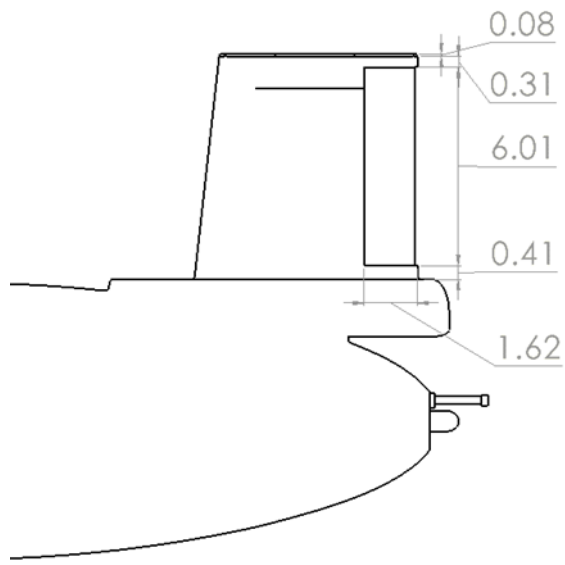
Figure A-4. Slocum Dimensions - Side View Rudder

Appendix B

Solidworks Flow Simulation Parameters

Typical run time: 1-3 hours per permutation

Local Mesh Settings

- **Level of Refining Fluid Cells:** 3 out of 9

- **Level of Refining Cells at Fluid/Solid Boundary:** 3 out of 9

- **Characteristic Number of Cells Across Channel:** 14

- **Maximum Channel Refinement Level:** 1 out of 9

- **Small Solid Feature Refinement:** 1 out of 9

- **Maximum Height of Slots to Close:** 3.9 cm

Global Mesh Settings

- **Type:** Automatic

- **Level of Initial Mesh:** 6 out of 7

- **Ratio Factor:** 1

Fluid and Thermal Characteristics

- **Fluid Type:** Water

- **Flow Type:** Laminar Only

- **Cavitation:** None

- **Wall Thermal Condition:** Adiabatic

- **Roughness:** 50 micrometers

- **Pressure:** 14.7 lbf/in^2

- **Temperature:** 20.05 °C

Velocity Parameters

- **Defined by:** Aerodynamic Angles

- **Velocity:** -0.5 m/s (0.97 knots)

- **Longitudinal Plane:** YZ

- **Longitudinal Axis:** Z

Computation Domain

- **Type:** 3D Simulation

- **X Distance:** $\pm$2.13 m

- **Y Distance:** +2.02/-1.75 m

- **Z Distance:** +1.85/-4.35 m

Calculation Control Options

- **Stop Criteria:** 500 Iterations and Refinement Finished

- **Global/Local Refinement Levels:** 7 out of 7

- **Approximate Maximum Cells:** 2,000,000

- **Refinement Strategy:** At iterations 80 and 160

- **Relaxation Interval:** 100

PC Specifications

- **Processor:** Water Cooled Intel i7-10700 (2.9GHz)

- **GPU:** NVIDIA GeForce GTX 1650

- **RAM:** 32GB DDR4 3600MHz

- **Hard Drive:** 1TB SSD NVMe m.2

Appendix C

Hydrodynamic Coefficient Data

Table C-I. Drag Coefficient Values Without Rudder

Without Rudder

Angle of Sideslip (deg)	\ Angle of Attack (deg) → 30	25	20	15	10	7.5	5	4	3	2	1	0	-1	-2	-3	-4	-5	-7.5	-10	-15	-20	-25	-30
-30	-4.086																						-0.043
-25		-1.449	0.424	0.807		2.331														2.014	1.529	1.063	
-20		-0.306	0.503	1.136		2.532														2.501	2.268	1.448	
-15		-0.014	0.804	1.528		2.597														2.890	2.272	1.809	
-10	-0.052				2.491														3.187				1.200
-7.5		0.492	1.301	1.720		2.960												3.262		2.782	2.527	1.327	
-5							2.887	3.082	2.848	3.173	3.303	3.230	3.156	3.239	3.110	3.465	2.969						
-4							3.012	2.968	2.787	3.142	3.300	3.329	3.358	3.078	3.331	3.397	2.986						
-3							2.855	3.041	2.808	3.173	3.263	3.213	3.163	3.157	3.118	3.251	2.804						
-2							2.864	2.943	2.758	3.255	3.326	3.276	3.225	3.317	2.905	2.970	2.693						
-1							2.807	2.944	2.728	3.257	3.398	3.389	3.379	3.278	2.985	3.186	2.791						
0							2.712	2.954	2.713	3.190	3.260	3.123	3.187	3.124	2.992	3.027	2.862						
1							2.883	2.932	2.809	3.089	3.253	3.248	3.243	3.125	2.997	3.171	2.940						
2							2.855	2.939	2.747	3.226	3.271	3.250	3.230	3.207	3.082	3.137	2.808						
3							2.921	2.981	2.787	3.205	3.233	3.207	3.181	3.223	3.240	3.198	2.851						
4							2.983	3.064	2.800	3.139	3.334	3.222	3.110	3.272	3.238	3.308	3.004						
5							2.995	3.225	2.845	3.150	3.455	3.288	3.121	3.340	3.076	3.328	3.097						
7.5				1.799		2.824												3.080		2.523	2.543	1.668	
10	-0.370				2.455														3.156				0.410
15		0.450	0.708	1.464		2.595														2.810	2.270	2.161	
20		-0.349	0.601	1.151		2.339														2.476	2.241	1.374	
25		-1.232	0.335	0.846		2.393														1.979	1.486	1.129	
30	-3.623				2.553														3.194				0.098

91

Table C-II. Lift Coefficient Values Without Rudder

Without Rudder

Angle of Sideslip (deg)	Angle of Attack (deg)																						
	30	25	20	15	10	7.5	5	4	3	2	1	0	-1	-2	-3	-4	-5	-7.5	-10	-15	-20	-25	-30
-30	181.3				81.6														77.5				168.3
-25		170.6	136.8	215.4		138.0												202.2		190.6	190.3	170.5	
-20		190.0	167.7	188.5		200.7												189.3		201.0	173.5	197.5	
-15		189.2	188.6	183.5		190.0												218.3		199.8	183.6	192.0	
-10	171.2				173.7														215.7				182.1
-7.5		183.1	193.0	178.5		250.2												246.1		186.6	201.0	192.6	
-5							234.8	275.5	256.5	272.9	276.7	286.7	296.7	291.0	260.6	272.1	237.4						
-4							238.5	276.0	253.7	271.5	280.0	293.6	307.1	315.3	268.7	257.5	239.3						
-3							240.4	278.6	259.0	270.7	276.6	294.2	311.9	290.3	262.9	265.6	245.5						
-2							240.6	282.4	258.5	272.5	262.2	285.2	308.2	343.3	276.8	260.1	245.0						
-1							240.6	288.8	261.6	277.3	282.0	304.7	327.4	331.0	267.2	268.1	248.2						
0							237.7	277.3	263.8	260.5	261.0	275.5	316.6	334.8	275.0	273.6	254.4						
1							242.0	287.4	263.1	283.9	268.3	293.5	318.7	323.5	272.0	272.8	248.3						
2							246.7	282.3	259.3	270.9	284.6	297.4	310.2	316.8	265.0	266.8	250.7						
3							242.7	282.7	258.1	278.6	272.2	285.5	298.9	311.2	256.4	264.8	244.9						
4							235.7	276.5	254.3	278.3	268.2	282.3	296.4	307.4	255.8	262.5	241.4						
5							231.9	247.5	256.4	276.5	272.0	295.6	319.1	299.6	261.6	263.4	238.8						
7.5		181.8	192.2	181.9		253.7												262.7		188.6	199.7	188.8	
10		184.1			171.9														218.9				195.4
15		179.4	187.9	178.2		191.8												215.1		190.5	182.7	189.0	
20		193.3	167.8	188.5		185.4												186.8		203.4	173.4	196.6	
25		170.1	139.1	213.3		140.3												159.4		193.3	198.0	166.3	
30	174.2				81.8														74.9				167.8

92

Table C-III. Side Force Coefficient Values Without Rudder

Without Rudder

Angle of Sideslip (deg)	Angle of Attack (deg)																						
	-30	-25	-20	-15	-10	-7.5	-5	-4	-3	-2	-1	0	1	2	3	4	5	7.5	10	15	20	25	30
-30	-99.92				-120.81														-117.38				-89.17
-25		-99.16	-84.25	-89.77		-102.27												-100.51		-102.29	-105.49	-97.89	
-20		-78.12	-87.78	-75.02		-86.25												-95.96		-76.44	-101.41	-93.96	
-15		-95.18	-81.33	-59.92		-72.77												-75.70		-73.87	-83.91	-74.42	
-10	-156.11				-65.09														-66.48				-155.84
-7.5		-95.87	-96.00	-83.66		-80.84												-60.00		-74.48	-86.72	-80.92	
-5							-84.16	-89.45	-71.93	-77.41	-54.39	-56.93	-57.83	-59.29	-52.72	-74.44	-58.00						
-4							-67.92	-71.57	-98.22	-61.74	-30.27	-58.13	-59.16	-55.61	-56.28	-66.15	-71.61						
-3							-52.19	-86.23	-66.81	-70.47	-38.76	-53.76	-51.97	-54.90	-46.71	-74.33	-62.57						
-2							-101.83	-56.23	-77.31	-73.71	-0.42	-38.38	-37.19	-38.97	-49.93	-70.37	-66.85						
-1							-49.13	-28.57	-80.80	-197.76	-99.19	-73.93	2.78	-54.69	-77.61	-115.21	-84.99						
0							-119.42	-5.12	-82.37	-136.30	-59.00	-58.69	-18.71	-68.63	-84.54	-102.85	-88.22						
1							-189.71	18.33	-83.95	-74.83	-18.80	-89.86	-40.20	-82.57	-91.47	-90.50	-91.45						
2							-78.48	-41.37	-91.56	-81.17	-53.53	-45.30	-26.86	-38.04	-52.97	-74.24	-57.64						
3							-82.36	-73.10	-91.42	-66.09	-37.27	-56.59	-55.55	-56.51	-51.35	-70.09	-58.82						
4							-92.08	-67.41	-90.28	-73.16	-69.15	-53.15	-30.77	-61.60	-60.42	-55.83	-68.71						
5							-81.65	-70.59	-70.05	-75.07	-50.51	-60.88	-43.20	-59.82	-57.33	-44.78	-64.83						
7.5		-133.22	-90.57	-79.66		-75.51												-59.75		-57.74	-78.27	-87.42	
10	-84.20				-70.40														-68.23				-66.37
15		-101.20	-82.99	-69.63		-74.80												-73.79		-74.79	-86.42	-95.49	
20		-80.21	-89.55	-74.72		-86.21												-84.02		-78.45	-100.49	-89.07	
25		-101.33	-79.50	-89.83		-105.74												-101.31		-102.61	-106.07	-96.91	
30	-100.91				-128.37														-117.30				-95.38

Table C-IV. Roll Moment Coefficient Values Without Rudder

Without Rudder

Angle of Sideslip (deg) \ Angle of Attack (deg)	-30	-25	-20	-15	-10	-7.5	-5	-4	-3	-2	-1	0	1	2	3	4	5	7.5	10	15	20	25	30
-30	-0.472				-0.499	-1.371												-2.287	-2.303				-3.196
-25		-0.132	-0.290	-0.269		-0.116												-1.323		-3.180	-2.348	-2.663	
-20		-0.749	-0.464	0.086		0.036												-1.394		-2.329	-1.847	-1.763	
-15		-0.947	-0.263	-0.052																-1.967	-1.433	-0.623	-0.333
-10																			-1.055				-0.034
-7.5	-0.295	-0.620	-0.586	-0.342	-0.525	-1.323												-0.289		-0.983	-0.395	-0.141	
-5							-0.273	-0.412	-0.303	-0.381	-0.297	-0.491	-0.438	-0.521	-0.547	-0.346	-0.637						
-4							-0.206	-0.192	-0.367	-0.259	-0.127	-0.395	-0.386	-0.432	-0.477	-0.283	-0.590						
-3							-0.097	-0.269	-0.198	-0.233	-0.170	-0.284	-0.279	-0.313	-0.359	-0.173	-0.429						
-2							-0.125	-0.142	-0.164	-0.178	-0.074	-0.181	-0.167	-0.190	-0.203	-0.125	-0.277						
-1							-0.013	-0.043	-0.098	-0.264	-0.109	-0.127	-0.046	-0.108	-0.107	-0.107	-0.167						
0							0.062	-0.011	-0.014	-0.091	-0.034	0.017	0.037	0.012	0.008	-0.010	0.017						
1							0.138	0.022	0.069	0.082	0.040	0.146	0.121	0.133	0.122	0.087	0.202						
2							0.121	0.115	0.166	0.249	0.134	0.192	0.151	0.180	0.208	0.117	0.238						
3							0.167	0.231	0.212	0.200	0.169	0.301	0.300	0.327	0.369	0.196	0.389						
4							0.268	0.204	0.334	0.299	0.333	0.387	0.303	0.449	0.498	0.162	0.565						
5							0.277	0.391	0.305	0.369	0.280	0.489	0.387	0.504	0.590	0.597	0.654						
7.5	0.461	0.747	0.833	0.286	0.383	1.637												0.306		0.963	0.188	0.044	
10																			1.095				
15		0.624	0.249	0.112																2.025	1.459	0.698	
20		0.841	0.594	0.018		-0.042												1.399		2.362	1.862	1.747	
25		0.195	0.287	0.290		0.184												1.587		3.053	2.364	2.797	
30	0.720				0.598	1.229												2.366	2.280				3.280

Table C-V. Pitch Moment Coefficient Values Without Rudder

Without Rudder

Angle of Sideslip (deg) \ Angle of Attack (deg)	-30	-25	-20	-15	-10	-7.5	-5	-4	-3	-2	-1	0	1	2	3	4	5	7.5	10	15	20	25	30
-30	9.243				44.835														58.704				9.957
-25		12.264	7.023	11.558		17.277												42.543		13.955	24.970	14.373	
-20		9.338	13.592	9.040		17.622												27.318		11.544	19.186	13.120	
-15		12.349	12.536	9.579		9.752												14.235		13.972	16.146	15.290	
-10	14.796				9.943														16.742				21.052
-7.5		11.553	12.673	13.700		13.425												16.142		18.982	19.162	17.467	
-5							13.826	3.685	6.709	7.698	3.856	12.195	20.534	16.974	17.171	14.243	18.587						
-4							14.830	10.779	0.228	-7.443	-2.022	10.247	22.517	19.217	19.701	15.649	18.795						
-3							10.069	8.119	6.860	10.233	-6.130	10.569	27.268	21.518	19.713	17.678	19.274						
-2							11.539	11.720	0.847	-24.080	-0.931	16.937	34.806	19.551	22.012	17.382	19.203						
-1							10.202	6.709	7.718	-15.351	-18.956	3.100	25.156	16.869	20.762	15.290	20.317						
0							6.862	2.673	2.265	-13.780	-13.440	8.564	25.800	19.577	19.478	17.706	18.500						
1							10.027	3.556	1.773	-11.281	-13.474	4.247	21.967	18.937	19.132	16.236	18.908						
2							8.601	6.389	5.380	-6.079	-6.472	9.168	24.807	20.614	20.236	17.394	18.563						
3							11.235	7.853	12.948	-5.426	1.015	16.309	31.602	17.615	20.254	16.143	19.923						
4							13.288	8.135	9.095	-4.441	-1.926	12.209	26.344	16.322	18.785	17.852	20.282						
5							13.496	8.610	5.844	-0.066	-15.670	0.608	16.887	14.539	17.503	17.934	20.252						
7.5		12.325	12.311	13.660		8.859												15.131		17.935	17.980	18.495	
10	11.811				11.034														16.865				17.041
15		11.687	12.833	10.949		10.616												14.248		14.886	16.602	17.172	
20		9.671	13.373	8.563		17.977												23.297		11.337	19.347	12.379	
25		12.805	4.777	10.673		33.679												41.671		14.411	23.913	14.687	
30	10.643				45.966														58.297				11.750

95

Table C-VI. Yaw Moment Coefficient Values Without Rudder

Without Rudder

Angle of Attack (deg) \ Angle of Sideslip (deg)	-30	-25	-20	-15	-10	-7.5	-5	-4	-3	-2	-1	0	1	2	3	4	5	7.5	10	15	20	25	30
30	12.239				13.665														1.063				9.586
25		8.559	10.481	23.191	28.033													2.536		1.954	3.307	9.523	
20		3.508	8.203	12.580	10.082													8.734		5.892	8.348	11.469	
15		2.308	6.994	8.433	9.474													10.329		10.346	12.097	19.101	
10	9.425				12.623													11.963	34.337				0.905
7.5	21.858	3.146	6.717	9.441	14.052													13.613		15.896	14.461	31.899	
5							7.972	-0.548	4.348	2.103	-9.730	-11.869	-14.009	8.287	6.732	1.506	4.431						
4							-2.004	3.650	-1.212	1.367	-28.692	-20.090	-11.487	-0.920	0.454	10.903	18.532						
3							12.256	10.001	15.765	13.331	-5.608	-9.155	-12.703	12.245	12.340	7.215	8.829						
2							7.724	9.927	10.924	21.665	11.884	1.927	-8.029	22.532	9.466	5.720	7.363						
1							9.150	7.890	12.618	22.175	50.460	35.130	19.800	29.271	9.084	26.837	19.634						
0							9.797	9.112	11.941	22.337	-1.917	8.493	-12.158	17.212	9.522	12.050	7.033						
-1							11.089	28.474	21.868	49.938	-24.527	5.197	34.920	11.826	23.068	0.226	14.410						
-2							-4.409	6.160	-0.561	-3.608	-90.059	-46.063	-2.068	-7.998	3.178	-1.683	-2.851						
-3							-1.583	-20.550	4.044	-6.559	-5.101	-7.286	-9.470	-14.994	-14.119	-13.671	0.447						
-4							-13.921	-0.386	-11.235	6.921	26.512	43.395	60.277	20.223	-1.913	2.766	-0.453						
-5							-10.015	4.291	14.487	-22.861	20.851	-30.200	-81.250	-5.276	-8.062	-14.455	-7.289						
-7.5	13.606	13.766	0.415	0.500	-5.082													-3.332		1.136	3.603	3.839	
-10	12.389				-5.852																		-10.738
-15		15.912	14.598	16.163	12.291													9.786		13.159	13.363	15.188	
-20		16.186	11.544	9.943														5.593		9.945	10.942	15.196	
-25		10.329	10.232	5.935														-0.520		5.544	12.545	9.755	
-30	11.763																						

Table C-VII. Drag Coefficient Values With Rudder

	With Rudder at 20 degrees														
		Angle of Attack (deg)													
		-30	-10	-5	-4	-3	-2	-1	0	1	2	3	4	5	10	30
Angle of Sideslip (deg)	-30	0.064	3.568	2.367					1.247					2.016	2.759	-3.871
	-10	1.424	3.457	3.151					3.237					2.964	2.746	0.229
	-5	1.045	3.071	3.280	3.423	3.208	3.438	3.345	3.334	3.422	3.311	2.912	3.139	3.246	2.779	0.316
	-4			3.167	3.550	3.397	3.335	3.358	3.242	3.493	3.310	2.992	3.183	3.152		
	-3			3.090	3.357	3.285	3.365	3.362	3.300	3.522	3.394	3.022	3.191	3.082		
	-2			3.041	3.344	3.240	3.397	3.462	3.293	3.532	3.467	2.967	3.167	3.090		
	-1			3.022	3.333	3.208	3.405	3.523	3.323	3.547	3.445	2.990	3.148	3.052		
	0	1.097	3.169	3.035	3.342	3.252	3.385	3.466	3.337	3.590	3.489	3.012	3.273	3.069	3.010	0.134
	1			3.193	3.788	3.303	3.393	3.581	3.416	3.591	3.384	3.049	3.400	3.134		
	2			3.090	3.452	3.369	3.420	3.538	3.425	3.650	3.476	3.098	3.218	3.151		
	3			3.132	3.422	3.373	3.455	3.468	3.364	3.522	3.402	3.090	3.223	3.180		
	4			3.388	3.576	3.541	3.526	3.385	3.288	3.604	3.297	3.063	3.189	3.259		
	5	1.138	3.031	3.379	3.449	3.131	3.383	3.180	3.391	3.412	3.297	2.975	3.199	3.248	2.643	0.609
	10	0.891	3.398	3.251					3.522					3.201	2.648	-0.265
	30	0.958	3.493	2.489					1.850					2.470	2.864	-3.143

Table C-VIII. Lift Coefficient Values With Rudder

	With Rudder at 20 degrees														
		Angle of Attack (deg)													
		-30	-10	-5	-4	-3	-2	-1	0	1	2	3	4	5	10	30
Angle of Sideslip (deg)	-30	170.4	75.4	192.4					146.0					180.6	85.7	171.8
	-10	181.5	221.0	238.9					204.8					244.0	169.9	173.2
	-5	192.9	202.8	236.9	262.4	257.1	295.6	300.6	269.9	292.2	285.7	256.0	278.9	234.2	170.8	183.9
	-4			242.3	260.3	250.4	310.1	303.8	270.8	288.7	277.4	257.6	278.3	239.2		
	-3			241.1	266.1	264.7	318.4	300.1	272.2	288.7	270.5	252.2	279.9	240.3		
	-2			247.2	265.5	270.3	306.9	305.6	271.1	268.0	265.7	256.8	284.9	240.3		
	-1			248.8	268.7	269.4	321.9	311.1	274.4	257.3	276.9	263.6	287.1	239.5		
	0	196.9	200.4	250.3	273.6	273.8	337.3	327.4	282.6	289.5	279.0	264.4	288.8	241.5	168.9	190.0
	1			245.2	264.8	272.2	319.4	298.6	275.5	264.4	294.1	261.4	289.6	245.0		
	2			249.5	265.3	256.9	316.2	297.0	274.9	281.5	282.4	260.7	288.7	250.4		
	3			239.7	258.0	261.1	304.6	281.2	274.1	302.2	291.6	263.0	289.3	250.7		
	4			233.6	256.6	243.3	285.7	260.6	268.2	309.1	296.4	264.5	287.7	244.4		
	5	192.9	197.3	231.1	256.6	247.2	275.4	262.8	265.5	305.5	292.6	260.2	281.8	241.9	178.6	183.7
	10	194.9	216.1	233.9					208.8					252.0	174.7	181.5
	30	163.2	74.3	183.3					141.7					173.5	82.0	173.7

Table C-IX. Side Force Coefficient Values With Rudder

With Rudder at 20 degrees															
		Angle of Attack (deg)													
		-30	-10	-5	-4	-3	-2	-1	0	1	2	3	4	5	10	30
Angle of Sideslip (deg)	-30	-95.50	-117.81	-112.35					-127.16					-115.57	-112.76	-89.26
	-10	-164.05	-55.47	-69.36					-63.42					-63.58	-56.86	-138.61
	-5	-89.56	-32.78	-35.06	-75.57	-74.19	-79.71	-40.36	-62.31	-59.67	-61.87	-55.39	-64.08	-17.07	-37.30	-107.86
	-4			-67.92	-43.45	-85.21	-61.68	-29.54	-29.82	-48.83	-51.11	-45.91	-51.17	-57.00		
	-3			-60.28	-57.26	-48.83	-46.47	-18.33	-2.79	-37.48	-31.40	-23.85	-55.71	-44.57		
	-2			-53.07	3.09	-22.57	-49.59	5.36	16.43	-13.23	5.20	-14.28	-37.35	-34.75		
	-1			-14.57	65.09	8.93	0.34	71.49	86.58	49.17	49.62	34.28	-3.85	-20.75		
	0	-119.63	-93.12	-110.59	-83.45	-95.04	-93.60	-72.62	-60.90	-74.89	-72.67	-69.90	-112.39	-87.39	-89.64	-102.20
	1			-286.55	-225.40	-176.81	-152.64	-209.05	-148.16	-205.36	-170.86	-178.49	-385.22	-184.15		
	2			-136.72	-81.41	-173.09	-141.43	-164.18	-124.90	-103.21	-111.84	-120.80	-147.49	-127.94		
	3			-139.26	-149.04	-125.16	-134.53	-105.39	-110.97	-121.72	-121.25	-101.96	-128.98	-115.45		
	4			-168.08	-150.87	-140.88	-139.19	-133.24	-114.10	-103.67	-116.18	-99.38	-138.90	-144.32		
	5	-159.27	-123.22	-144.36	-119.68	-112.54	-131.10	-102.97	-118.90	-104.90	-116.98	-93.22	-111.11	-127.88	-112.88	-113.13
	10	-96.89	-94.45	-89.30					-94.13					-87.20	-92.98	-64.77
	30	-112.53	-135.00	-125.55					-143.58					-125.54	-125.05	-99.60

Table C-X. Roll Moment Coefficient Values With Rudder

With Rudder at 20 degrees															
		Angle of Attack (deg)													
		-30	-10	-5	-4	-3	-2	-1	0	1	2	3	4	5	10	30
Angle of Sideslip (deg)	-30	-0.249	-0.026	-1.564					-1.764					-2.150	-1.722	-2.759
	-10	-0.169	0.077	-0.129					-0.556					-1.061	-0.760	0.161
	-5	-0.071	0.347	0.421	-0.253	-0.305	-0.376	-0.169	-0.295	-0.425	-0.507	-0.553	-0.257	-0.012	-0.401	0.668
	-4			0.000	0.183	-0.256	-0.167	-0.040	-0.022	-0.258	-0.309	-0.351	-0.086	-0.360		
	-3			0.039	-0.032	0.015	-0.016	0.065	0.117	-0.116	-0.098	-0.128	0.022	-0.230		
	-2			0.123	0.189	0.123	-0.048	0.183	0.206	0.046	0.069	0.055	0.132	-0.061		
	-1			0.212	0.265	0.210	0.124	0.299	0.329	0.209	0.183	0.207	0.226	0.087		
	0	0.408	0.708	0.272	0.359	0.340	0.316	0.384	0.427	0.373	0.339	0.314	0.340	0.278	0.777	0.311
	1			0.487	0.867	0.425	0.381	0.553	0.483	0.582	0.463	0.466	1.006	0.528		
	2			0.502	0.488	0.640	0.632	0.724	0.673	0.618	0.598	0.619	0.579	0.639		
	3			0.641	0.815	0.712	0.784	0.734	0.814	0.860	0.885	0.846	0.698	0.847		
	4			1.174	1.100	0.897	0.977	1.021	0.928	1.000	1.047	1.001	1.029	1.434		
	5	0.893	1.032	1.147	1.056	0.887	1.135	0.960	1.060	1.084	1.275	1.104	0.891	1.543	1.648	0.372
	10	1.139	1.079	0.734					1.350					1.684	1.920	0.646
	30	1.229	1.081	2.798					3.183					2.994	2.713	3.613

Table C-XI. Pitch Moment Coefficient Values With Rudder

With Rudder at 20 degrees															
		Angle of Attack (deg)													
		-30	-10	-5	-4	-3	-2	-1	0	1	2	3	4	5	10	30
Angle of Sideslip (deg)	-30	8.895	44.392	33.562					33.049					39.996	58.720	12.730
	-10	15.062	8.488	10.607					14.135					11.144	18.979	20.529
	-5	12.996	13.852	13.378	10.565	8.656	3.981	2.371	10.597	10.275	8.227	16.732	12.093	19.692	22.652	19.582
	-4			12.163	9.153	12.321	-3.721	-1.418	11.129	17.762	15.012	16.892	14.392	18.733		
	-3			13.298	7.308	4.990	-6.864	-0.374	12.096	21.261	22.294	23.798	16.381	18.869		
	-2			9.771	7.257	4.603	0.105	-4.759	13.080	31.476	23.504	23.200	15.781	19.860		
	-1			9.506	6.069	4.916	-8.472	-9.393	10.725	31.706	16.801	19.547	15.952	20.615		
	0	11.354	14.608	8.758	3.734	2.696	-15.065	-20.085	7.428	22.634	17.315	19.601	15.867	18.825	22.414	18.455
	1			11.865	8.287	2.081	-8.927	-1.493	10.102	24.108	13.042	19.994	14.651	17.416		
	2			9.347	7.944	11.148	-4.104	0.811	11.475	27.983	13.358	19.311	12.763	16.194		
	3			14.412	12.381	7.622	-0.974	13.413	11.412	14.125	9.787	16.631	11.654	15.069		
	4			17.430	12.025	16.719	9.892	23.518	12.166	0.617	3.566	12.172	10.800	14.924		
	5	13.093	16.945	18.287	13.014	16.608	17.104	24.545	12.709	-2.329	1.741	13.926	9.886	14.313	17.633	19.340
	10	12.509	12.812	15.743					13.121					5.979	14.926	16.758
	30	11.622	45.889	40.278					34.316					37.520	58.589	11.997

Table C-XII. Yaw Moment Coefficient Values With Rudder

		With Rudder at 20 degrees														
		Angle of Attack (deg)														
		-30	**-10**	**-5**	**-4**	**-3**	**-2**	**-1**	**0**	**1**	**2**	**3**	**4**	**5**	**10**	**30**
	-30	16.024	-3.001	-0.628					-0.699					-0.656	5.104	14.160
	-10	11.124	21.066	3.612					9.838					5.852	20.723	26.831
	-5	27.006	28.497	29.007	-3.264	-2.927	-6.743	21.567	6.024	7.481	5.589	9.921	5.497	40.267	24.165	45.107
	-4			3.731	22.323	-10.225	6.390	29.686	28.643	15.624	13.978	17.874	15.134	11.070		
	-3			9.348	10.231	16.306	17.906	37.954	48.740	23.946	29.029	33.428	13.263	18.432		
	-2			15.673	55.271	36.089	16.830	56.558	64.283	42.104	55.585	42.141	28.450	27.915		
Angle	**-1**			49.428	101.839	62.916	56.914	109.073	118.472	91.568	91.687	80.655	56.925	43.321		
of	**0**	7.215	-3.611	-28.770	-12.366	-19.252	-18.039	-3.869	3.899	-5.737	-3.512	-1.443	-31.602	-13.690	0.069	23.497
Sideslip	**1**			-159.551	-134.785	-85.010	-64.567	-111.368	-69.348	-107.812	-79.737	-85.334	-246.215	-90.309		
(deg)	**2**			-51.830	-13.480	-79.194	-56.262	-74.882	-47.424	-31.121	-35.060	-41.382	-59.415	-47.294		
	3			-52.464	-60.426	-44.265	-50.694	-30.455	-35.875	-42.156	-41.590	-28.220	-45.457	-37.400		
	4			-74.638	-62.435	-53.341	-53.131	-50.104	-36.423	-29.090	-36.947	-24.235	-53.223	-57.837		
	5	-26.268	-43.059	-56.405	-38.935	-32.867	-47.037	-26.717	-38.104	-27.911	-37.653	-19.277	-30.982	-45.065	-36.793	14.425
	10	10.823	-9.469	-12.592					-13.726					-12.620	-8.411	34.494
	30	4.579	-15.700	-10.723					-14.794					-8.665	-4.374	5.967
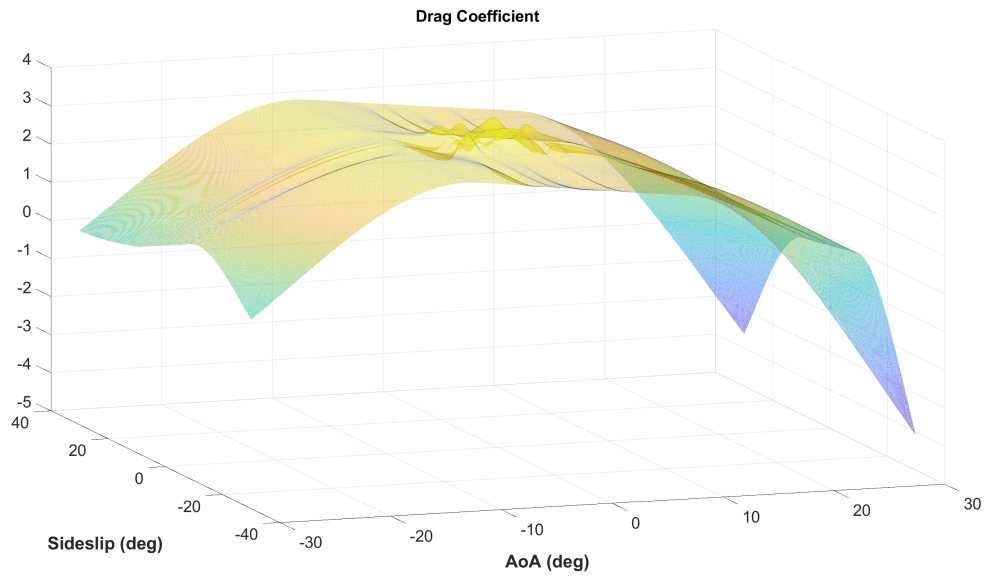
Figure C-1. Drag Coefficient Without Rudder
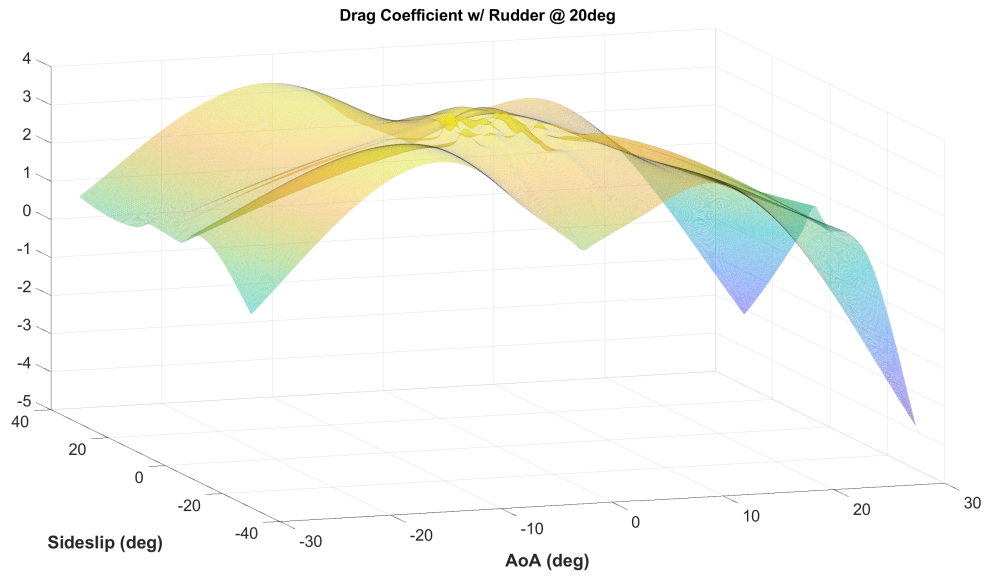
Figure C-2. Drag Coefficient With Rudder At 20°
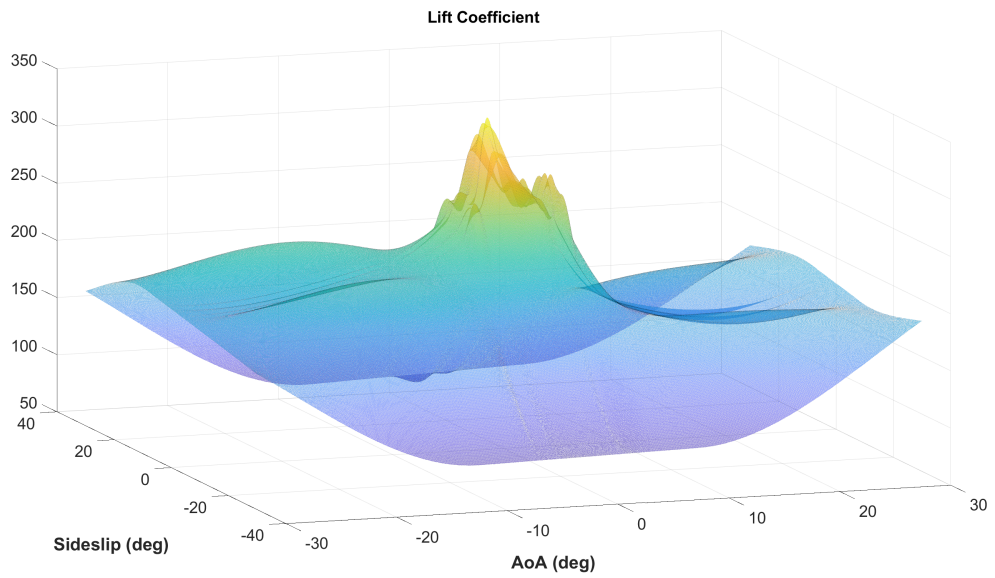
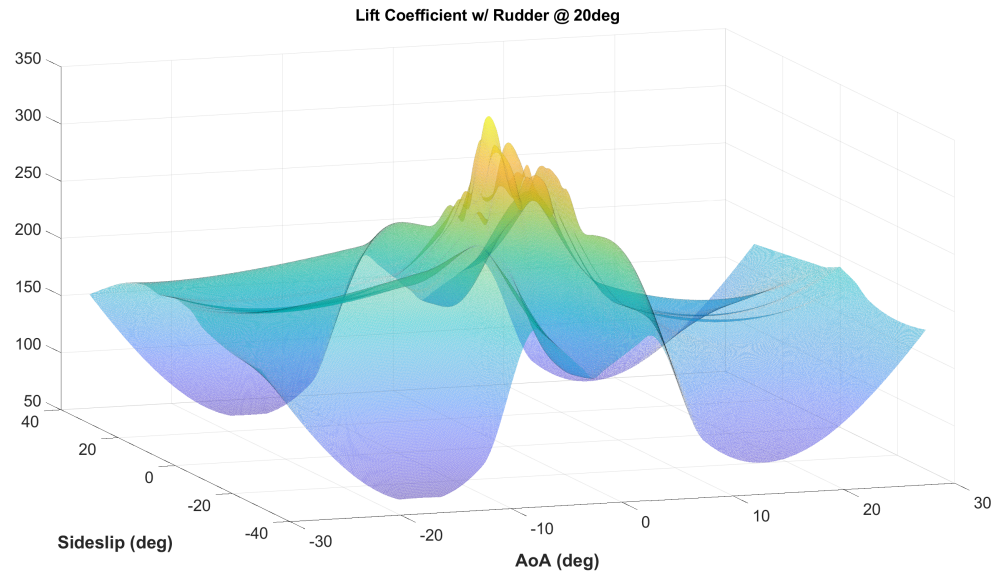**Figure C-3.** Lift Coefficient Without Rudder
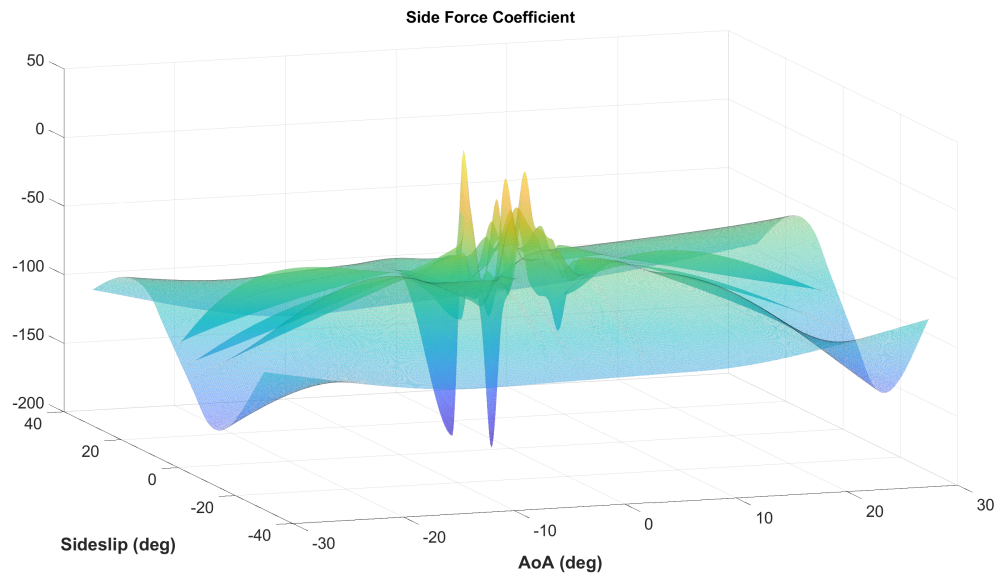
Figure C-4. Lift Coefficient With Rudder At 20°

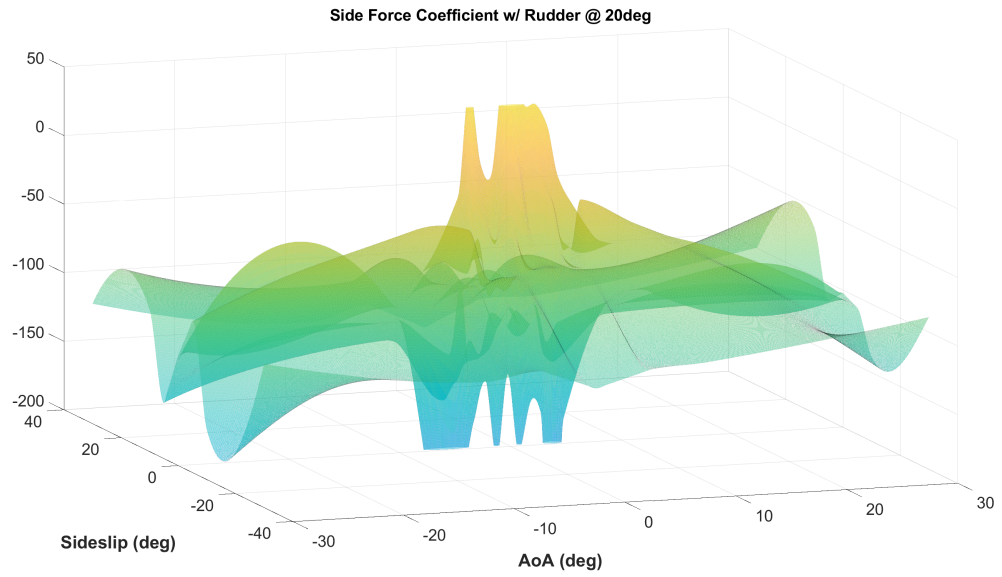**Figure C-5.** Side Force Coefficient Without Rudder

101

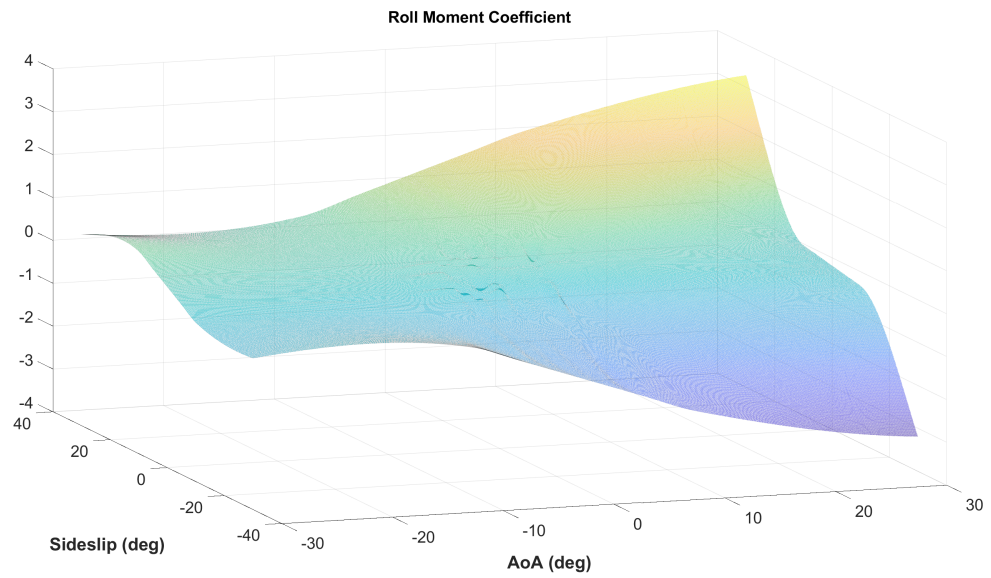**Figure C-6.** Side Force Coefficient With Rudder At 20°

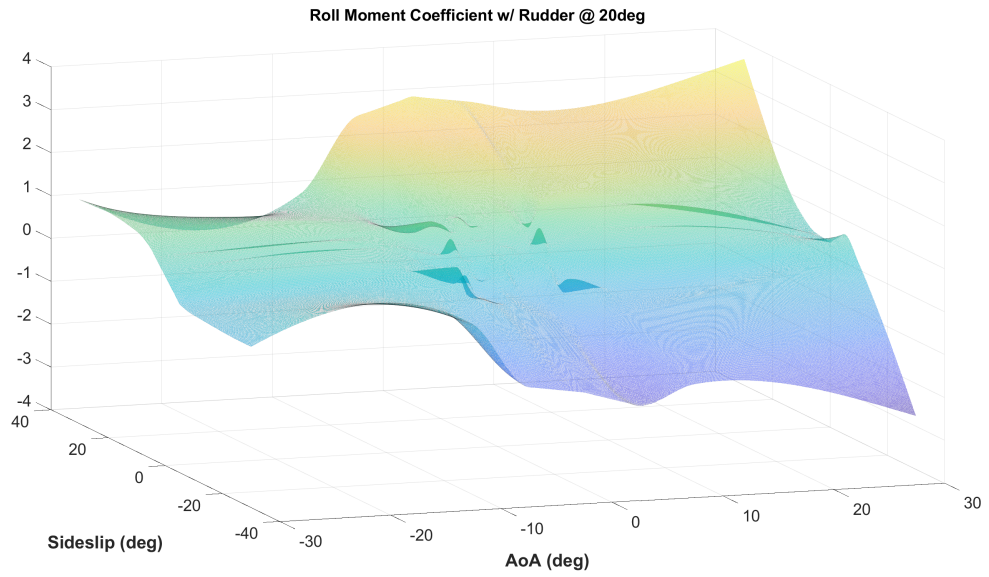**Figure C-7.** Roll Moment Coefficient Without Rudder

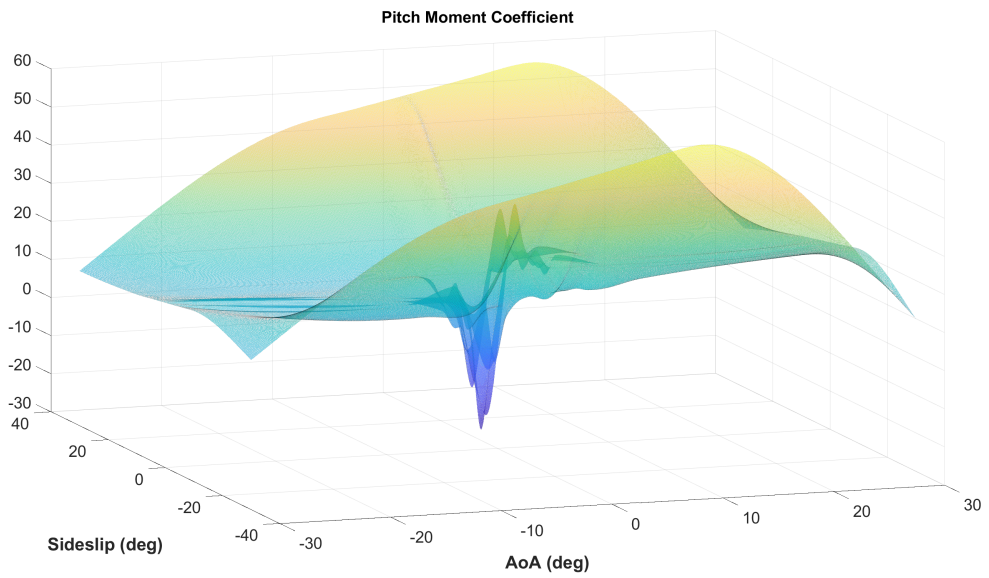**Figure C-8.** Roll Moment Coefficient With Rudder At 20°
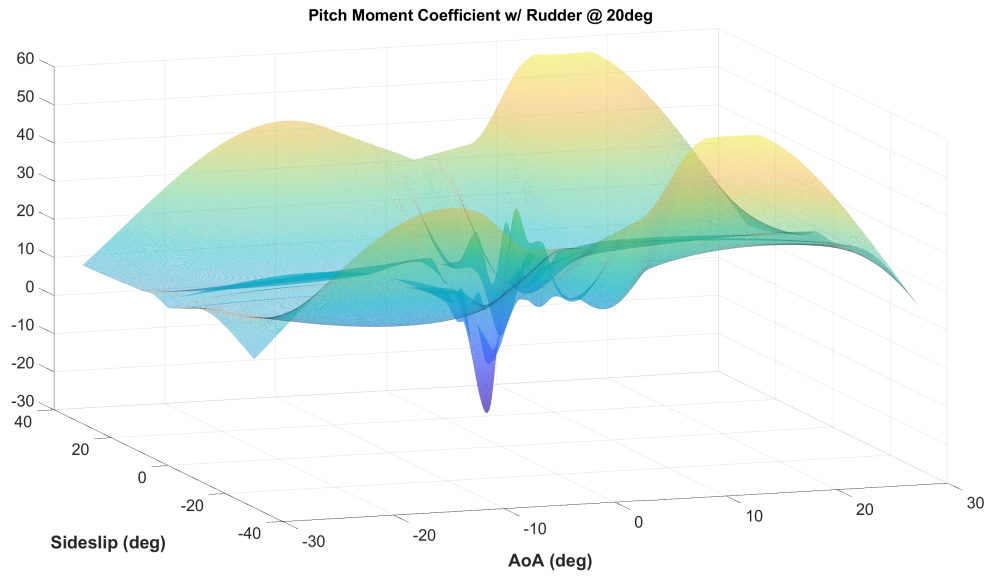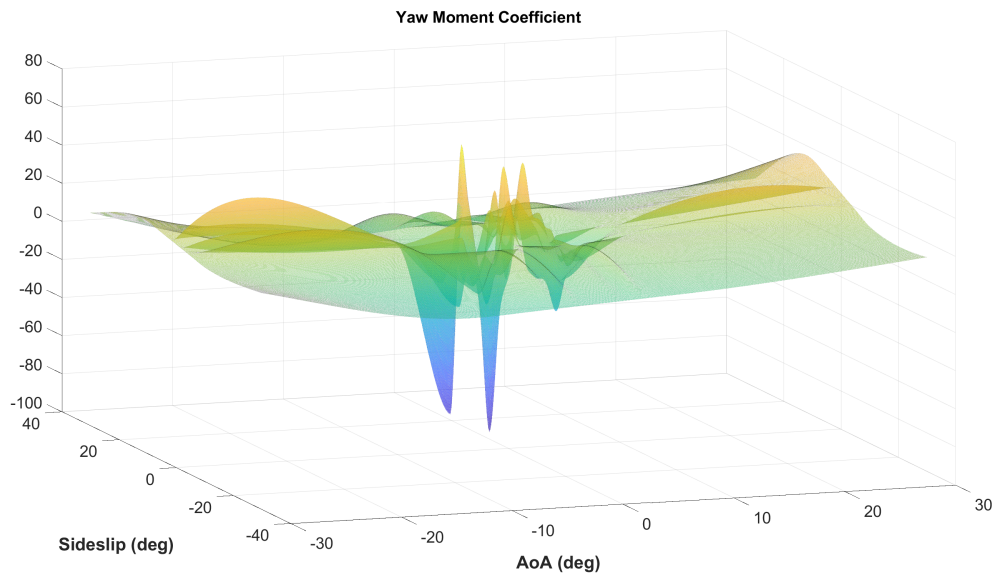

Figure C-9. Pitch Moment Coefficient Without Rudder

Figure C-10. Pitch Moment Coefficient With Rudder At 20°

Figure C-11. Yaw Moment Coefficient Without Rudder
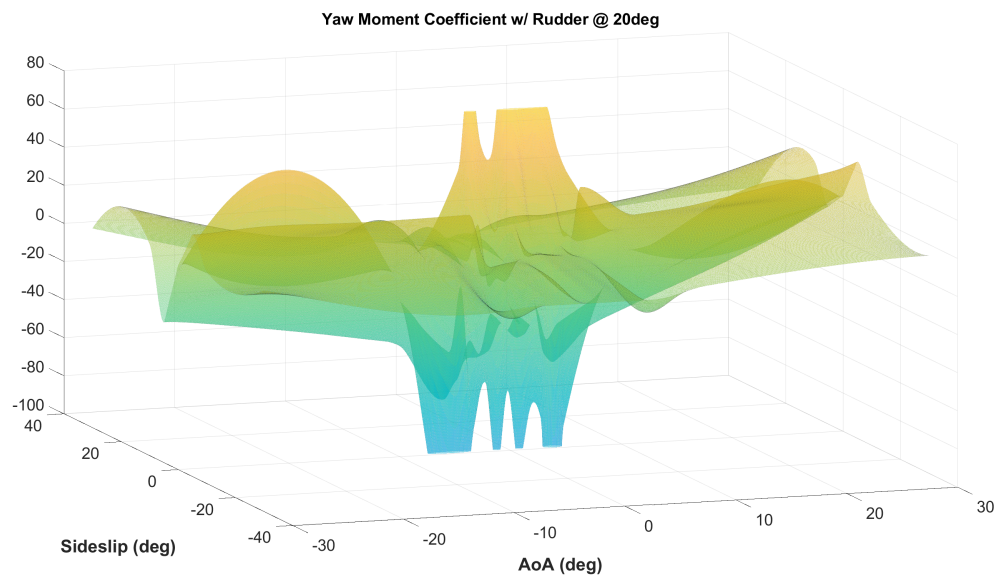
Figure C-12. Yaw Moment Coefficient With Rudder At 20°

Appendix D

Controller Gain Curves
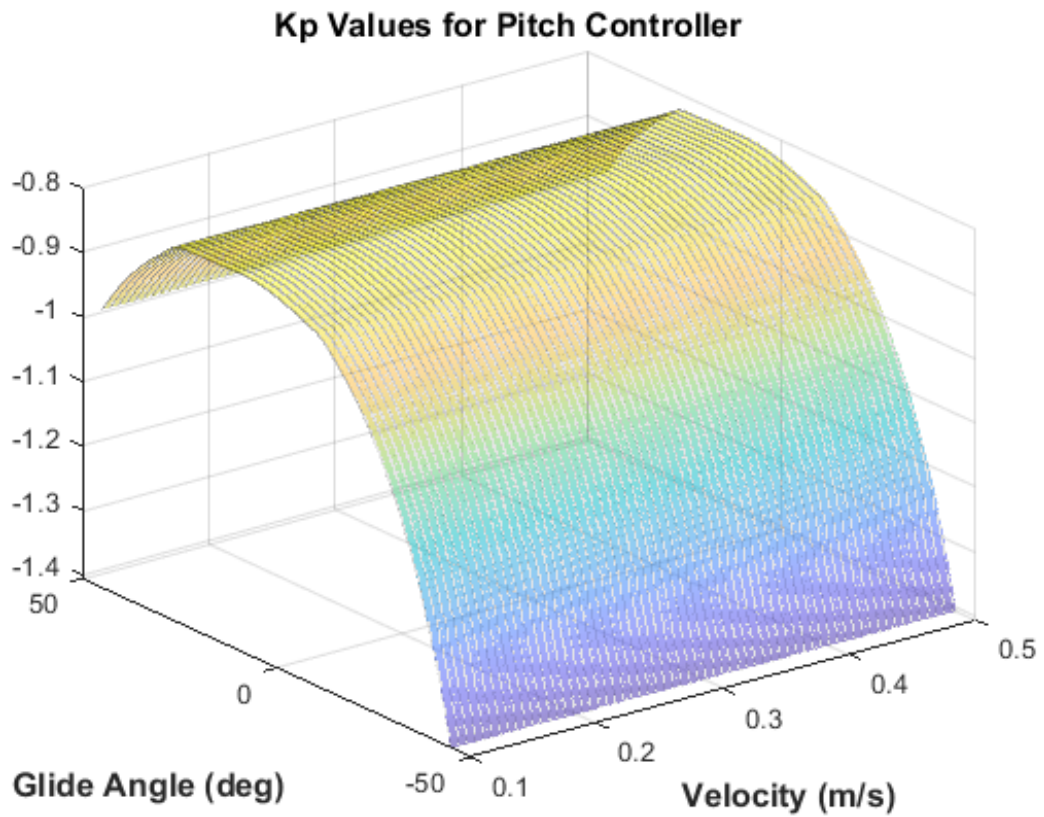
Figure D-1. K_p Gain Curve for Pitch Controller
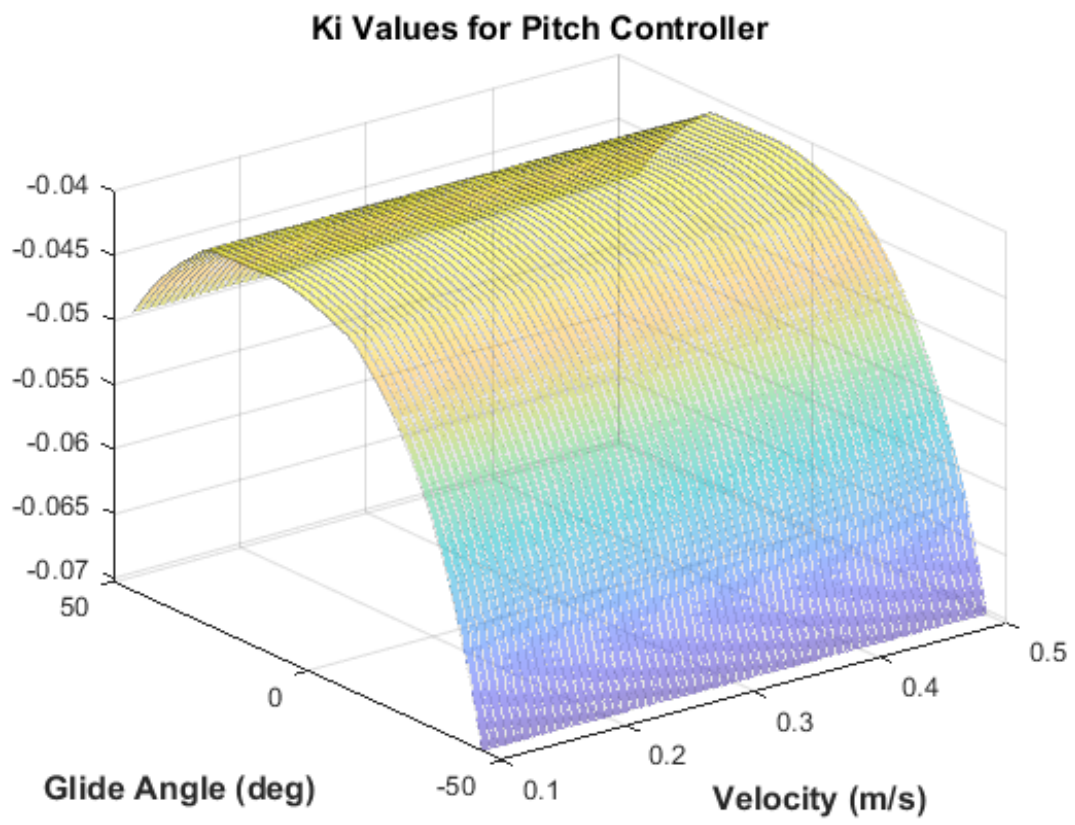
Figure D-2. K_i Gain Curve for Pitch Controller
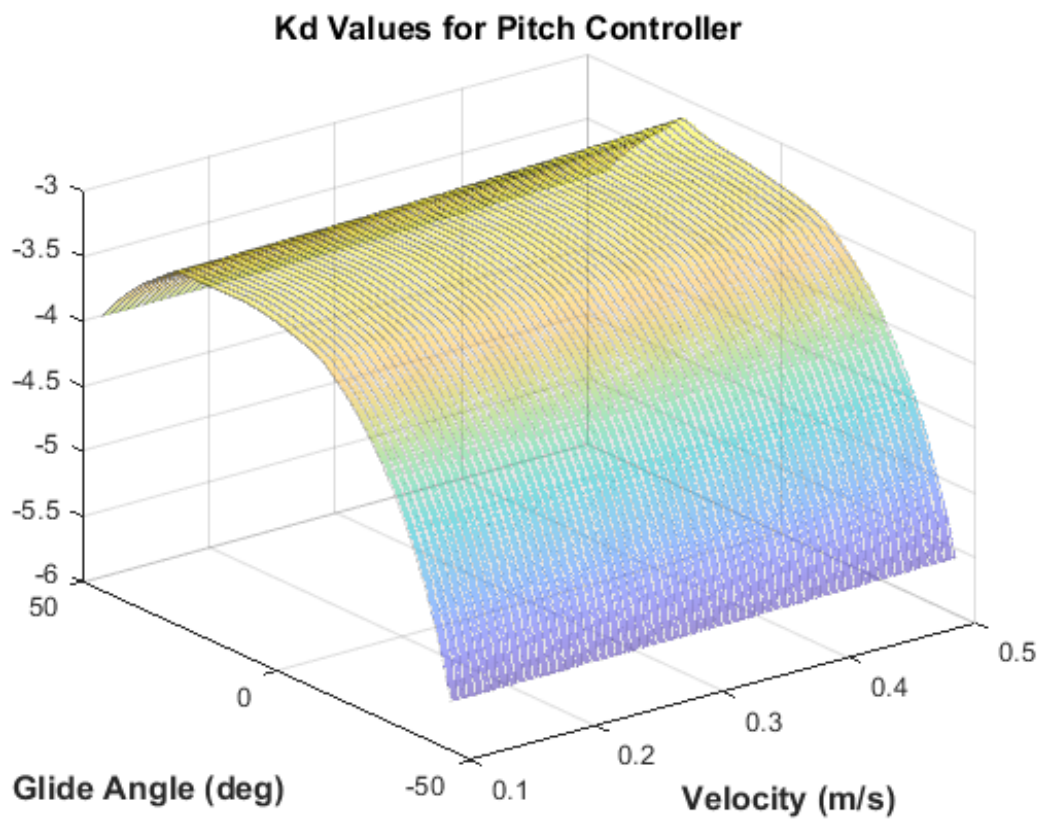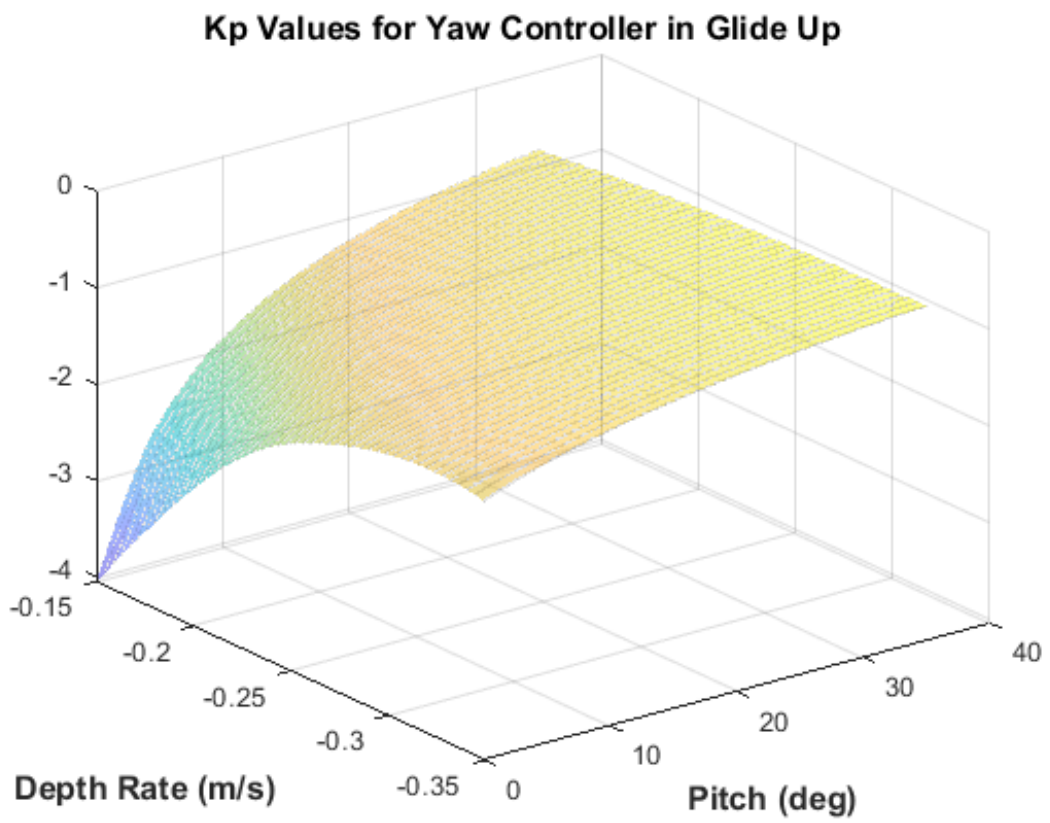
Figure D-3. K_d Gain Curve for Pitch Controller

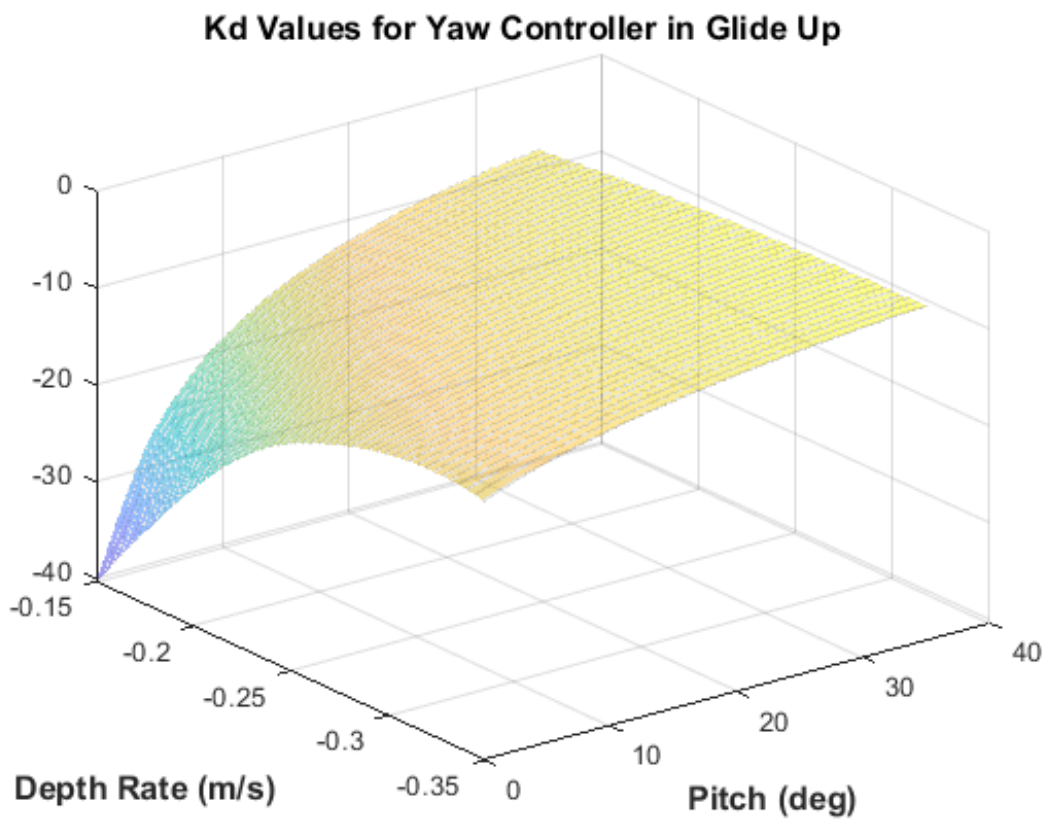**Figure D-4.** K_p Gain Curve for Heading Controller During Glide Up

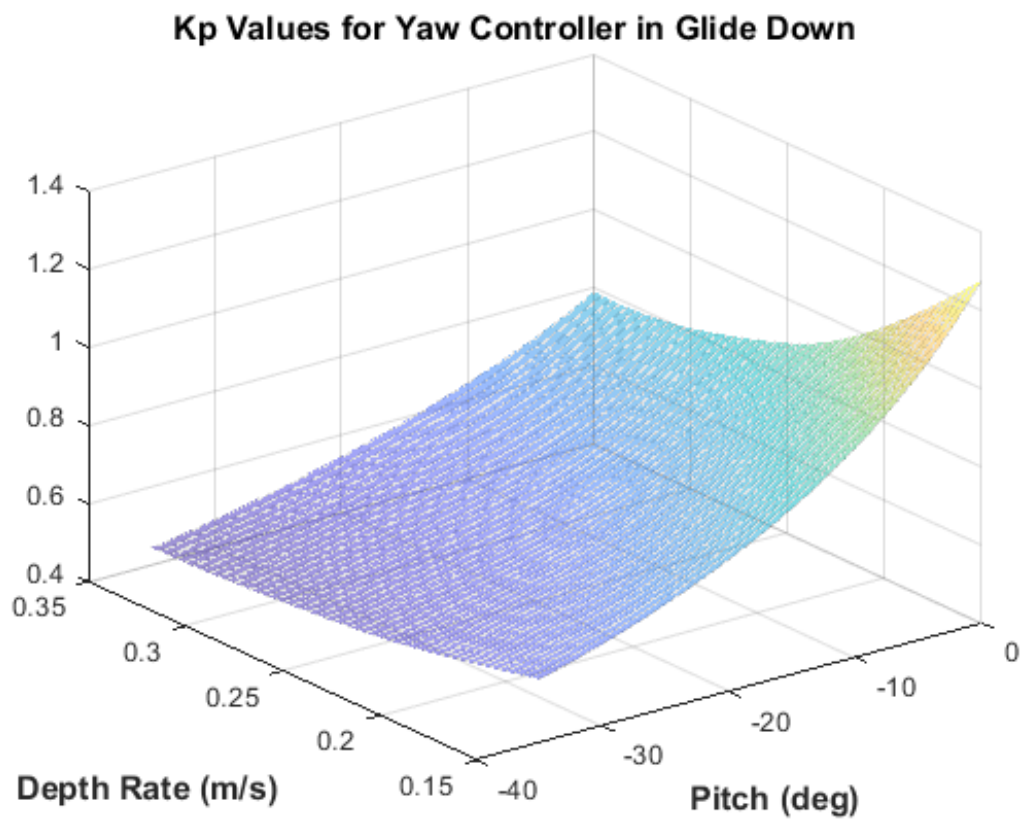**Figure D-5.** K_d Gain Curve for Heading Controller During Glide Up

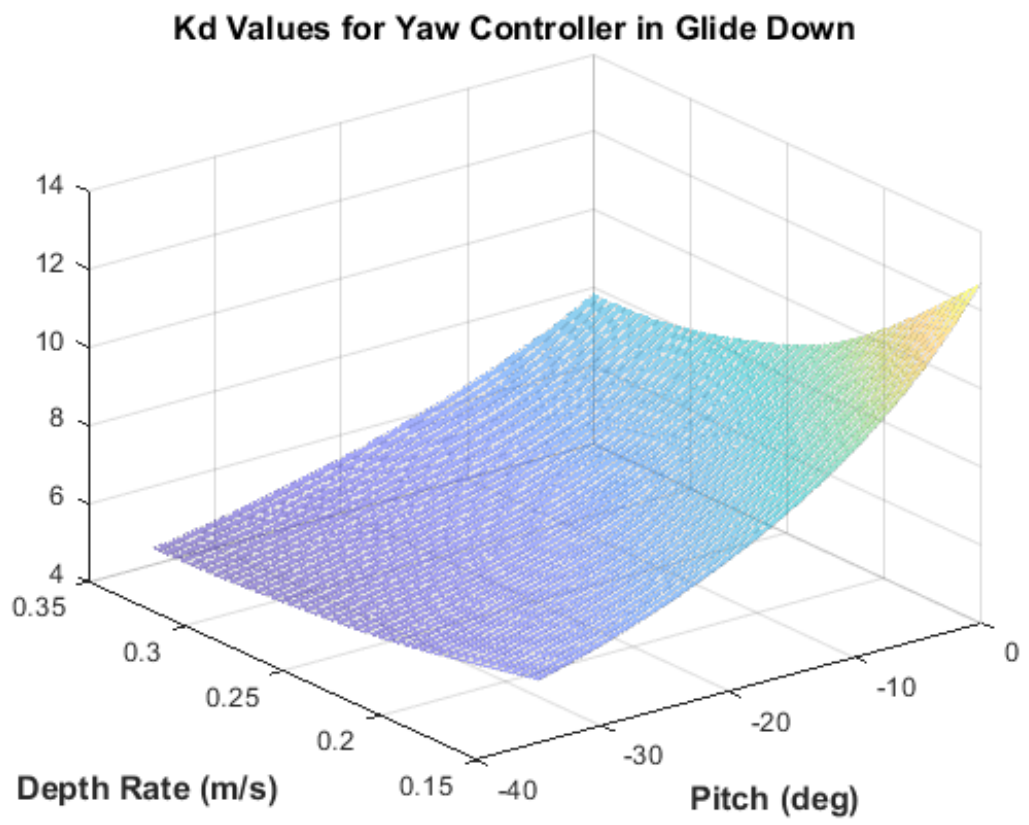**Figure D-6.** K_p Gain Curve for Heading Controller During Glide Down

Figure D-7. K_d Gain Curve for Heading Controller During Glide Down

Bibliography

[1] Hiroshi Akima. A new method of interpolation and smooth curve fitting based on local procedures. *Journal of the ACM*, 1970.

[2] Pradeep Bhatta. *Nonlinear stability and control of gliding vehicles*. PhD thesis, Princeton University, 2006.

[3] D Cowling. Full range autopilot design for an unmanned underwater vehicle. *IFAS Proceedings Volumes*, 1996.

[4] Alberto Alvarez Diaz. *Hydrodynamics of Underwater Gliders and the Impact on the Functionality of CTD Sensors*. PhD thesis, Technical University of Madrid, 2015.

[5] Duguid and Camilli. Improving resource management for unattended observation of the marginal ice zone using autonomous underwater gliders. *Frontiers in Robotics and AI*, 2021.

[6] Ali Hussain et al. Underwater glider modelling and analysis for net buoyancy, depth and pitch angle control. *Ocean Engineering*, 2011.

[7] C.C. Hang et al. Refinements of the ziegler-nichols tuning formula. *IEEE Proceedings-D, Vol. 138, No. 2*, 1991.

[8] Cotroneo et al. Glider and satellite high resolution monitoring of amesoscale eddy in the algerian basin: Effects on the mixed layer depth and biochemistry. *Journal of Marine Systems*, 2015.

[9] D. Mercado et al. Aerial-underwater systems, a new paradigm in unmanned vehicles. *Journal of Intelligent and Robotic Systems*, 2017.

[10] Darshana Makavita et al. Fuzzy gain scheduling based optimally tuned pid controllers for an unmanned underwater vehicle. *International Journal of Conceptions on Electronics and Communication Engineering*, 2014.

[11] Eriksen et al. Seaglider: A long-range autonomous underwater vehicle for oceanographic research. *IEEE Journal of Oceanic Engineering*, 2001.

[12] Isa et al. A hybrid-driven underwater glider model, hydrodynamics estimation, and an analysis of the motion control. *Ocean Engineering*, 2014.

[13] Joshua Graver et al. Underwater glider model parameter identification. *Symposium on Unmanned Untethered Submersible Technology*, 2003.

[14] Li et al. Vertical motion control of an underwater glider with a command filtered adaptive algorithm. *Journal of Marine Science and Engineering*, 2022.

[15] Liu et al. Using petrel ii glider to analyze underwater noise spectrogram in the south china sea. *Acoustics Australia*, 2018.

[16] Mahmoudian et al. Dynamics and control of underwater gliders ii: Motion planning and control. Technical report, Virginia Center for Autonomous Systems, 2010.

[17] Noh et al. Depth and pitch control of usm underwater glider: performance comparison pid vs. lqr. *Indian Journal of Geo-Marine Sciences*, 2011.

[18] Peng et al. Anti-windup, bumpless, and conditioned transfer techniques for pid controllers. *IEEE Control Systems Magazine*, 1996.

[19] Peng et al. Surface warming-induced global acceleration of upper ocean currents. *Science Advances - Oceanography*, 2022.

[20] Sang et al. Heading tracking control with an adaptive hybrid control for under actuated underwater glider. *ISA Transactions*, 2018.

[21] Sherman et al. The autonomous underwater glider "spray". *IEEE Journal of Oceanic Engineering*, 2001.

[22] Tchilian et al. Optimal control of an underwater glider vehicle. *Dynamics and Vibroacoustics of Machines*, 2017.

[23] Wagawa et al. Observations of oceanic fronts and water-mass properties in the central japan sea: Repeated surveys from an underwater glider. *Journal of Marine Systems*, 2019.

[24] Wang et al. Dynamic modeling and motion simulation for a winged hybrid-driven underwater glider. *China Ocean Engineering*, 2011.

[25] Wang et al. A backseat control architecture for a slocum glider. *Journal of Marine Science and Engineering*, 2021.

[26] Wang et al. Vertical profile diving and floating motion control of the underwater glider based on fuzzy adaptive ladrc algorithm. *Journal of Marine Science and Engineering*, 2021.

[27] Webb et al. Slocum: An underwater glider propelled by environmental energy. *IEEE Journal of Oceanic Engineering*, 2001.

[28] You Liu et al. Steering control for underwater gliders. *Frontiers of Information Technology and Electronic Engineering*, 2017.

[29] Yu et al. Development and experiments of the sea-wing underwater glider. *China Ocean Engineering*, 2011.

[30] Ziaeefard et al. Effective turning motion control of internally actuated autonomous underwater vehicles. *Journal of Intelligent and Robotic Systems*, 2017.

[31] Fossen and Ross. Nonlinear modeling, identification and control of uuvs. *Guidance and Control of Unmanned Marine Vehicles*, 2006.

[32] Jesse Geisbert. Hydrodynamic modeling for autonomous underwater vehicles using computational and semi-empirical methods. Master's thesis, Virginia Polytechnic Institute, 2007.

[33] Gladkikh and Tenzer. A mathematical model of the global ocean saltwater density distribution. *Pure and Applied Geophysics*, 2011.

[34] Joshua Graver. *Underwater Gliders: Dynamics, Control and Design.* PhD thesis, Princeton University, 2005.

[35] Isa and Arshad. Buoyancy-driven underwater glider modelling and analysis of motion control. *Indian Journal of Marine Sciences*, 2012.

[36] Isa and Arshad. Neural networks control of hybrid-driven underwater glider. *Oceans – Yeosu*, 2012.

[37] Isa and Arshad. An analysis of homeostatic motion control system for a hybrid-driven underwater glider. *International Conference on Advanced Intelligent Mechatronics*, 2013.

[38] Isa and Arshad. Modeling and motion control of a hybrid-driven underwater glider. *Indian Journal of Geo-Marine Sciences*, 2013.

[39] Isa and Arshad. Development of a hybrid-driven autonomous underwater glider with a biologically inspired motion control system. *Asian Control Conference*, 2015.

[40] Jenkins and D'Spain. Autonomous underwater gliders. In *Springer Handbook of Ocean Engineering*, pages 301 – 321. Springer, New York, NY, 2016.

[41] Leonard and Graver. Model-based feedback control of autonomous underwater gliders. *IEEE Journal of Oceanic Engineering*, 2001.

[42] Nina Mahmoudian and Craig Woolsey. Underwater glider motion control. *IEEE Conference on Decision and Control*, 2008.

[43] Nomoto. On the steering qualities of ships. *International Shipbuilding Progress*, 1957.

[44] Fletcher Paddison. The talos control system. *Johns Hopkins APL Technical Digest*, 1982.

[45] Jan Petrich and Daniel Stilwell. Robust control for an autonomous underwater vehicle that suppresses pitch and yaw coupling. *Ocean Engineering*, 2010.

[46] Teledyne Webb Research. *Slocum G2 Operators Manual*, 2012.

[47] Daniel Rudnick. Ocean research enabled by underwater gliders. *Annual Review of Marine Science*, 2016.

[48] Rugh and Shamma. Research on gain scheduling. *Automatica*, 1999.

[49] De Souza and Maruyama. Intelligent uuvs: Some issues on rov dynamic positioning. *IEEE Transactions on Aerospace and Electronic Systems*, 2007.

[50] Gregory Stewart. A pragmatic approach to robust gain scheduling. *IFAC Symposium on Robust Control Design*, 2012.

[51] Henry Stommel. The slocum mission. *Oceanography*, 1989.

[52] Yang and Ma. Sliding mode tracking control of an autonomous underwater glider. *International Conference on Computer Application and System Modeling*, 2010.

[53] Feitian Zhange and Xiaobo Tan. Passivity-based stabilization of underwater gliders with a control surface. *Journal of Dynamics Systems, Measurement, and Control*, 2015.

[54] Mingxi Zhou. The approach of improving the roll control of a slocum autonomous underwater glider. Master's thesis, Memorial University of Newfoundland, 2012.